



Università degli Studi di Napoli *Federico II*

DOTTORATO DI RICERCA IN
FISICA

Ciclo XXXIII

Coordinatore: prof. Salvatore Capozziello

**Event reconstruction and data analysis techniques
for the SHiP experiment**

Settore Scientifico Disciplinare FIS/01

Dottorando
Antonio Iuliano

Tutori
Prof. Giovanni De Lellis
Dott.ssa Antonia Di Crescenzo

Anni 2018/2021

Index

Introduction	5
1 The Physics Beyond Colliders landscape	7
1.1 Introduction	7
1.2 Portals to the Hidden Sector	9
1.2.1 Introduction to the portal framework	9
1.2.2 Vector portal	10
1.2.3 Scalar portal	11
1.2.4 Neutrino Portal	12
1.2.5 Axion Portal	13
1.3 Implications for experimental searches	14
1.3.1 Proposals from the Physics Beyond Colliders at CERN	15
1.4 High-energy neutrino physics at CERN	19
1.4.1 Introduction	19
1.4.2 High energy neutrino searches	20
1.4.3 Tau neutrino cross section	21
1.4.4 Neutrino magnetic moment	25
1.4.5 Neutrino induced charm production	26
2 Design of the SHiP experiment	28
2.1 The Beam Dump Facility	29
2.1.1 Location and beam delivery	29
2.1.2 The target	31
2.1.3 Hadron absorber and active muon shield	32
2.2 Scattering Neutrino Detector	35
2.2.1 Emulsion Target	35
2.2.2 Target Magnetization	40
2.2.3 Muon Tracker	41
2.3 Hidden Sector detector	42

2.3.1	The decay vessel	43
2.3.2	Hidden Sector Spectrometer	44
2.3.3	Calorimeters and Particle Identification	45
2.4	SHiP sensitivity to new physics	47
2.4.1	Sensitivity to Light Dark Matter	47
2.4.2	Hidden Sector performances	48
2.4.3	Sensitivity to Heavy Neutral Leptons	49
3	Neutrino interactions in the Scattering Neutrino Detector	51
3.1	Tau neutrino production at SHiP	52
3.1.1	Heavy flavour cascade production	52
3.1.2	Expected neutrino yields	53
3.2	Neutrino detection in the SND	57
3.2.1	SND layout	58
3.2.2	Lepton identification	59
3.2.3	Tau neutrino interaction within the ECC target	61
3.2.4	Momentum and charge measurement of tau daughters	64
3.2.5	Tau lepton decay channels	65
3.3	Background from neutrino-induced charm events	66
3.4	Current status of SND design	69
4	Electromagnetic shower reconstruction	71
4.1	Energy loss and shower development	72
4.2	Electron beam exposure at DESY	74
4.2.1	Motivation	74
4.2.2	Experimental apparatus	75
4.2.3	Emulsion data reconstruction	78
4.3	Shower reconstruction algorithms	80
4.3.1	Introduction	80
4.3.2	Background	82
4.3.3	Standard reconstruction procedure	82
4.3.4	Machine Learning classification	86
4.3.5	Energy resolution	92
4.4	Conclusions and next steps	94
5	SHiP-charm experiment	95
5.1	Introduction	95
5.2	Physical background	95

5.2.1	Observation of the first charm pair production event	95
5.2.2	Current knowledge of charm hadroproduction	98
5.3	Optimization run of the SHiP-charm experiment	100
5.3.1	Experimental layout	100
5.3.2	Summary of the data taking	106
5.4	Event simulation	109
5.4.1	Acceptance of the magnetic spectrometer	109
5.4.2	Event simulation in the emulsion target	111
6	Analysis of the SHiP-charm emulsion data	113
6.1	Reconstruction of emulsion data	113
6.1.1	Track reconstruction	114
6.1.2	Vertex reconstruction	115
6.2	Reconstruction of proton interactions	116
6.2.1	Boosted Decision Tree classification	117
6.2.2	Results and interaction length fit	118
6.2.3	Matching with pixel telescope	120
6.3	Search for associated charm production	122
6.3.1	Event topology	122
6.3.2	Decay search procedure	125
6.3.3	Momentum measurement through Multiple Coulomb Scattering	128
6.4	Conclusions	129
	Conclusions	132
A	List of ECC configurations for SHiP-charm optimization run	134
A.1	CHARM1 configuration	134
A.2	CHARM2 configuration	135
A.3	CHARM3 configuration	135
A.4	CHARM4 configuration	136
A.5	CHARM5 configuration	136
A.6	CHARM6 configuration	136
	Bibliography	144

Introduction

The preparation of new experiments in Particle Physics requires a large effort in the development of dedicated reconstruction and data analysis techniques. This requirement is even stronger in high intensity environments, where detectors have to cope with large particle rates avoiding any significant loss on performance.

In this regard, a challenging environment is presented by the SHiP (Search for Hidden Particles) experiment, a proposal for a new high intensity beam dump facility at the CERN SPS, with promising studies both on the search for new particles and on neutrino physics. A main component of this project is the Scattering and Neutrino Detector (SND), designed to detect high statistics of neutrino interactions and to search for light dark matter scattering. It is composed of a magnetic spectrometer followed by a muon filter. The spectrometer employs nuclear emulsion films and SciFi trackers, designed to locate the event and to measure particle charge and momentum.

The nuclear emulsion detector is designed according to the Emulsion Cloud Chamber (ECC) technique: the target unit is a brick of passive plates, interleaved with emulsion films acting as submicrometric resolution trackers. The main tasks of the emulsion detectors are to identify the particle interaction vertices and the decay vertices from short-lived particles. Particle energy can be estimated by the multiple coulomb scattering in the passive material between emulsion films. ECC bricks can be also employed as sampling calorimeters to identify electromagnetic showers. The emulsions have been successfully employed in large experiments, but SHiP will provide higher intensity. Therefore, all the algorithms and analysis techniques need to be adapted to this challenging environment and to be tested.

My Ph.D. activity has been directed towards the development of new reconstruction tools and the study of the ECC detector performances for the SHiP experiment. My research has been within the Naples emulsion

laboratory, involving both simulation of neutrino interactions in SHiP and data collected by two different experiments, performed in these years. Both experiments have in common the employment of ECCs as their main target, providing an optimal environment to study the response of the detector.

This thesis is structured in six chapters:

- **Chapter 1** reviews the landscape of Physics Beyond Colliders, an exploratory study which aims at scoping the possibilities of new projects and experiments at CERN, other than higher energy colliders. The current open questions and topics of interest in particle physics are discussed.
- **Chapter 2** describes the experimental apparatus of the SHiP experiment. Even if all its components are mentioned, deeper focus is directed towards the Scattering and Neutrino Detector, which is the subject of my studies.
- **Chapter 3** is dedicated to detection of tau neutrino interactions in the SND detector at SHiP. After the discussion of the selection procedure, signal efficiency and background rejection are estimated with a full simulation;
- **Chapter 4** is focused on the task of electromagnetic shower reconstruction, which plays a key role in detection of both neutrino interactions and light dark matter scatterings. From a test beam performed at DESY in 2019, the standard reconstruction is compared with a new machine learning algorithm;
- **Chapter 5** introduces the SHiP-charm experiment, started in 2018 at CERN SPS, to measure charm associated production. The apparatus and general Monte Carlo simulation are described;
- Finally, **Chapter 6** is dedicated to the analysis of emulsion data from the 2018 exposure. Topics of study are inelastic proton interactions and charm decays. After describing track and vertex reconstructions, results are presented and discussed.

Chapter 1

The Physics Beyond Colliders landscape

1.1 Introduction

Enormous progress has been achieved by particle physicists in the last years: with the discovery of the Higgs boson in 2012 [1, 2], the Standard Model (SM) has been completed, and its predictions are continuously confirmed by precise measurements. However, many questions remain open:

- **Dark Matter.** The current cosmological model associates only 5% of the Universe to ordinary matter, the remaining part being divided between dark energy (68%) and dark matter (27%). Dark matter exhibits all expected features of known neutral massive weakly-interacting particles, but its nature is still unaccounted for. On the other side, the properties of dark energy are mostly unknown;
- **Baryon Asymmetry.** The origin of ordinary matter itself is not known: the current dominance of matter over antimatter means that, when the Universe started cooling, the amount of matter should have been larger than antimatter, otherwise both would have been totally annihilated. However, the CP violation present in the Standard Model is too small to explain the asymmetry ($\frac{n_B}{n_\gamma} = 10^{-10}$, where n_B is the baryon density and n_γ is the photon density);
- **Neutrino masses.** Neutrinos are the only neutral fermions in the Standard Model. The discovery of oscillations has provided experimental evidence of a nonzero neutrino mass, but the mass origin can-

not be explained by the Standard Model, which does not foresee the existence of a new, right-handed, neutrino. Most of the new physics models give neutrinos their masses through the introduction of new particles, such as sterile neutrinos. Until now, none of these particles have been discovered.

To address these issues, a rich environment of theories and models has been proposed, describing what we usually call Beyond the Standard Model (BSM) physics. Unfortunately, even after years of intense search, no significant (i.e. $> 5\sigma$) and convincing (i.e. demonstrably unaffected by possible systematics) deviation from the Standard Model has been found in experiments [3]. The natural question which arises is why new particles have not been observed: a possible reason is that these particles are heavier than the current TeV energy scale explored by LHC. In this case, it is required to push forward the energy frontier, through the introduction of new colliders such as the currently proposed FCC [4].

Meanwhile, over the past 10 years another option has received increasing attention. It could be that new physics is confined into a “hidden” sector (or “dark” sector) connected to the Standard Model only via the interaction of still unknown particles. This situation can be described theoretically by introducing new fields, which are uncharged under the SM gauge groups, therefore they can interact only via a relatively small set of “portals” to SM particles. In this case, new particles can be lighter, and the reason they phenomenologically escape detection is their weak coupling to the SM fields. It is then necessary to maximize the number of interactions, by creating an high intensity environment where these particles can be searched for. This approach is referred to as investigating the intensity frontier.

Figure 1.1 depicts an artistic representation of the current landscape in the search for new physics. The currently known particles are shown, together with the research paths in the energy frontier and in the intensity frontier.

The two frontiers are not completely unrelated: very weak interactions often arise by integrating out heavier particles and the weakness of interactions is related to the underlying very large energy scale. For example, a coupling constant can be related to a power of an inverse mass scale $1/M^k$, representing the mass scale of new physics: this coupling constant becomes then the fundamental parameter in the search for new particles. Therefore,

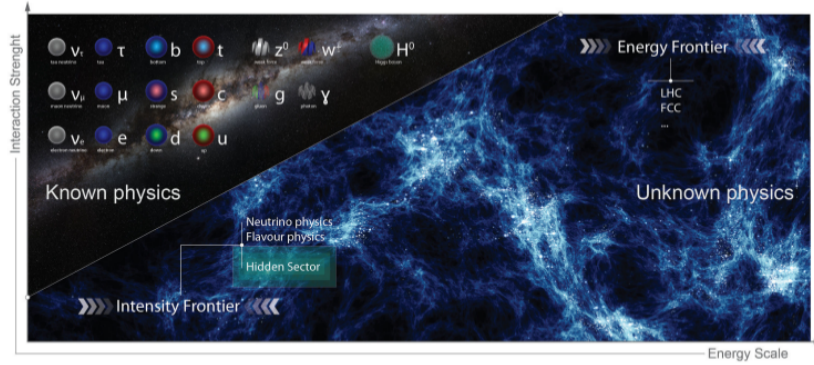


Figure 1.1: Current frontiers of new physics: the energy frontier, looking for particles with heavy masses and the intensity frontier, looking for weak couplings.

only by acquiring data from both sections of the parameter space, a complete coverage can be reached, thus excluding or confirming most of the currently discussed models of new physics.

1.2 Portals to the Hidden Sector

1.2.1 Introduction to the portal framework

The main portal framework can be defined by the following generic setup. Let O_{SM} and O_{DS} be an operator composed from SM fields and a corresponding operator from the dark sector fields, respectively. Combining them, the following interaction Lagrangian can be obtained:

$$\mathcal{L} = \sum O_{SM} \times O_{DS}, \quad (1.1)$$

where the sum goes over a variety of possible operators, which have different composition and dimension. We will briefly introduce some of the portals in the SM with the lowest dimensions, usually classified in the following types:

- Dark Photon (Vector portal);
- Dark Higgs (Scalar portal);
- Axion;
- Sterile Neutrino.

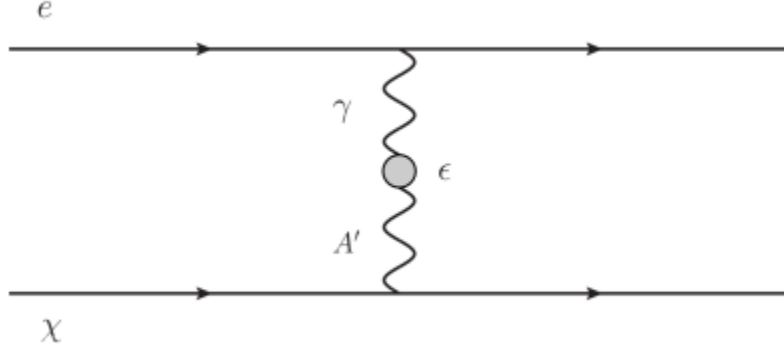


Figure 1.2: Scattering of a dark matter candidate χ with an SM electron, through the exchange of a mixed $\gamma - A'$ propagator.

1.2.2 Vector portal

The hypothesis of one or more new U(1) gauge groups, in addition to the $SU(3) \times SU(2) \times U(1)$ combination from the Standard Model, is proposed by many models of new physics.

In the portal framework, the corresponding new vector state can be a light particle, connecting SM fields and Dark Sector fields. Due to the close analogy to the QED, the resulting new state is called *dark photon*, usually denoted as A' . The resulting Lagrangian can be written as

$$\mathcal{L} = \mathcal{L}_{SM} + \frac{\epsilon}{2} F'_{\mu\nu} F^{\mu\nu} - \frac{1}{4} F'_{\mu\nu} F'^{\mu\nu} + \frac{m_{\gamma'}^2}{2} A'_\mu A'^\mu, \quad (1.2)$$

where $F'_{\mu\nu} = \partial_\mu A'_\nu - \partial_\nu A'_\mu$ is the new field strength tensor. The interaction between the Standard Model and the Dark Sector fields is expressed by the term $F'_{\mu\nu} F^{\mu\nu}$, multiplied by a factor ϵ .

Examples of dark photon production are meson decays (most important process being $\pi^0 \rightarrow \gamma A'$), proton bremsstrahlung ($pp \rightarrow pp A'$) and direct perturbative QCD production (processes like $q + \bar{q} \rightarrow A'$ and $q + g \rightarrow q + A'$.)

Depending on the theory, the Standard Model can be extended with only a single new state A' , or new χ particles may also be present. Thus, the dark photon may decay either visibly in a pair of SM particles or invisibly in a pair of new particles $\chi\chi$. In the latter case, a produced χ particle can then scatter off an electron, as shown in Figure 1.2, and the event can be

detected from the scattered electron. Since the new particle χ can be a dark matter candidate, the dark photon plays the role of a mediator, thus explaining the existence of dark matter.

1.2.3 Scalar portal

The discovery of the Higgs boson confirmed the existence of fundamental scalar bosons in nature. Many extensions of the Standard Model predict the existence of other new states of this kind. In the portal framework, they can be light and with highly suppressed couplings to the Standard Model.

The minimal scalar portal operates with one extra singlet field S and two types of couplings, μ and λ :

$$\mathcal{L}_{scalar} = \mathcal{L}_{SM} + \mathcal{L}_{DS} - (\mu S + \lambda S^2) H^\dagger H. \quad (1.3)$$

The μ factor leads to the mixing of the SM boson h state with a new S state. In the limit of small mixing, this can be written as

$$\theta = \frac{\mu v}{m_h^2 - m_s^2}. \quad (1.4)$$

If the other coupling factor λ is assumed to be zero, all production and decay processes of the dark scalars are controlled by the same parameter μ .

The resulting new state m_s can be light ($m_s \ll m_h$), with the same production mechanisms and decay modes of a SM higgs boson, having the same mass. However, the production cross sections and decay rates are suppressed by a factor θ^2 , and the lifetime is inversely proportional to the squared mixing angle.

Below the electron production threshold ($m_s < 2m_e$), the dark scalar can still decay to two photons. Above the electron threshold, but below the hadronic threshold ($2m_e < m_s < 2m_\pi$), the scalar can decay to electrons and/or muons, with a width given by

$$\Gamma(S \rightarrow l\bar{l}) = \frac{g_*^2 m_l^2 m_s}{8\pi v^2} \left(1 - 4\frac{m_l^2}{m_s^2}\right)^{3/2}. \quad (1.5)$$

For even heavier scalars, additional hadronic decay channels are possible, as shown in Figure 1.3. However, the appearance of hadronic resonances complicates the calculation of decay parameters for masses around

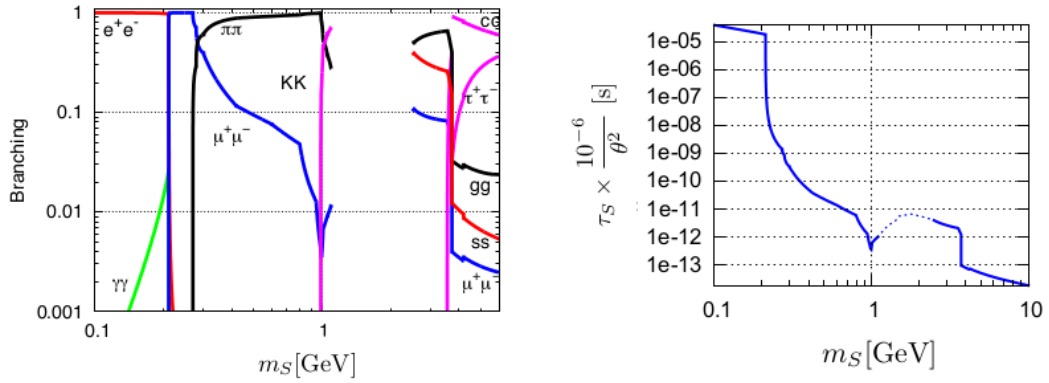


Figure 1.3: Decay properties of a dark scalar in function of its mass m_S . On the left: predicted decay branching ratios. On the right: scalar lifetime as a function of its mass m_S for constant mixing angle with the Higgs boson, $\theta^2 = 10^{-6}$. From the SHiP physics proposal [5], reproduced from [6].

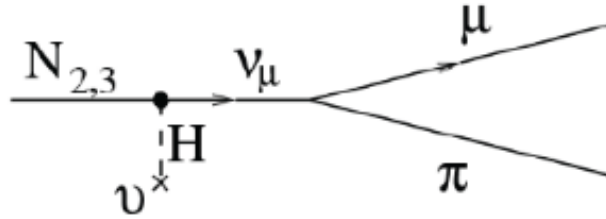


Figure 1.4: Decay diagram of a sterile neutrino $N_{2,3}$ into a muon and a pion.

2 GeV.

1.2.4 Neutrino Portal

The neutrino portal extensions of the Standard Model add one or several dark fermions N , which are also called heavy neutral leptons (HNLs).

For example, the Neutrino Minimal Standard Model (ν MSSM) solves all the SM puzzles by inserting three heavy right handed neutrinos, which couple to the left-handed SM neutrinos. Their introduction modifies the SM Lagrangian into

$$\mathcal{L} = \mathcal{L}_{SM} + \bar{N}_i i \not{\partial} N_i - U_{i\alpha} \Phi N_i L_\alpha - \frac{M_i}{2} \bar{N}_i^C N_i + h.c., \quad (1.6)$$

where

- N_i is the HNL field (N_i^C is a charge conjugate fermion);
- $U_{i\alpha}$ is the matrix of Yukawa couplings with $\alpha = e, \mu, \tau$;
- Φ is the Higgs field;
- L_α are the SM left-handed fields;
- M_i are the Majorana masses.

The introduction of these new right-handed states allows to explain the neutrino masses generation, through the I-type see-saw mechanism. Moreover, the lightest HNL, N_1 , has the mass of a few keV and it is a DM candidate, with a mean life larger than the lifetime of the Universe. On the other hand, N_2 and N_3 can explain the baryon asymmetry through a process of leptogenesis. They have masses in the MeV-GeV range and they are more unstable, decaying through mixing with active neutrinos in leptonic or semi-leptonic channels.

Experimentally, if HNLs exist, they would be produced in every process containing active neutrinos with a branching fraction proportional to the mixing parameters $|U_{e,\mu,\tau}|^2$. Then HNLs would decay via Charged Current (CC) and Neutral Current (NC) interactions into active neutrinos and other visible final states, as pions, muons and electrons. One of the main channels for experimental searches is $N_{2,3} \rightarrow \pi\mu$ (Figure 1.4): the signal is identified by the presence of two tracks coming from a single point, whose invariant mass is equal to the sterile neutrino's mass.

1.2.5 Axion Portal

QCD axions have been introduced to provide a natural solution to the strong CP problem, that is an apparent lack of CP violation in strong interactions. Even if current QCD axion models are restricted to sub-eV mass ranges, the existence of Axion-Like Particles (ALPs) can be assumed, having similar interactions of the axions, but larger masses.

An Axion-Like Particle is a pseudo-Nambu-Goldstone boson, coming from a new spontaneously broken symmetry. If this symmetry is not exact, the ALP is massive, but his mass is suppressed by the symmetry breaking scale: $m_A = \Lambda^2/f_A$. The resulting particle is connected to the SM via a

coupling to two gauge bosons or fermions. Depending on which coupling is assumed to be predominant, different phenomenologies (production and decay) are theoretically predicted.

To probe untested regions in the parameter space, both for ALPs coupled to a pair of bosons and a pair of fermions, the following production modes can be considered:

- directly from proton interactions

$$\begin{aligned} pp &\rightarrow A + X, \\ A &\rightarrow \gamma\gamma, \end{aligned} \tag{1.7}$$

- or via B-meson decay

$$\begin{aligned} pp &\rightarrow B + X \rightarrow A + K + X, \\ A &\rightarrow \mu^+\mu^-. \end{aligned} \tag{1.8}$$

1.3 Implications for experimental searches

All the portal models discussed so far share very weak couplings to the Standard Model. Therefore, a large amount of hidden particles needs to be provided, in order to allow the detection of a statistically significant amount of interactions.

In the case of dark matter candidates, a large cosmogenic amount of new particles can be found, thus motivating research in observatories and direct detection of dark matter experiments. However, an accurate knowledge of the source is needed, in order to minimize statistical and systematic uncertainties on the results.

Another possibility is the production of hidden particles in accelerators. Other than being a suitable alternative for dark matter search (Figure 1.5), this allows to look for new states which are not dark matter candidates.

Both scattering and decays into visible SM particles can be detected. However, different challenges arise between partially reconstructed final states, which include particles that cannot be detected (an example of such decay is $l^\pm l^\mp \nu_l$) and fully reconstructed final states, where all final particles are detectable (for example $l^\pm \pi^\mp$). To study partially reconstructed final states, kinematic cuts need to be looser, and particle identification becomes

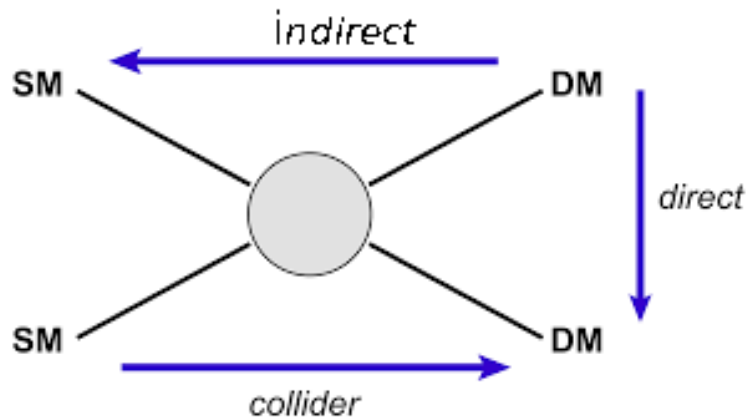


Figure 1.5: Complementary Dark Matter (DM) research procedures: direct searches, looking for nuclear recoil from scattering with SM particles; indirect research, looking for bumps in the SM particle spectrum in cosmic rays with ground based or space observatories; artificial production from interactions of known particles produced at colliders [7].

more important, since lepton number violation can be used to infer the presence of an undetected neutrino.

Finally, both for direct dark matter searches and production of hidden particles, a fundamental requirement is a zero-background environment, in order to not spoil the detected interactions with the Standard Model background.

1.3.1 Proposals from the Physics Beyond Colliders at CERN

The European Centre for Nuclear Research (in French *Conseil Européen pour la Recherche Nucléaire*, CERN) operates the most advanced machines in high energy physics. Its chain of accelerators, represented in Figure 1.6, gradually increases the energy of the protons, reaching 7 TeV at the latest stage, the Large Hadron Collider (LHC).

The LHC will remain the CERN flagship in the medium term. It is due to be enhanced in a High Luminosity LHC (HL-LHC) in 2026, aiming to deliver around 250 fb^{-1} per year, for ten years of operation.

At the same time, the whole CERN accelerator complex has a long history of evolution and adaption with each of the four operating synchrotrons, in order to serve a rich and diverse physics community. The CNGS neutrino beam program was successfully conducted until 2012, delivering a total of 1.8×10^{20} protons on target for the OPERA and ICARUS

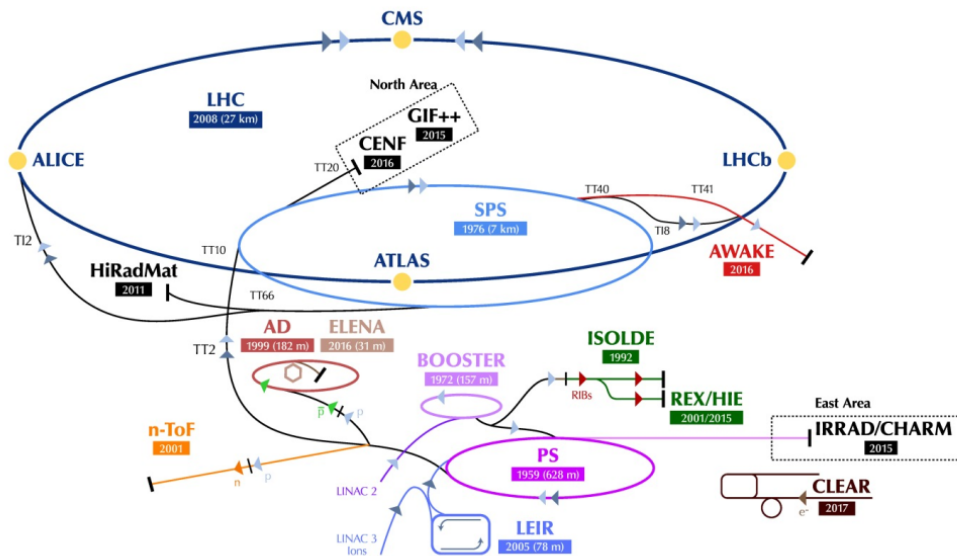


Figure 1.6: Overview of the CERN accelerator complex in 2018 [8].

detectors, located in the Gran Sasso underground laboratories. OPERA [9] established the oscillation of ν_μ to ν_τ with a significance higher than 6σ , and ICARUS [10] opened the way to large underground liquid argon TPCs.

Learning from this experience, the Physics Beyond Collider group was started, with the intent of studying the physics opportunities of research for new particles, with a complementary approach to the one currently followed in the four main experiments at the LHC line.

As shown in Figure 1.7, many proposals have been made, covering the wide physics landscape described by various BSM models. Since a complete list of all the projects would be out of the scope of this section, only a brief introduction of some proposals will be presented, focusing in the MeV - GeV mass range.

Experiments at the PS accelerator

REDTOP [11] is a fixed-target experiment, designed to search for new physics from the decay of η and η' mesons. These particles have almost all additive quantum numbers equal to zero (except their negative parity), similarly as the void and the Higgs boson. This leads to a suppression of SM decays and, conversely, a promising place to look for BSM effects, from the rare η and η' decays.

REDTOP experiment aims to collect a total of 10^{13} η and 10^{11} η' mesons,

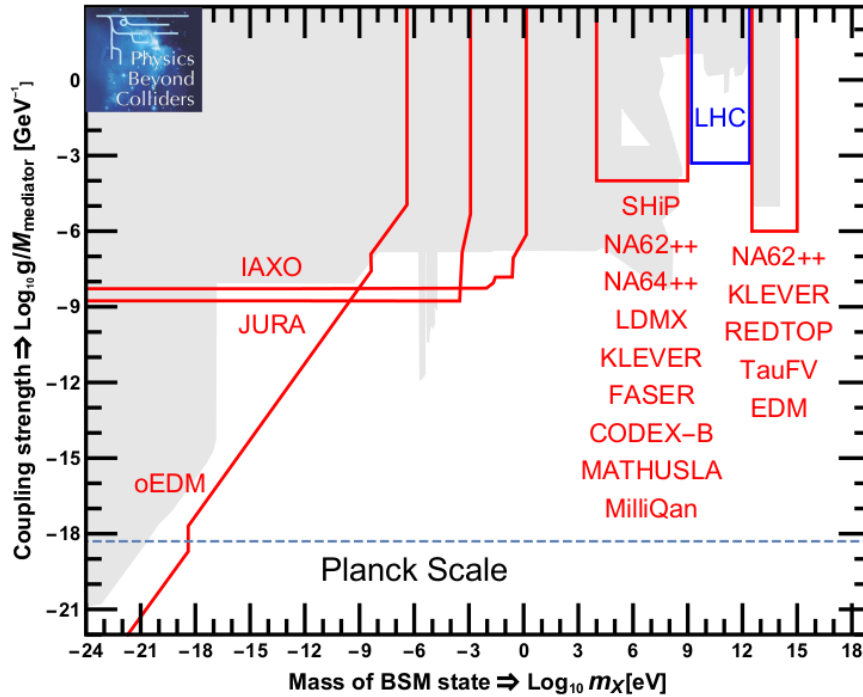


Figure 1.7: Schematic overview of the BSM landscape, based on a selection of specific models. The x-axis corresponds to the mass m_X of the lightest BSM state, and the y-axis to the scale of the effective new interaction where M_{mediator} is the mass of a heavy mediator and g its dimensionless coupling constant to the Standard Model. The gray shaded area outlines the currently excluded regions, the red areas are schematic outlines of the areas targeted by the experiments considered in the PBC sensitivity studies. The true sensitivities of individual experiments can vary significantly as function of the model [3].

produced from the interaction of 10^{17} protons with energy in the range of 1.7 – 1.9 GeV for η production and about the same number of protons with energy about 3.5 GeV for η' production.

Experiments at the SPS accelerator

The SPS beam line provides a high intensity 400 GeV proton beam, which creates an ideal environment to look for new particles at the GeV range.

NA62 [12] is an on-going experiment, currently measuring the branching ratio of the ultra-rare decay $K^+ \rightarrow \pi^+ \bar{\nu} \nu$. Nevertheless, the performance and layout of its detector allow an operation in beam dump mode, which would allow to search for the decays of hidden particles. The NA62 collaboration proposes to integrate 10^{18} protons on target for this scope, for a few months during RUN3 (2021-2023), in parallel with its main aim of measuring the kaon ultra-rare decay.

The NA64⁺⁺ experiment [13] aims to search for dark sector particles in an active dump. It can use a high energy (100 GeV) beam to scatter off nuclei: for example, an electron beam can be used to produce a vector mediator, via the reaction $e^- Z \rightarrow e^- Z A'$. The signature of a possible new A' state would appear as a single isolated electromagnetic shower in the active dump with detectable energy, accompanied by missing energy in the rest of the detector. The advantage of this technique is that the sensitivity scales with ϵ^2 , instead of ϵ^4 , since the new state is required to be produced, but not detected in the far detector. A similar procedure can be applied to high-energy muon and hadron beams.

The AWAKE experiment, placed at the former site of the CNGS target complex, is currently investigating the possibility of accelerating electron beams to GeV energies in a 10-20 m plasma cell [14]. This would allow to produce Dark Photon particles from a beam of 5×10^9 electrons/bunch, impinging on a tungsten target. Then the detection of the new particles would be performed with a NA64-like experiment downstream.

Finally the SHiP experiment [15] aims to study a wide variety of models containing long-lived particles with masses below $O(10 \text{ GeV})$ with unprecedented sensitivity, thanks to the introduction of a new Beam Dump Facility (BDF). The facility will operate at high intensity in a very clean, zero-background environment. Since the work of this thesis has been performed within the SHiP Collaboration, the details of this project will be

reported in the following chapters.

Experiments at LHC interaction points

The Large Hadron Collider provides the highest energy particles in the CERN accelerator complex. Thus, in order to explore the highest mass range currently available, new experiments have been proposed to look for BSM particles produced there.

Codex-B [16] is a proposed new shielded subdetector for LHCb, to be placed in what currently is the LHCb data acquisition room. The purpose of this detector is to search for new Long Lived Particles (LLPs), focusing mostly on relatively light new particles ($m \leq 10 \text{ GeV}$), for which background in ATLAS and CMS are prohibitive. The detector would be installed very close to the Impact Point, allowing large sensitivity even with low acceptance and luminosity. Moreover, the detector would be directly interfaced with LHCb trigger and reconstruction streams.

On the other hand, the FASER experiment [17] aims to search for LLP particles at 480 m from the Impact Point of the ATLAS experiment, with the following reactions:

$$pp \rightarrow LLP + X, \tag{1.9}$$

$$LLP \rightarrow \text{charged tracks} + X(\text{or } \gamma\gamma + X).$$

The signal is identified as two opposite Standard Model particles, having very high energy (O(TeV)) and pointing to a common vertex within the detector.

Finally the MATHUSLA collaboration [18] proposes to install a large detector on the surface, to detect Long Lived Particles produced from LHC collisions, during the High Luminosity phase. The planned surface of $200 \times 200 \text{ m}^2$ makes it also suitable for cosmic ray detection, thus providing a secondary physics application.

1.4 High-energy neutrino physics at CERN

1.4.1 Introduction

The existence of neutrino particles has been proposed early in the history of particle physics, dating back to Pauli's letter in 1930 [19], aimed at preserv-

ing energy conservation in beta decays. However, neutrinos have always been difficult to detect, since they only interact with weak interactions. Moreover, the data collected in the last century have provided many surprises, leading often to more questions than answers.

First, neutrinos occur in three flavours, ν_e , ν_μ , ν_τ , associated with the corresponding charged leptons e^- , μ^- , τ^- . The state at production is not always the same at detection, since neutrinos have been observed to oscillate from one specie to another, a phenomenon which can only happen if neutrinos are not massless. However, the mass is very low, less than one millionth of the lightest charged particle, the electron. The reason for their lightness is still unknown, and various models of new physics have been proposed to provide it.

The discovery of neutrino oscillations has also proved that the mass eigenstates $m_{1,2,3}$ are different from the flavour eigenstates. Experiments using neutrino oscillations have been able to measure the squared differences between the mass eigenstates with high accuracy, however they cannot provide the absolute values of m_1 , m_2 and m_3 . Whether m_2 is heavier than m_3 remains unknown, in what is commonly referred to as the neutrino mass hierarchy problem. If m_2 is lighter than m_3 , the hierarchy is said to be “normal”, but if it is heavier the hierarchy is called “inverted”.

The discovery of neutrino mass raises the question whether each mass eigenstate ν_i is identical to its antiparticle $\bar{\nu}_i$ or is distinct from it. If $\nu_i = \bar{\nu}_i$, the neutrinos are called Majorana particles, while if the states are different they are called Dirac particles. Usually conserved charges distinguish a particle from an antiparticle, for example the electric charge allows to separate electrons and positrons. However, neutrinos carry no charge motivated by theory (the only assumed conserved charge, the lepton number, is not protected by any gauge symmetry). If such a conserved charge does not exist, then there is nothing to distinguish $\bar{\nu}_i$ and ν_i . The neutrino may very well be a Majorana particle.

1.4.2 High energy neutrino searches

The presence of so many questions shows the need for more neutrino data, covering a spectrum of energies and flavours as wide as possible. To provide these data, the scientific community has advanced many and different proposals for neutrino searches, both from existing and new facilities [20].

Concerning the energy range, of course the highest energies are provided by astroparticle searches. Since neutrinos interact only with weak interactions, they are not deflected in magnetic fields and rarely absorbed, making them an ideal messenger to study astronomical sources. Current neutrino observatories, like IceCube [21], are collecting neutrino data at very high energy (above 10 TeV).

On the other side, data acquired from artificial neutrinos cover lower energies, but allow for more control on the intensity and spectrum of the source. Neutrino interactions have been measured in the energy regime below 350 GeV.

Again, the CERN high-energy accelerator chain provides a suitable environment for high intensity and high energy neutrino searches. In order to scope the largest energies possible, detectors for neutrinos produced at LHC are currently being designed. There, proton collisions produce copiously neutrinos and antineutrinos of all flavours at TeV-energy, but at the present no neutrinos at colliders have been observed. The main challenges are that the highest energy neutrinos, which have the largest probability to interact, are produced along the beam lines, where the collider detectors are blind. Even at about 200 m from the Impact Point, the radiation background has been proven [22] to be too high for a neutrino detector. Therefore, the next detectors will be placed at a very far distance from the collision, with FASER-nu [23] and SND@LHC [24] proposed to be located at 480 m from the ATLAS Impact Point.

The beam dump facility designed for the SHiP experiment would provide an unprecedented spectrum of neutrinos, even with energies still limited to a few hundreds of GeV. Indeed, thanks to an high intensity and an high energy proton beam impinging on a target, a high flux of neutrinos and anti-neutrinos can be expected. In this section, the physics potential of these searches is reported.

1.4.3 Tau neutrino cross section

The tau is the neutrino flavour with the less known interaction cross section, due to the much lower number of detected events.

The DONUT collaboration observed a total of 9 tau neutrino events, with a background of 1.5 events. Since the experiment was unable to distinguish between tau neutrinos and antineutrinos, an average CC cross

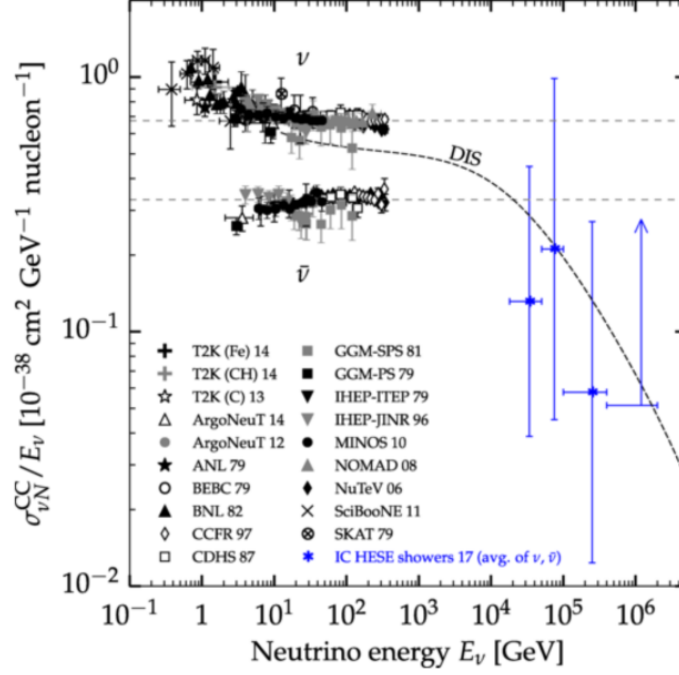


Figure 1.8: Existing data on νN CC scattering cross sections, where N refers to an isoscalar nucleon in target [25].

section was reported [26]:

$$\sigma_{\nu_l} = \sigma_{\nu_l}^{const} \cdot E \cdot K(E), \quad l = e, \mu, \tau, \quad (1.10)$$

where E is the neutrino energy, $K(E)$ describes the kinematic suppression due to the tau mass and $\sigma_{\nu_l}^{const} = (0.39 \pm 0.13 \pm 0.13) \times 10^{-38} \text{ cm}^2 \text{ GeV}^{-2}$, comparable to the average of ν_μ and $\bar{\nu}_\mu$ cross sections.

More recently, the OPERA experiment performed the first measurement of ν_τ CC cross section with a negligible contamination of $\bar{\nu}_\tau$. The final results [9] reported the observation of 10 tau neutrino events, from which the following averaged CC cross section of neutrino over lead was measured:

$$\langle \sigma \rangle_{meas} = 5.1_{-2.0}^{+2.4} \times 10^{-36} \text{ cm}^2, \quad (1.11)$$

where the average is performed on the tau neutrino flux, obtained from the muon neutrino flux produced at the CNGS and the probability of $\nu_\mu \rightarrow \nu_\tau$ oscillations. The measured value is compatible with the prediction from Monte Carlo simulations.

Both measurements are affected by large uncertainties. The detection of

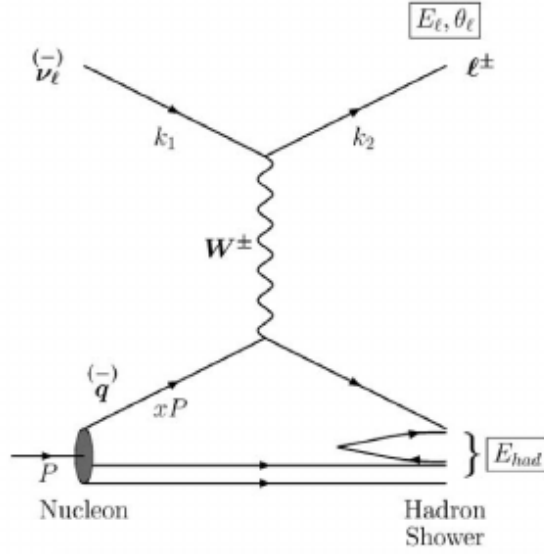


Figure 1.9: Feynman diagram for a charged current deep inelastic neutrino scattering. In the parton model, the constituent of the nucleon involved in the interaction has a fraction x of the nucleon's momentum.

a large number of tau neutrino interactions would allow a more accurate measurement of the cross section, leading to a deeper knowledge of the physics at the basis of the interaction.

In the CCDIS interaction the tau neutrino scatters off a quark in the nucleon, exchanging a W^\pm boson with four-momentum q . The interaction breaks up the nucleon, leading to an hadronic final state X :

$$\nu_l(k_1) + N(p) \rightarrow l(k_2) + X(p_1). \quad (1.12)$$

The kinematics is conventionally studied with the following Lorentz-invariant quantities: the Bjorken- x

$$x = \frac{Q^2}{2p \cdot q} \quad (1.13)$$

and the inelasticity y

$$y = \frac{p \cdot q}{p \cdot k_1} \quad (1.14)$$

Using these variables, the tau neutrino and anti-neutrino DIS cross-sections can be written as follows:

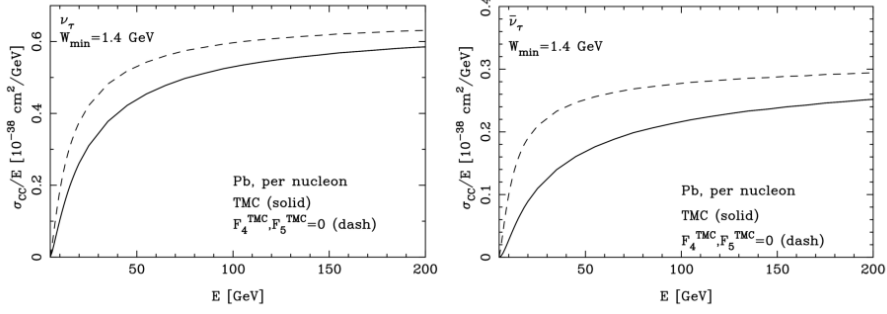


Figure 1.10: ν_τ and $\bar{\nu}_\tau$ CCDIS cross sections predicted by the SM (solid) and in the $F_4 = F_5 = 0$ hypothesis (dashed) [28].

$$\frac{d^2\sigma^{\nu(\bar{\nu})}}{dxdy} = \frac{G_F^2 M E_\nu}{\pi(1 + Q^2/M_W^2)^2} \left((y^2 x + \frac{m_\tau^2 y}{2E_\nu M}) F_1 + \left[(1 - \frac{m_\tau^2}{4E_\nu^2}) - (1 + \frac{Mx}{2E_\nu}) \right] F_2 + \right. \\ \left. \pm \left[xy(1 - \frac{y}{2}) - \frac{m_\tau^2 y}{4E_\nu M} \right] F_3 + \frac{m_\tau^2 (m_\tau^2 + Q^2)}{4E_\nu^2 M^2 x} F_4 - \frac{m_\tau^2}{E_\nu M} F_5 \right), \quad (1.15)$$

where the plus sign applies to neutrino scattering, and the minus one to antineutrino scattering. M and m_τ are the nucleon and τ lepton masses, respectively, M_W is the W boson mass and E_ν is the initial neutrino energy. The F_i ($i=1..5$) terms are the structure functions, which depend on both x and Q^2 . The last two, F_4 and F_5 are multiplied by a factor $\frac{m_\tau^2}{E_\nu M}$, thus their contribution is significant only for the tau lepton, and suppressed otherwise. At the leading order, their value is expressed by Albright-Jarlskog relations [27]:

$$F_4 = 0 \quad (1.16)$$

$$2xF_5 = F_2 \quad (1.17)$$

At Next to Leading Order level, however, $F_4 = 1\%F_5$. If the two structure functions F_4 and F_5 are assumed to be 0, both ν_τ and $\bar{\nu}_\tau$ CCDIS cross sections are enhanced, thus resulting in a larger number of expected tau neutrino interactions. Figure 1.10 shows that the difference is larger at low energies: for $\sigma_{\nu_\tau}^{CCDIS}$, at $E = 20$ GeV the value in the $F_4 = 0$ and $F_5 = 0$ assumption is 30% larger than the one when their contribution is taken into account, whereas at $E = 200$ GeV the F_4 and F_5 contribution reduces the cross section of only 7%. A similar energy dependence can be observed for

the anti-neutrino cross section.

1.4.4 Neutrino magnetic moment

The study of the electromagnetic properties of neutrinos can directly probe many fundamental aspects of particle physics. In the Standard Model, a neutrino at tree level has zero electric charge and zero electric dipole and magnetic moments. Nevertheless, nonzero electromagnetic factors appear from loop corrections, where a neutrino transforming into a lepton radiates a W boson, which then couples to the produced lepton to give back the initial neutrino. However, the resulting magnetic moment is proportional to the neutrino mass

$$\mu_\nu = \frac{3eG_F}{8\pi^2\sqrt{2}}m_\nu \sim 3.2 \times 10^{-19} \left(\frac{m_\nu}{1 \text{ eV}} \right) \mu_B, \quad (1.18)$$

with μ_B being the Bohr magneton, leading to a value too small to be measured in laboratory experiments. Thus, observation of a nonzero neutrino magnetic moment would indicate new physics beyond the SM. It can also be used to distinguish between Dirac and Majorana neutrinos, due to the different nature of the 3×3 matrix of dipole magnetic moments μ_{ij} , which in the Majorana hypothesis is antisymmetric and can have nonzero values only in the off-diagonal terms [29].

In various extensions of the SM, the magnetic moment of the neutrino is expected to fall within the range $\mu_\nu = (10^{-11} - 10^{-12})\mu_B$ for the Majorana neutrino and $\mu_\nu < 10^{-14}\mu_B$ for Dirac neutrinos. Therefore, experimental observations of a neutrino magnetic moment larger than $10^{-14}\mu_B$ would provide evidence of the Majorana neutrino.

Currently, the most stringent limits on the neutrino magnetic moment are $\mu_{\nu_e} \leq 2.9 \times 10^{-11}\mu_B$ (from the GEMMA [30] experiment) for electron neutrinos and $\mu_{\nu_\mu} < 6.8 \times 10^{-10}\mu_B$ (from the LSND [31] experiment). Still due to the low number of detected tau neutrinos so far, the limit on the tau neutrino magnetic moment is much less stringent [32]:

$$\mu_{\nu_\tau} < 3.9 \times 10^{-7}\mu_B \quad (1.19)$$

A wide parameter space remains thus unexplored for tau neutrino magnetic moment.

Experimentally, the neutrino magnetic moment can be observed as an

increase in the cross section $\sigma_{\nu e}$ for elastic scattering of neutrino on electron, which involves only neutral current interactions in the SM. This increase is expressed by an additional term in the energy distribution (T) of the scattered electron in the laboratory frame [33]:

$$\sigma(\nu e, \bar{\nu} e)|_{\mu_\nu} = \frac{\pi\alpha_{em}^2\mu_\nu^2}{m_e^2} \left(\frac{1}{T} - \frac{1}{E_\nu} \right). \quad (1.20)$$

Background events consist of ν -nucleon scattering, which can be suppressed by requiring a kinematic constraint on the angle between the incoming neutrino and the scattered electron [34]:

$$\theta_{\nu-e}^2 < \frac{2m_e}{E_e}, \quad (1.21)$$

which is $\theta_{\nu-e} < 30$ mrad for electron energies of about 1 GeV.

1.4.5 Neutrino induced charm production

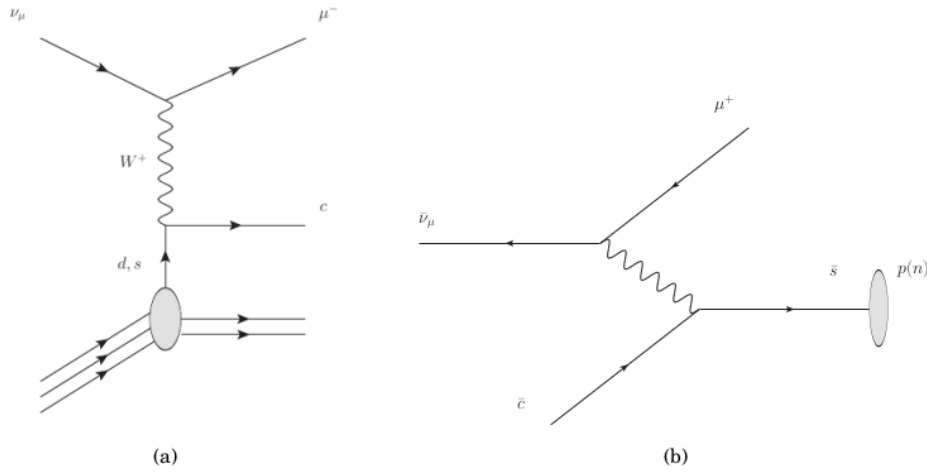


Figure 1.11: Neutrino and anti-neutrino induced charm production diagrams.

A few percent of high energy neutrino and anti-neutrino interactions produce charmed particles. From the first discovery of this production in 1974 [35], this event is identified by looking for two muons of opposite charge, in the final state, usually requiring a 5 GeV cut on the minimum momentum, to reduce background from pion decays.

Diagrams of charm production induced by neutrinos and anti-neutrinos are shown in Figure 1.11. Collecting a large statistics of anti-neutrino in-

duced charm production events leads to a deeper understanding of the anti-strange quark content of the nucleon. Indeed the $s \rightarrow c$ transition, even if favored by CKM matrix, is suppressed with respect to the $d \rightarrow c$ transition, due to the d being a nucleon valence quark. On the other side, both \bar{d} and \bar{s} are sea quarks, therefore the $s \rightarrow c$ transition is above 90% in anti-neutrino scattering.

Another physics application is the detection of pentaquark charm states. The possibility of detecting such states in neutrino-induced charm production events has been shown in literature [36]. The search for these pentaquarks has found renovated interest in this period, after the observation of P_c^+ pentaquark states with charm content by the LHCb collaboration [37].

Chapter 2

Design of the SHiP experiment

SHiP (Search for Hidden Particles) is a proposed experiment to search for new weakly interacting particles in a new Beam Dump Facility (BDF). The proposed facility will be located at CERN, receiving beams of 400 GeV protons from the SPS accelerator. Even if the specifications of the BDF are mainly driven by the requirements of the SHiP experiment, the facility is designed as a multipurpose, large-scale experimental program.

The SHiP setup consists of a high density proton target, followed by a hadron stopper and an active muon shield. Two main detector areas can be identified: the Scattering and Neutrino Detector (SND) and the Hidden Sector (HS) decay spectrometer. The SND is designed to search for light dark matter scattering and neutrino interactions, and the HS spectrometer aims at measuring the visible decays of Hidden Sector particles, by reconstructing their decay vertices in a long vacuum volume. The layout is shown in Figure 2.1.

This chapter presents an overview of the different components of the SHiP experiment, describing their structure and function. If not explicitly stated otherwise, layouts and performances are updated to the Comprehensive Design Study [38] and the previous Progress Report [39].

SHiP formed an official collaboration shortly after the submission of an Expression of Interest in 2013. Today it consists of 50 institutes and the four associated institutes from 18 countries, CERN, and JINR.

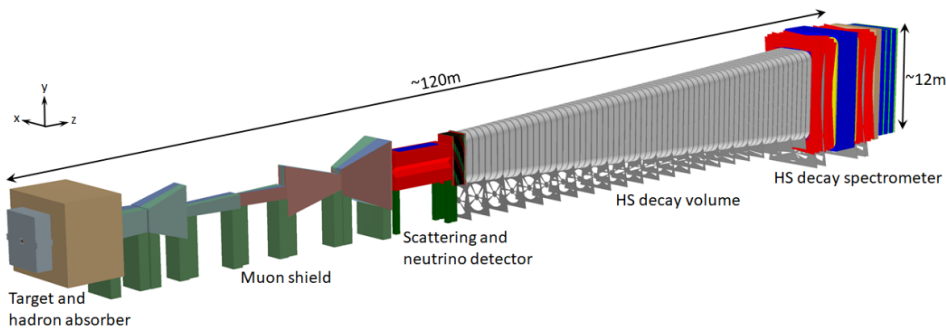


Figure 2.1: Global overview of the SHiP experiment.

2.1 The Beam Dump Facility

2.1.1 Location and beam delivery

The proposed Beam Dump Facility is foreseen to be located in the North Area of the Super Proton Synchrotron (SPS). The designed complex is a 120 m long underground experimental hall, with a width of 20 m. The implementation is based on minimal modifications of the complex, using as much as possible already existing accelerator and beam lines. It is planned to re-use about 600 m of the present transfer line TT20, which already serves other North Area facilities. A new splitter/switch will then deflect the beam into a new dedicated 380 m long section of beam line (TT90), which will finally deliver the beam to the target, as shown in Figure 2.2.

The SHiP Collaboration needs for its physics case a total of 2×10^{20} protons on target in five years of data taking. In order to reduce the probability of combinatorial background events from residual muons entering the decay volume, and to respect the limits of instantaneous beam power deposited in the target, the proton beam should be provided via a slow extraction of a duration of 1.0 s. At each spill, a total of 4×10^{13} protons on target can be collected. The duration of the SPS cycle has been computed to be 7.2 s.

A slow beam extraction at the specific length of 1.0 s has been demonstrated with a dedicated test [40], performed at the SPS with the lower intensity of about 10^{12} protons. A display from this test is reported in Figure 2.3.

The next objective is to improve the extraction technology, in order to

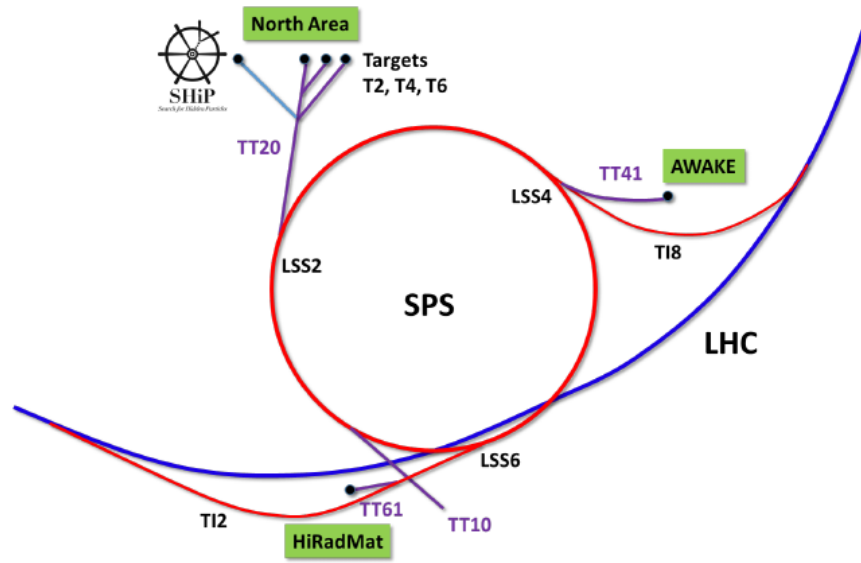


Figure 2.2: Schematic layout of the SPS and its associated facilities. The planned additional beam line for the BDF is reported [40].

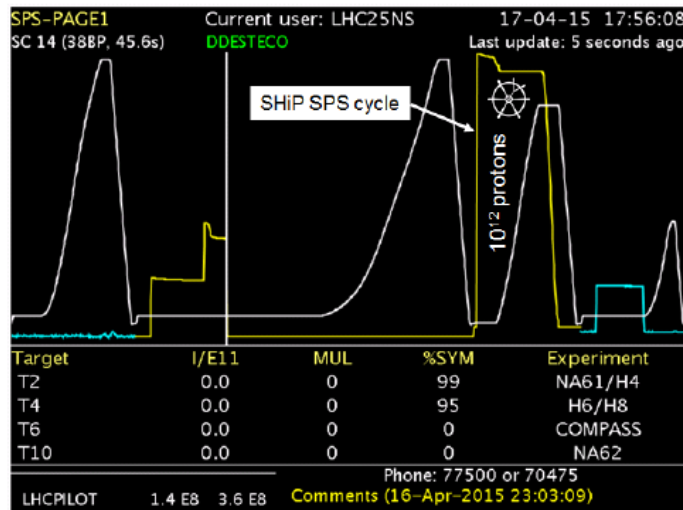


Figure 2.3: Display from a slow beam extraction test for the Beam Dump Facility. The yellow line represents the proton beam intensity in the SPS and the white line represents the beam energy [40].

minimize the inherent beam losses, which would limit the proton intensity due to the risk of radio-activation of the extraction region and radiation damage. Technologies under study are either a passive beam scattering device, which consists of a high-Z blade designed to spread the beam, or a thin bent crystal, which would channel away the misdirected protons. Testing these technologies in 2018 resulted in a loss reduction of a factor four, allowing for a safe extraction of 5.0×10^{19} protons per year. Therefore, the SHiP requirement of 4.0×10^{19} protons on target per year can be achieved, at the same time addressing the beam needs of the other facilities at the North Area.

2.1.2 The target

A dense target will be the core of the beam dump facility, with two main functions:

- producing as many charm and beauty hadrons as possible, as well as photons, all of which are potential sources of very weakly coupled particles;
- absorbing safely and reliably the energy of the proton beam. Moreover, pions and kaons should be absorbed before their decay, to minimize the muon and neutrino background.

Thus, the target should be long, and made of a material with the highest possible atomic mass and atomic charge. The SPS beam is foreseen to deposit on target 320 kW of average power and 2.56 MW, over the 1 s slowly extracted spill [41]. Thus, the target has been designed to bear large thermal and structural loads, for at least five years of operation, in order to provide the total of 2×10^{20} protons on target required by the SHiP physics case.

As shown in Figure 2.4, the designed target is a hybrid assembly, consisting of several collinear cylinders, with a diameter of 250 mm. The materials are TZM (0.08% titanium-0.05% zirconium-molybdenum) alloy and pure tungsten. The thickness and material of each block has been optimized, according to the energy deposition at a given depth.

Two main sections can be identified: the downstream section uses pure tungsten, since it satisfies all the physics requirements (high atomic number

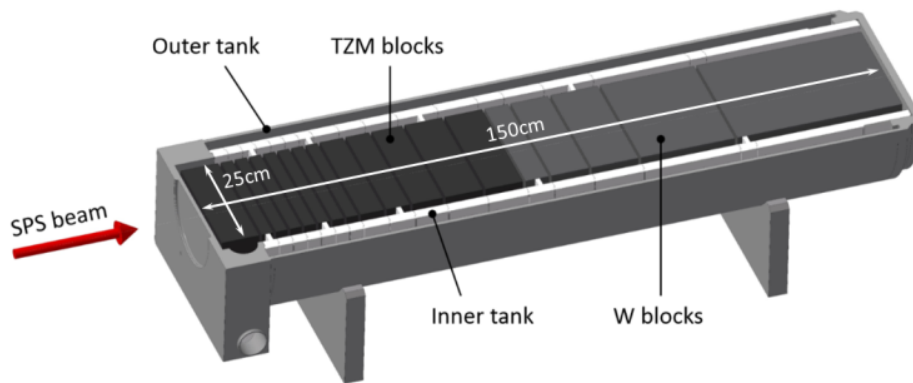


Figure 2.4: Layout of the BDF target assembly, showing the TZM and the tungsten blocks, together with the beam direction.

and short interaction length). However, this material cannot be adopted for the whole target, due to the excessive stress that would be present in the first part. There, the TZM alloy is adopted, since its lower density allows for lower energy deposition, but the material is still dense enough to fulfill the requirements of the experiment [42]. The usage of this alloy, instead of pure molybdenum, has been driven by the requirements of higher strength, better creep resistance and higher recrystallization temperature.

The target needs to be actively cooled: the required cooling can be provided via the circulation of a high velocity water stream, through 5 mm gaps, placed between different target blocks. In order to avoid the resulting corrosion of the material, the blocks should be coated with Ta2.5W[(2.5% tungsten-tantalum alloy)].

Figure 2.5 illustrates the maximum deposited energy density, normalized per proton impact on target, calculated from a FLUKA [43, 44] Monte Carlo simulation. The highest values correspond to the coating layers, due to the higher density of the tantalum alloy. On the other side, the lowest values correspond to cooling gaps. An energy increase passing from TZM to W can be seen, after a vertical line drawn between the two regions.

2.1.3 Hadron absorber and active muon shield

A primary requirement of the facility is to operate in an environment of extremely low background from ordinary physics processes. All Standard Model particles must be taken into account for background evaluation. Pions and kaons need to be absorbed before they decay, in order to minimize

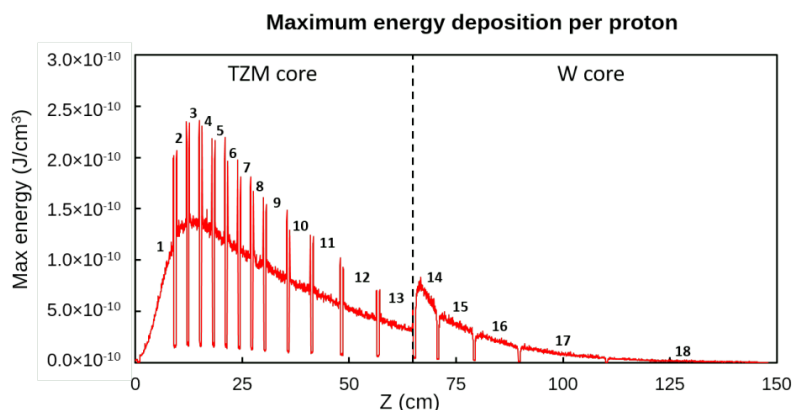


Figure 2.5: Maximum deposited energy density per proton in the target, as obtained from a Monte Carlo simulation [41].

the production of neutrino and muon background from their decay products: an iron absorber is placed to contain the background radiation and hadrons emerging from the proton target, covering a thickness of 5 m.

A different strategy must be adopted for muons, which are more penetrating. The total flux of muons with momentum larger than 1 GeV/c has been estimated to amount to $O(10^{11})$ muons per spill of 4×10^{13} protons. The muon spectrum arrives to a momentum of 350 GeV/c and a P_T of 8 GeV/c. To make background from random combinations and deep inelastic scattering negligible, the muon flux should be reduced by at least six orders of magnitudes. Thus, an active muon shield has been designed, to deflect muons out of the acceptance of downstream detectors.

Making a section of the hadron absorber itself magnetized allows to reduce the whole length required for the actual muon shield. Of course, not all the hadron absorber can work as a magnet, since the active field would interfere with the instrumentation of the target system, aside for the technical difficulties of the installation of the required coil. Still, a magnetic field of 1.6 T over 4.5 m can be achieved, by using multiple coils, powered and cooled independently to ensure redundancy.

The active muon shield itself starts with a first set of magnets, with enough length to separate both muon charges to either side of the z-axis. For a 350 GeV/c muon, assuming a field in the iron of 1.8 T, a requirement of a ~ 18 m total length has been computed [45]. However, when lower momentum muons traverse the return field of this magnet, they would be sent back towards the detectors, as shown in Figure 2.6 for a 50 GeV/c

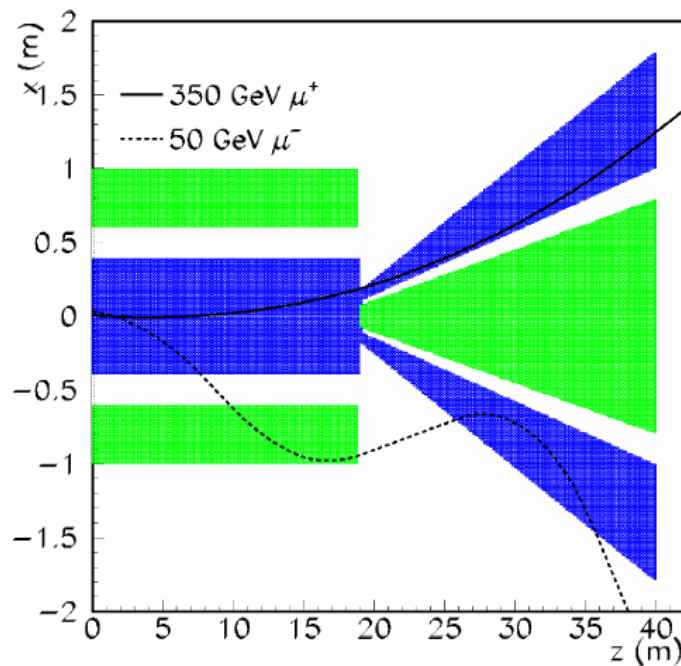


Figure 2.6: Schematic representation of the active muon shield's principle. The paths of a 350 GeV/c muon and a 50 GeV/c muon are also shown [45].

muon. A second set of magnets is therefore needed, with opposite polarity field close to the z-axis, in order to sweep out these muons again.

The optimization of the muon shield resulted in a total length of 35 m and a total weight of 1300 tons of magnets. Concerning the technology, grain-oriented (GO) steel has been proposed, since it allows to achieve high fields with warm magnets. Up to 150 sheets at a time can be welded together into packs of 5 cm depth, which are then bolted into rectangular modules of 50 cm depth. Aligning grains in one dimension allows to produce higher fields with reduced currents and without dedicated cooling. However, the joints between the steel segments need to be carefully realized, in order to ensure the required performances, given the size and complexity of this magnet system.

The impact of the shield can be seen in Figure 2.7, where the muon flux from a FLUKA simulation is reported. The actual shield covers about the first 40 m of the plot, as represented by the black layout.

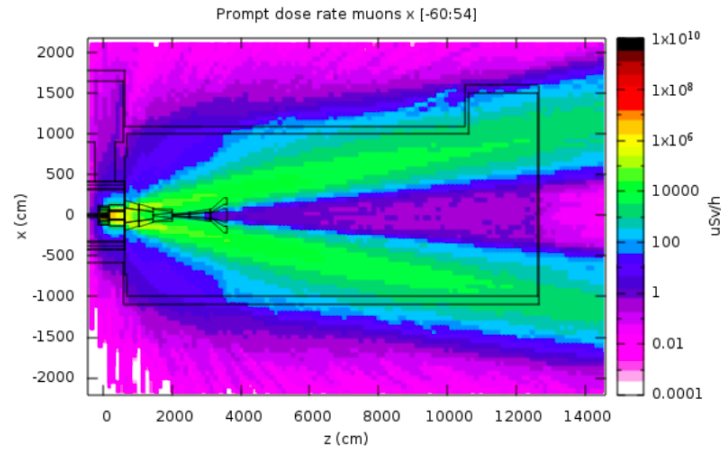


Figure 2.7: Prompt dose rate from muons at the level of the beam axis, illustrating the function of the muon shield. The layout of the magnets is outlined in black [39].

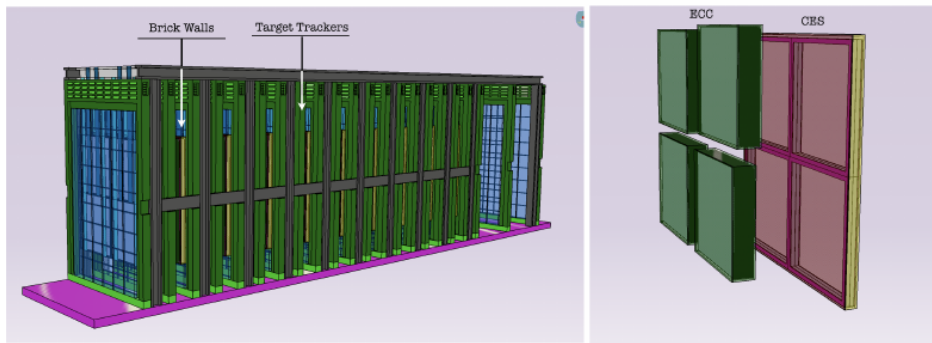


Figure 2.8: Schematics of the Emulsion Target. On the left, the global structure, made of 19 walls. On the right, the composition of a single wall, with the bricks and CES components underlined.

2.2 Scattering Neutrino Detector

2.2.1 Emulsion Target

The Emulsion Target is designed to detect τ leptons and charmed hadrons, by disentangling their production and decay vertices. It is also suited for Light Dark Matter detection, through the direct observation of the scattered electrons.

The target exhibits a modular structure, arranging the emulsions in

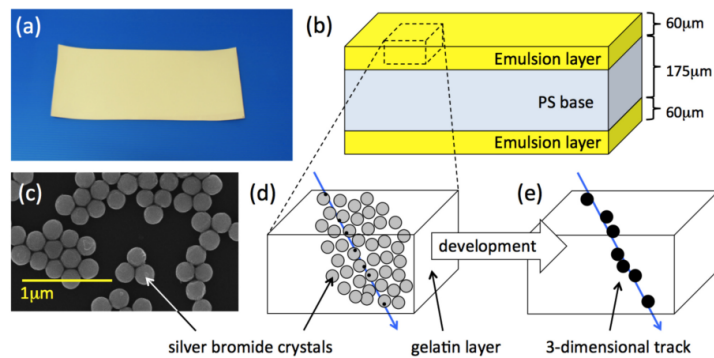


Figure 2.9: Illustration of the principle of particle detection with nuclear emulsions: (a) is a picture of the nuclear emulsion, while (b) shows its internal structure. The silver bromide crystals themselves are seen in an electron microscope image in (c). The diameter of crystals is approximately 200 nm; (d) and (e) illustrate the principle of detection of a charged particle in the nuclear emulsion. Black small dots on silver bromide crystals show latent images in (d). From Ref.[46].

“bricks”, employing the Emulsion Cloud Chamber technique (ECC), where the interactions are located and reconstructed, and in Compact Emulsion Spectrometers (CES), designed for charge and momentum measurement. The structure is completed with electronic detectors, called Target Trackers, providing time stamp and matching the tracks reconstructed in the various detector components.

The baseline option involves 19 emulsion brick walls and 19 Target Tracker planes. The walls are divided in 2×2 cells, each with a transverse size of $40 \times 40 \text{ cm}^2$, as illustrated in Figure 2.8.

Nuclear emulsion unit cell

Nuclear emulsions are made of AgBr crystals, dispersed in a gelatine binder. Since the crystals are semiconductors with a band gap of 2.6 eV, the transit of a charged particle produces electron-hole pairs, with the Ag atoms working as latent images. After a dedicated chemical development of the emulsion, the number of silver atoms multiplies and the size of silver grains increases from 0.2 μm to 0.6 μm . Finally, the trajectory of the particles can be seen with an optical microscope. The whole process is reported in Figure 2.9.

Each emulsion film is made of two active layers, poured on the two sides of a plastic base. This configuration provides high tracking performances,

with sub-micrometric position and milliradian angular resolution. Nuclear emulsion films are produced by Nagoya University in collaboration with the Fuji Film Company and by the Slavich Company in Russia.

The unit cell employs the Emulsion Cloud Chamber technique (ECC), largely exploited by the OPERA experiment, which consists in interleaving layers of passive material with emulsion films, acting as tracking devices. The single unit, also called “brick”, is made of nuclear emulsion films, interleaved with 1 mm thick passive layers, with a transverse size of $40 \times 40 \text{ cm}^2$. The proposed materials for the passive layers are either a lead or a tungsten alloy, and each brick covers ~ 10 radiation lengths. According to the current estimate of the background flux, the emulsion films must be replaced twice a year, in order to contain the integrated number of tracks within 10^5 particles/cm², and not to spoil the reconstruction performance.

Compact Emulsion Spectrometer

The Compact Emulsion Spectrometer (CES) aims at measuring the electric charge and momentum of hadrons produced in τ lepton decays, allowing to disentangle ν_τ and $\bar{\nu}_\tau$ charged current interactions, even in hadronic decay channels. It is also required to measure the momentum of soft muons which, being emitted at large angles, would not reach downstream detectors.

The CES is made of a sandwich of three emulsion films interleaved by two layers of air gaps, attached immediately downstream of each ECC brick (Figure 2.10). The momentum is measured from the curvature in a magnetic field, via the sagitta method. The two-dimensional sagitta $s = (s_x, s_y)$ is the distance between the track position in the middle plane and the intercept in this sheet of the straight line, joining the track positions in the two external planes. Assuming a magnetic field directed along the y axis, the x component of the sagitta reflects the curvature, while the y component reflects the effects of multiple coulomb scattering. Since the reconstruction in this spectrometer requires a lower level of background tracks with respect to the ECC bricks, the emulsion films in the CES need to be replaced more often, and the required frequency of these replacements is currently under study.

A prototype with air gaps between emulsion films has been tested in 2017 at the CERN PS, using a vertical 1 T magnetic field and π^- beams,

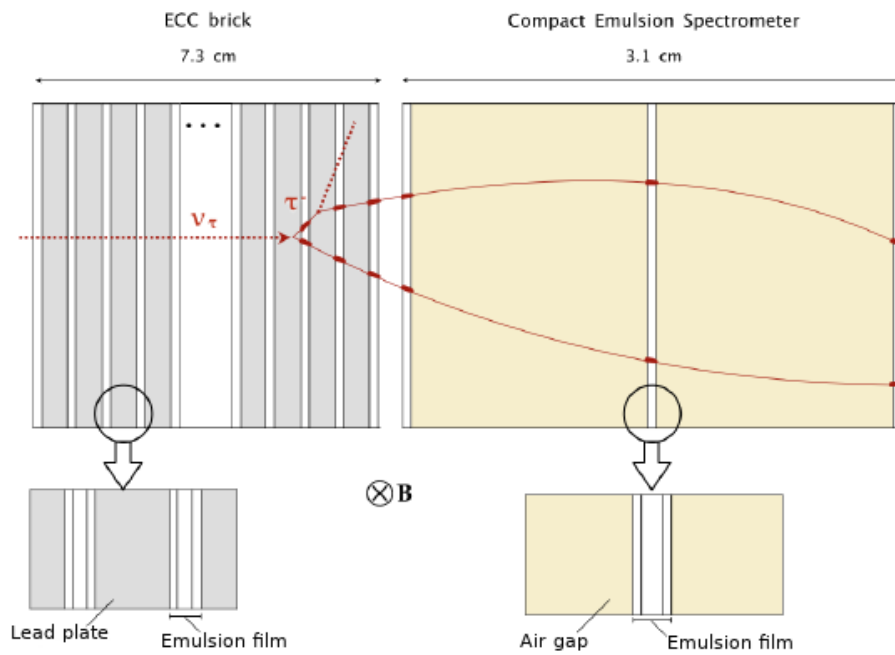


Figure 2.10: Schematic representation of the target unit: the brick on the left, the Compact Emulsion Spectrometer on the right.

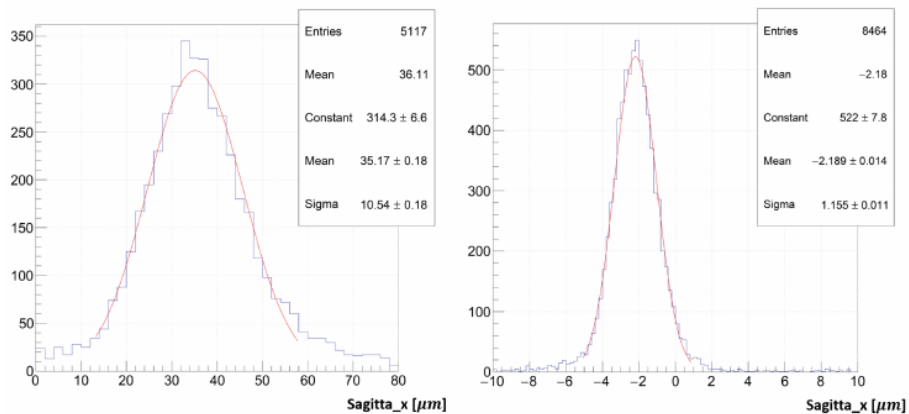


Figure 2.11: Measured sagitta along the x axis for 1 GeV (left) and 10 GeV (right) pions. Magnetic field is along the y axis [39].

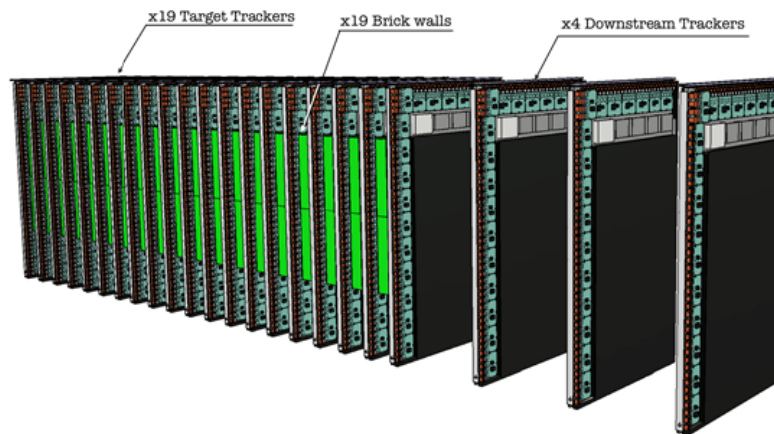


Figure 2.12: Illustration of the instrumentation of Target Trackers and Downstream Trackers.

with momenta ranging from 1 to 10 GeV/c. The results are reported in Figure 2.11. The distributions of the measured sagitta along the x-axis for 1 GeV/c and 10 GeV/c show Gaussian peaks with σ of $10.5 \mu\text{m}$ and $1.15 \mu\text{m}$, respectively. A very good agreement has been observed in the whole momentum range, with a momentum resolution of $\sim 30\%$ up to 10 GeV/c.

Target Trackers and Downstream Trackers

A system of electronic detectors in combination with the ECCs is needed to provide the time stamp of the events reconstructed in the emulsion bricks and to connect the emulsion tracks to the downstream detectors.

A set of 19 Target Tracker planes is placed within the target, complementing each brick wall with a plane. The first plane precedes the first brick, thus acting as a veto for charged particles entering the Emulsion Target. Additional planes of electronic detectors are located downstream to measure momentum and charge, working as a second spectrometer to complement the Compact Emulsion Spectrometer for penetrating charged tracks, especially muons. They are usually referred to as Downstream Trackers: the layout of the whole system is shown in Figure 2.12.

The tracking chambers must satisfy very stringent requirements: a single plane should have a total thickness within 5 cm and a flat surface to get a good planarity and uniform tracking performances. Furthermore, a position resolution better than $100 \mu\text{m}$ in both coordinates and a high efficiency

(> 99%) for angles up to $\pi/4$ are needed, to ensure an efficient vetoing of background muons. Finally, the time stamps require a resolution better than 10 ns.

The baseline option consists of Scintillating Fiber trackers (SciFi). The active planes are composed of several fibre layers, glued together to form fibre mats of 1.5 mm thickness. The fibre mats are glued on supports made of carbon fibre honeycomb structures, forming a large detector surface and ensuring a spatial resolution of $50 \mu\text{m}$ over a surface of $\sim 1 \text{ m}^2$, containing the total thickness within 15 mm.

The active area of the SciFi planes is $917 \times 1440 \text{ mm}^2$, larger than the size of the ECC and the CES, in order to follow particles in several consecutive walls downstream of the ECC in which the interaction occurred, even if they are emitted at large angles. The full dimension of the target tracker modules is $930 \times 1500 \text{ mm}^2$, just barely larger than the active area. A first prototype of this detector has been tested during two exposures, in 2018 and 2019.

2.2.2 Target Magnetization

The SND spectrometer requires to magnetize a 10 m^3 volume with a field gradient of at least 1.2 T, at an acceptable power consumption and a low stray field to avoid influencing the muon flux deflected from the muon shield. Furthermore, the magnet must operate at a temperature of 18°C , to ensure optimal condition to the nuclear emulsion films.

A comprehensive design of the magnet has been conducted in the last years, including the magnetic, electrical, thermal and structural aspects. It is based on a water-cooled warm magnet, using either copper or aluminum as a coil and producing a uniform magnetic field of 1.25 T with $\Delta B/B < 1\%$ in the detector volume. At a current density of 3.2 A/mm^2 and an excitation current of $\sim 10 \text{ kA}$, the total power consumption is $\sim 1 \text{ MW}$. The details of the designed magnet are reported in Ref.[47].

Due to the needed emulsion film replacements, an opening and closing mechanism of the magnet has been developed. This procedure relies on opening one of the side walls of the yoke through an hydraulic system with the help of floor rails, which are shown in Figure 2.13. The complete procedure to replace the emulsion bricks should take no more than a day.

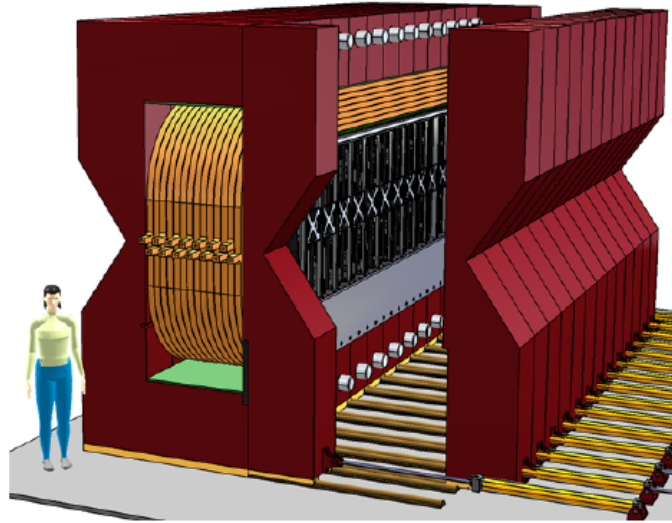


Figure 2.13: Layout of the SND spectrometer magnet, showing the opening mechanism for the replacement of the emulsion films.

2.2.3 Muon Tracker

The SND muon identification system aims at detecting muons produced in neutrino interactions from the Emulsion Target. It works as a filter, made of 8 iron layers. The thickness must be large enough to absorb hadrons produced in the neutrino interactions, at the same time minimising the production of additional background for Hidden Sector search in downstream detectors. The current design involves four iron layers of 15 cm thickness, followed by smaller four iron layers of 10 cm thickness. The layout is shown in Figure 2.14.

The muon tracking planes are Resistive Plate Chambers (RPCs), operated in avalanche mode to cope with the significant particle rate. Each RPC station is composed of three gaps with an active area of $1900 \times 1200 \text{ mm}^2$ each. The planes are read via orthogonal strip panels with $\sim 1 \text{ cm}$ pitch and they are staggered by $\pm 10 \text{ cm}$, to compensate from the acceptance losses due to the dead areas between adjacent gaps in the same plane. The overall transverse dimension of one plane is $4290 \times 2844 \text{ mm}^2$.

The muon filter is followed by a veto tagger, designed to detect the charged particles produced in the iron layers, thus identifying them as a background source for the Hidden Sector detectors downstream. A good timing resolution, around 300 ps, is needed to avoid losses in the signal efficiency caused by a longer veto gate.

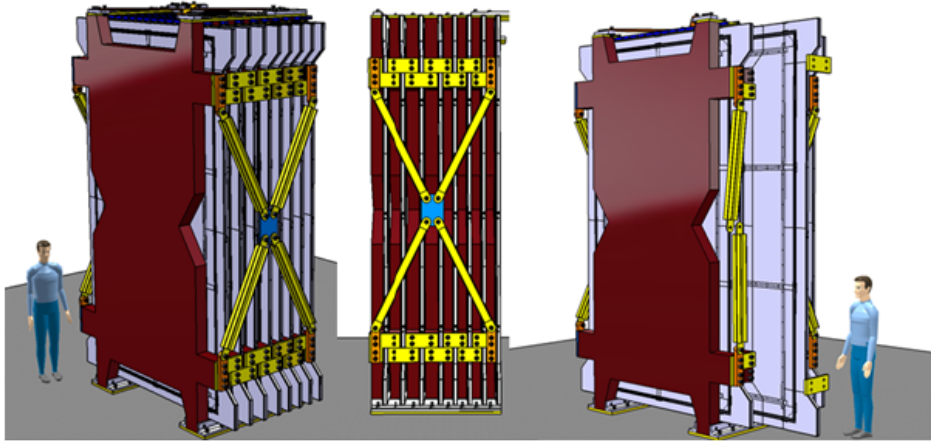


Figure 2.14: Layout of the SND muon identification system. The RPC and iron layers are visible.

The tagger planes are instrumented with two gas gaps of Multigap Resistive Plate Chambers (MRPCs), each composed of five MRPC modules arranged vertically, in order to cover the vacuum vessel entrance window. The modules are staggered by 20 cm to avoid dead zones due to the frames. An efficiency of 90% can be achieved, only limited by the space required for the pick-up electrode.

2.3 Hidden Sector detector

The Hidden Sector detector searches for evidence of decays of long-lived particles, coming from the upstream proton target. It is therefore needed to reconstruct the decay vertex, to measure the invariant mass of the decayed particle, and to identify the final state. The decay search should not require the assumption of pointing and timing, which can instead be used for background control.

A schematic layout of the Hidden Sector detector is shown in Figure 2.15. The particle is let to decay in a dedicated vacuum vessel, which is followed by a magnetic spectrometer for momentum measurement and a particle identification system.

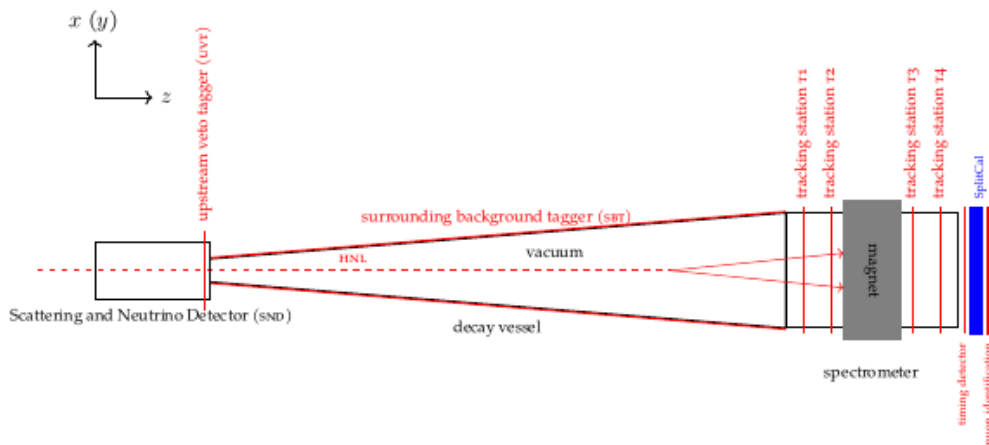


Figure 2.15: Schematic diagram of the Hidden Sector detector (not to scale). An HNL decay is shown, as an example of HS decay topology [48].

2.3.1 The decay vessel

The design of the decay vessel involves a large 50 m long decay volume, with a pyramidal frustum shape. The transverse outer dimensions are $2.2 \times 5.0 \text{ m}^2$ for the upstream section, immediately following the scattering and neutrino detector, and $5.9 \times 11.9 \text{ m}^2$ for the downstream section, before the HS detectors.

Deep inelastic neutrino-nucleon scattering in the detector volume leads to background events through production of V^0 particles (K_L, K_S, Λ), whose decay can mimic the topology of a hidden particle decay. To suppress this background source, the vessel must be kept under vacuum, at a pressure of less than 10^{-2} bar. The actual vacuum area extends throughout the downstream spectrometer magnet, to avoid the presence of a significant amount of material in the spectrometer magnet. The total volume under vacuum amounts thus to 2040 m^3 .

Background comes from neutrino and muon interactions in the upstream Scattering and Neutrino Detector or in walls of the decay volume. These interactions should be excluded by completely covering the decay volume section with a high efficiency Surround Background Tagger system, aimed at detecting the charged particles produced. The instrumentation of this system can employ a liquid scintillator detector or a plastic scintillator. Test beam measurements in the last years have demonstrated that a muon detection efficiency of at least 99.6% and a time resolution of 1 ns can be achieved.

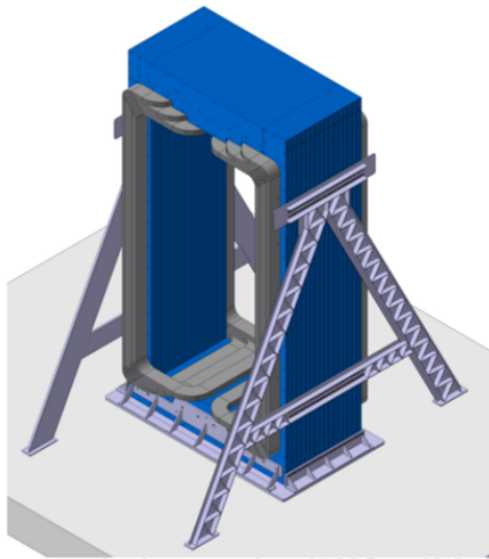


Figure 2.16: Layout of the Hidden Sector Spectrometer magnet.

2.3.2 Hidden Sector Spectrometer

Tracking and momentum reconstruction of the charged daughters of hidden particle decays are dedicated to the Spectrometer Straw Tracker. This system is a magnetic spectrometer, employing a large aperture dipole magnet and two tracking telescopes, one on each side of the magnet and composed of two tracking stations. The four tracking stations are identical, with a transverse nominal acceptance of $5 \times 10 \text{ m}^2$, and they are based on ultra-thin straw drift tubes. Each station consists of four views, arranged as stereo views and with straw diameter $D = 20 \text{ mm}$.

Currently the spectrometer employs a warm normal conducting magnet, shown in Figure 2.16. The magnetic field is about 0.14 T at its maximum, and about 0.08 T at the location of the closest tracker stations.

The required physical performances of this system involve a good vertex quality, along with accurate invariant mass for decay analysis. Moreover, good timing resolution and matching with veto taggers are needed, since the track position should be well extrapolated to the other detectors, in order to exclude combinatorial background.

Several prototype straws have been produced, and current test beam measurements indicate a straw hit resolution of $120 \mu\text{m}$, achievable with high hit efficiency over most of the straw diameter. The results are reported in Figure 2.17.

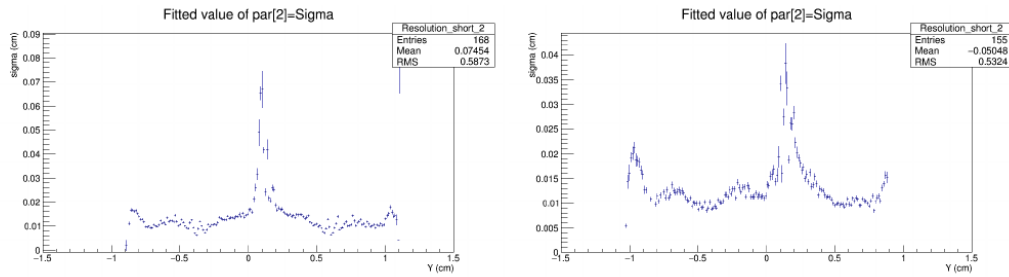


Figure 2.17: Hit resolution for a straw diameter equal to 20 mm. The measurement was performed by requiring no wire offset (on the left) and with a wire offset of 2 mm (on the right) [39].

2.3.3 Calorimeters and Particle Identification

The most downstream section of the SHiP apparatus involves a series of detectors, aimed at providing all the needed measurements for complete reconstruction of the Hidden Sector decay.

A Timing Detector is located outside the vacuum vessel, right after the aluminum endcap of the decay volume. The role of this detector is to provide unambiguous start times to the Spectrometer Straw Tracker. In order to reduce combinatorial muon background to an acceptable level, a timing resolution of ~ 100 ps is required. The covered surface must be $5\text{ m} \times 10\text{ m}$.

Two alternative technologies have been proposed for the timing detector. The first option employs a plastic scintillator, made of staggered scintillator bars arranged in 3 columns and 182 rows, each bar read by an array of 8 Silicon PhotoMultipliers (SiPMs). The timing resolution ranges from 80 ps to 180 ps, depending on the particle position with respect to the bar's sensor. A layout of the timing detector in this configuration is shown in Figure 2.18.

The second option employs the same Multigap Resistive Plate Chamber (MRPC) technology proposed for the Upstream Tagger of the Scattering and Neutrino Detector. A time resolution of less than 60 ps and an efficiency larger than 98% have been demonstrated over a large scale prototype. However, it is still required to prove the multi-hit performance of the MRPC, which is essential for the measurement of the time arrival difference of the HS decay products, if separated by a short distance in the same Timing Detector module.

The Timing Detector is followed by a Split Calorimeter (SplitCal), dedi-

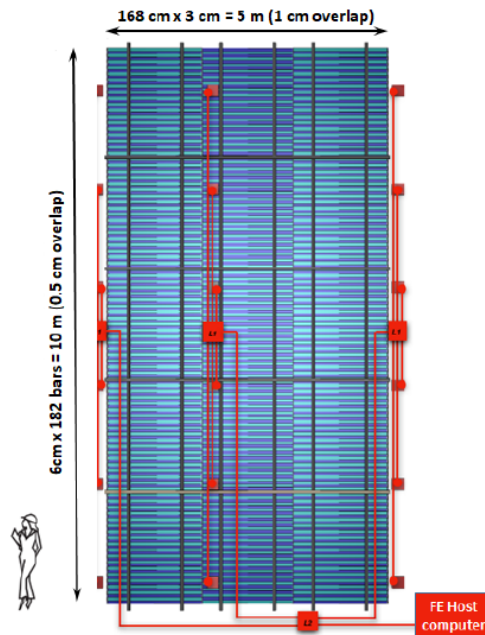


Figure 2.18: Layout of the Timing Detector, in the plastic scintillator option.

cated to energy measurement of decay daughters. It is a sampling calorimeter, made of scintillator planes interleaved by lead blocks. The current design involves 40 absorber and scintillator planes, with a transverse cross-section of $6 \times 12 \text{ m}^2$ and a total depth of 20 radiation lengths.

The calorimeter is divided in two sections, as shown in Figure 2.19: the first section aims at reconstructing the transverse profile at the beginning of the electromagnetic shower, while the latter section is designed to study the shower at its maximum point.

The instrumentation of the SplitCal can be performed with MicroMegas Chambers, acting as high precision layers. The design is similar to the one designed for the upgrade of ATLAS muon system [49], but with a smaller area of $80 \times 80 \text{ cm}^2$. A prototype with this size has been tested at DESY in October 2019.

The most downstream detector of the SHiP apparatus is a muon system, aimed at performing particle identification of the muons coming from Hidden Sector decays. This system is made of four active stations, interleaved by iron filters with a thickness of ~ 3.0 interaction lengths. The stations cover a total active area of 288 m^2 .

The baseline technology consists of scintillating tiles with direct SiPM readout. Organic scintillators have been chosen thanks to their fast re-

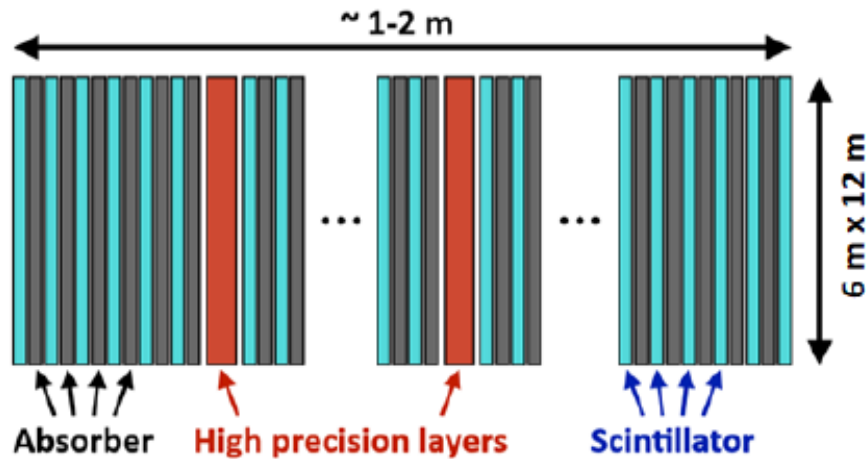


Figure 2.19: Layout of the Hidden Sector calorimeter. The different colors mark separate regions.

sponse (short rise and decay times), along with their high light yield. Moreover, the SiPMs provide good timing, compactness, and high photon detection. Indeed, maximising the photon collection is needed to preserve the optimal time resolution, which is required to be better than 300 ps per station.

2.4 SHiP sensitivity to new physics

2.4.1 Sensitivity to Light Dark Matter

The SHiP Scattering and Neutrino Detector (SND) can probe the existence of Light Dark Matter particles by detecting the recoil electrons coming from elastic scattering in the Emulsion Target. The signal is a single electromagnetic shower, generated from the recoil electron. A sufficient portion of this shower can be reconstructed by the Emulsion Cloud Chamber (ECC) bricks and Target Tracker planes, acting as sampling calorimeters with a total depth of 10 radiation lengths.

Background for this LDM search are neutrino interaction events, with only one reconstructed outgoing electron at the primary vertex, mimicking the signature $\chi e^- \rightarrow \chi e^-$. The main variables to separate signal from background are the electron energy and the angle with respect to the incoming particle detection, which need to be accurately measured from the

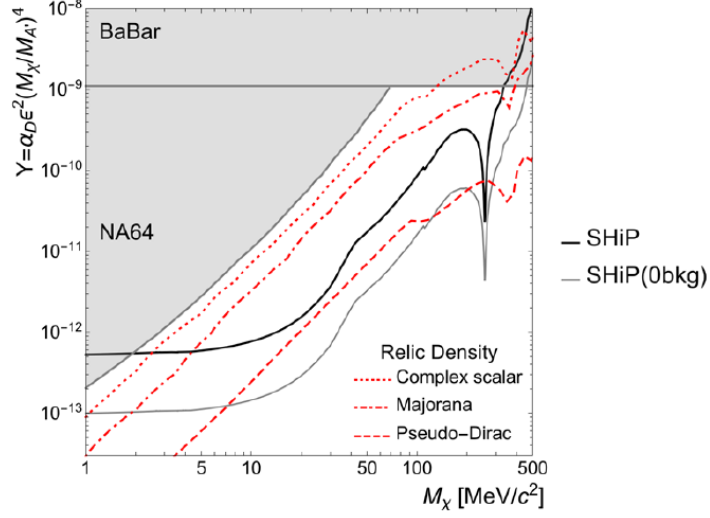


Figure 2.20: SHiP exclusion limits at 90% C.L. as a function of the LDM mass M_X , compared to the current experimental limits [38].

electromagnetic shower reconstruction.

The Light Dark Matter particles are produced by Dark Photon decay, as introduced in section 1.2.2. The considered Dark Photon mass range is $M_{A'} \sim O(1 \text{ GeV}/c^2)$, where significant contributions to its production are from decay of light mesons and from proton bremsstrahlung. Assuming a benchmark scenario with a dark coupling constant of $\alpha_D = 0.1$ and a LDM mass of $M_X = M_{A'}/3$, the SHiP 90% C.L. sensitivity is shown in Figure 2.20, with a predicted background of ~ 800 neutrino events.

2.4.2 Hidden Sector performances

The SHiP experiment is designed as a general-purpose facility, aimed at exploring the physics range of many different models and portals to new physics. The unique peculiarity of the Hidden Sector detection apparatus is the ability to fully reconstruct the decay: the various detectors discussed so far provide vertex reconstruction and invariant mass measurement of the decayed particles, while timing information and pointing to the proton target are necessary tools for background suppression.

Background sources of this search are deep inelastic neutrino and muon scatterings in the detector volume, leading to production of V^0 particles (K_L, K_S, Λ), whose decay can mimic the topology of a hidden particle decay. Moreover, the coincidence of muons from the same spill escaping from the

shield is a source of combinatorial background. The last component of the muon background is the cosmic rays contribution. A comprehensive design of the detector reduced the background to less than 0.1 events over the lifetime of the experiment, thus allowing to focus the sensitivities studies to the detector's acceptance.

In general, the computation of SHiP sensitivity to a new hidden particle requires to know:

- the production rate of the new particle, assuming the planned total number of 2×10^{20} protons of target, in five years of data taking;
- the probability that the decay vertex is located within SHiP decay volume, thus related to the geometrical acceptance of the apparatus;
- the fraction of hidden particle decays resulting in a detectable final state, taking into account both the predicted branching ratios and the detector efficiencies.

2.4.3 Sensitivity to Heavy Neutral Leptons

The SHiP experiment plans to search for Heavy Neutral Leptons in the $O(1\text{ GeV})$ mass range. They are produced from the decay of B and D mesons: beauty decays are the main production mode for HNLs with masses above $2\text{ GeV}/c^2$, while charm decays are the main contribution for lighter masses. Thus, in the light mass range, the spectrum of charmed hadrons produced in the SHiP proton target needs to be known with high accuracy, in order to optimize the detector acceptance for angular and momentum of the produced HNLs.

Sterile neutrinos are unstable due to the mixing with active neutrinos. The decay rate is the typical one for all weak decays, multiplied by the squared mixing angle $U_{\alpha I}$ [5]:

$$\Gamma_{N \rightarrow \text{weak}} \propto |U_{\alpha I}|^2 G_F^2 M_I^5, \quad (2.1)$$

where G_F is the Fermi constant and M_I is the HNL mass. Masses of the final state particles are neglected.

The SHiP experiment looks at the charged particles in the final state of HNL decays, in order to probe sterile neutrino models. The final state from decays of N_2 and N_3 are formed by two charged leptons,

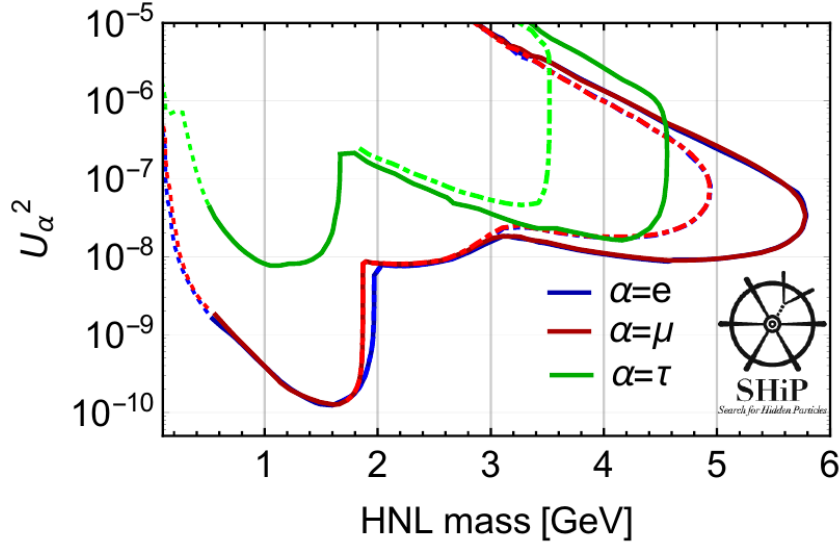


Figure 2.21: SHiP sensitivity curves (90 % C.L.) for HNLs mixing to a single SM flavour: electron (blue), muon (red) and tau (green) [50].

$$N_I \rightarrow e^+e^- \nu, \mu^+\mu^- \nu, \tau^+\tau^- \nu, \mu^\pm e^\mp \nu, \text{ etc.} \quad (2.2)$$

or by hadrons and leptons.

$$N_I \rightarrow \pi^\pm e^\mp, \pi^\pm \mu^\mp, K^\pm e^\mp, K^\pm \pi^\mp \nu, \text{ etc.} \quad (2.3)$$

SHiP sensitivity to these events depends on the relative strength of the HNL coupling to the three SM flavours U_e^2 , U_μ^2 and U_τ^2 . According to which coupling is assumed to be dominant, different scenarios need to be explored. The sensitivity curves for the different flavours are shown in Figure 2.21.

Chapter 3

Neutrino interactions in the Scattering Neutrino Detector

Introduction

One of the main goals of the proposed SHiP experiment is an high precision measurement of the tau neutrino production cross section. The primary neutrino interaction and the following decay of the associated tau lepton need to be clearly identified, and separated from the background mainly coming from neutrino-induced charmed hadrons. The definition and optimisation of the decay search procedure is based on accurate Monte Carlo simulations of both signal and background events in the SHiP Scattering and Neutrino Detector (SND).

The main software framework of the SHiP Collaboration is called FairShip and it is derived from the FairROOT [51] framework. It provides a general interface for a variety of Monte Carlo generators, along with an accurate geometry of all designed detectors.

The following reference system is used:

- the z coordinate follows the beam line, defined as the 400 GeV proton beam provided by the SPS accelerator;
- the y coordinate represents the height. Positive y go towards the ceiling of the experimental hall;
- the x coordinate represents the width. Its verse is given by the other two, assuming a right-handed coordinate system.

The origin is set at the center of the SHiP decay vessel. Since the vessel is placed downstream of the SND detector, all the positions along the z coordinates in this area are lower than zero.

3.1 Tau neutrino production at SHiP

The main source of tau neutrinos is the decay of D_s mesons, produced in the SHiP proton target. The production mechanisms of these charmed mesons can be grouped in two main categories:

- leading fragmentation: $c \rightarrow D_s^+, \bar{c} \rightarrow D_s^-$;
- subleading fragmentation: $\bar{s} \rightarrow D_s^+, s \rightarrow D_s^-$;

Currently available sets of proton Parton Distribution Functions (PDF) [52] provide an asymmetric strange sea quark distribution in the proton ($s(x) \neq \bar{s}(x)$), resulting in a different number of produced D_s^+ and D_s^- for the subleading contribution.

Direct tau neutrinos are produced from the D_s meson decay channels $D_s^+ \rightarrow \tau^+ \nu_\tau$ and $D_s^- \rightarrow \tau^- \bar{\nu}_\tau$, with a well known branching ratio $BR(D_s^\pm \rightarrow \tau^\pm \nu_\tau) = 0.0548 \pm 0.0023$ [53].

Another ν_τ is produced by the following tau lepton decay, leading to a total of two tau neutrinos from each D_s meson decay. The lepton number conservation ensures that the total amount of produced antineutrinos corresponds to the amount of neutrinos. However, the mass of the τ lepton (1.777 GeV) is very similar to the mass of the D_s meson (1.968 GeV). Therefore, the direct neutrino brings only a small fraction of energy and momentum of the mother D_s in its 2-body decay, and it is thus less energetic than the second tau neutrino.

3.1.1 Heavy flavour cascade production

The SHiP experiment is characterized by a long beam dump target, covering about twelve interaction lengths. Due to this large depth, charmed hadrons can be produced either directly from the initial pN collision (primary production), or from a subsequent interaction of secondary particles (cascade production).

The generation of charmed hadrons has been simulated according to the algorithm designed by Dijkstra and Ruf [54]. First, the ratios $\chi = \frac{\sigma_{cc}}{\sigma_{total}}$ for $p, n, \pi^\pm, K^\pm, K_S$ and K_L are computed, as a function of their momenta, then normalized to

$$\chi_{norm} = \frac{\chi}{\chi(400 \text{ GeV}/c \pi^+ n)}. \quad (3.1)$$

Starting from the initial 400 GeV protons, either a standard Pythia [55] event with all QCD processes active or a charm event is produced, with the probability of the latter being the obtained χ_{norm} . If a charm event is not generated, all the protons, neutrons, pions and kaons from the interaction with momenta above the kinematic cutoff are added to the list of suitable charm mothers. Then, the previous step is repeated, until this list is cleared.

Charmed hadrons produced in pN interactions directly from the 400 GeV SPS proton beam are referred to as "primary production". On the other side, "cascade production" is referred to as an associated charm production happened after any previous interaction of the proton beam, either elastic or inelastic. Including the cascade contribution the simulations predict about 2.3 times more charmed hadrons. However, the energy loss during the cascade produces softer charmed hadrons, as it can be seen in the momentum distributions of charmed hadrons reported in Figure 3.1. Consequently, the neutrino spectrum is modified as well, and neutrinos from cascade production have lower energy, as shown in Figure 3.2 for tau neutrinos.

3.1.2 Expected neutrino yields

The produced tau neutrino spectrum is shown in Figure 3.3, with the clear presence of two peaks at different momenta. They correspond to direct neutrinos and neutrinos from tau decays, having different energies. This spectrum is the input for the propagation of neutrinos to the SND detector, which is placed at a distance of ~ 40 m from the proton target.

At SHiP energies, the dominant process is the Charged Current Deep Inelastic Scattering (CCDIS). For SHiP predictions, neutrino cross sections provided by the GENIE [56] toolkit are used as input. The same procedure is applied to electron and muon neutrinos. Table 3.1 shows the number of neutrinos produced and interacting within the SND target from 2×10^{20}

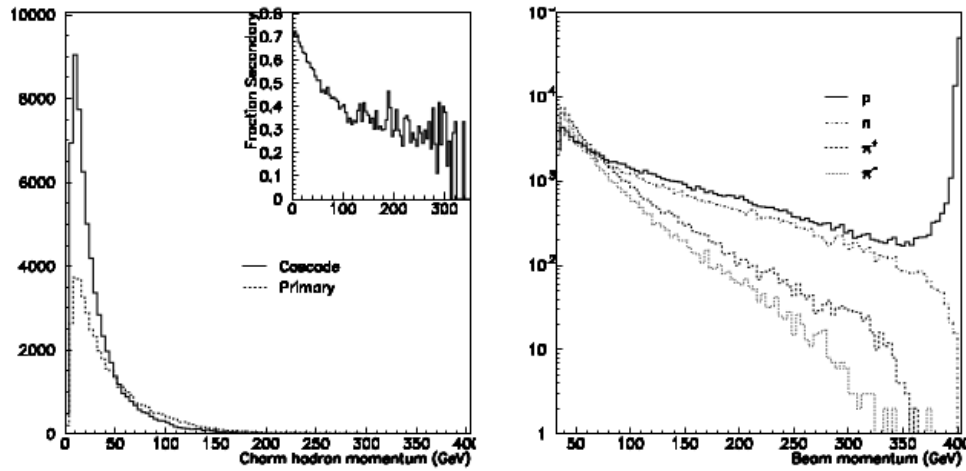


Figure 3.1: On the left, momentum of charmed hadrons, separating the direct production from 400 GeV protons and the cascade production. The latter fraction is reported in the top-right inset. On the right, momentum of mother particles [54].

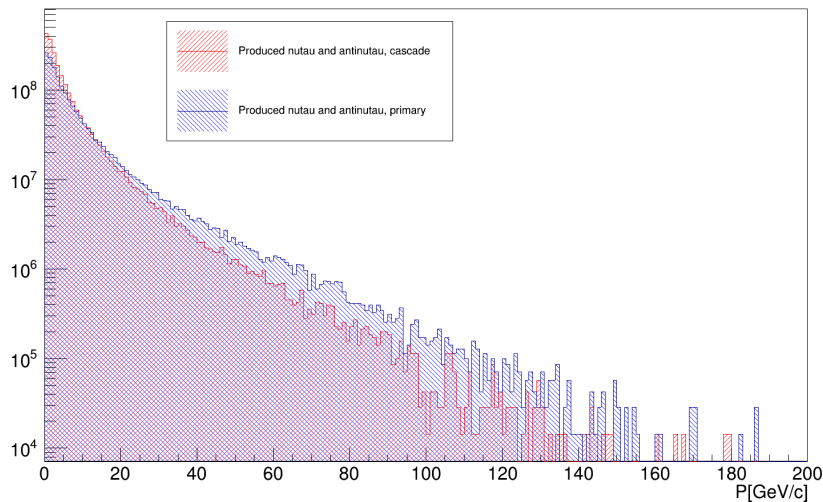
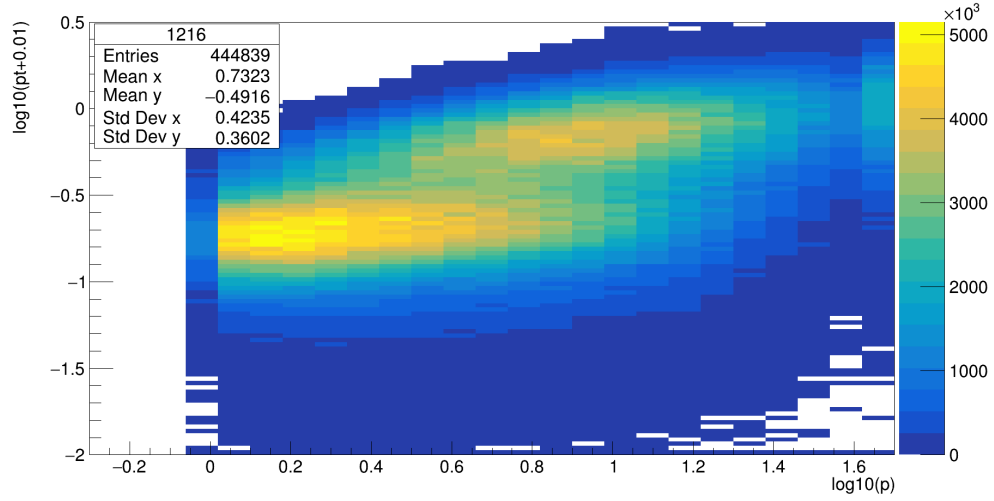


Figure 3.2: Momentum of produced tau neutrinos and antineutrinos, separating primary contribution (in blue) and cascade contribution (in red). The histograms are weighted to a spill of 5×10^{13} protons on target.

Figure 3.3: Spectrum of ν_τ transverse momentum vs momentum.

N	Beam dump	CCDIS interactions
N_{ν_e}	2.8×10^{17}	1.1×10^6
N_{ν_μ}	4.2×10^{18}	2.7×10^6
N_{ν_τ}	1.4×10^{16}	3.2×10^4
$N_{\bar{\nu}_e}$	2.3×10^{17}	2.6×10^5
$N_{\bar{\nu}_\mu}$	2.7×10^{18}	6.0×10^5
$N_{\bar{\nu}_\tau}$	1.4×10^{16}	2.1×10^4

Table 3.1: Expected neutrino flux for different neutrino flavours after collecting 2×10^{20} protons on target [39].

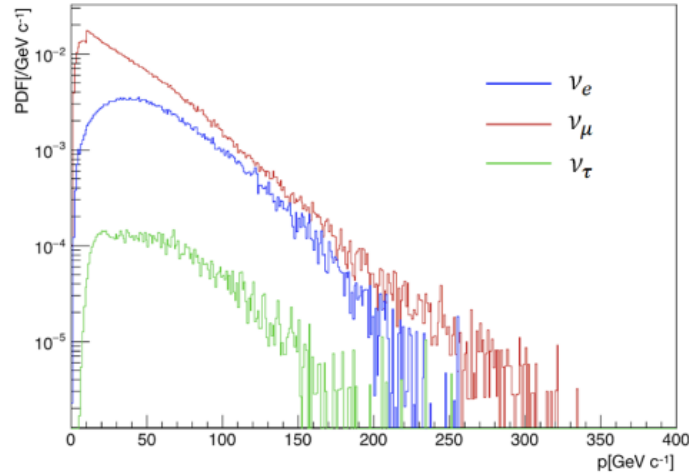


Figure 3.4: Momenta spectra of all neutrino flavours, underdoing a DIS interaction in the emulsion target [38].

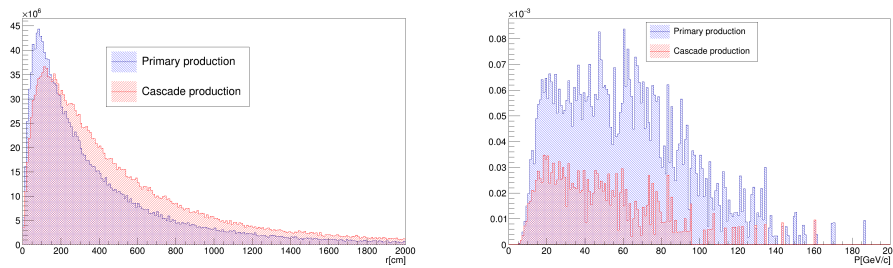


Figure 3.5: Comparison between tau neutrinos from primary production (in blue) and cascade production (in red). On the left, the position of tau neutrinos in the transverse radius, with respect to the beam direction. On the right, the momentum of CCDIS interacting neutrinos.

protons on target (p.o.t), as expected to be collected in the 5 years of data taking [39].

Neutrinos from cascade production are characterized by a wider beam profile, with a larger fraction escaping the detector acceptance. Moreover, since the CCDIS interaction cross section increases with the energy and neutrinos from cascade production are softer, there is a lower number of neutrino interactions. Figure 3.5 shows the radial position of neutrinos after the propagation to the neutrino target position (on the left) and the spectrum of interacting neutrinos (on the right). Overall, the total tau CCDIS neutrino yield including both primary and cascade productions is 1.3 times larger than the yield from primary production only.

3.2 Neutrino detection in the SND

Starting from the rate of interactions and the cross section σ , the luminosity of a particle detector is defined as $L = R/\sigma$. It depends on the intensity of incoming particles I and on the detector structure (its density ρ and its length l), according to the following formula:

$$L = I \rho l N_A, \quad (3.2)$$

where N_A is the Avogadro number.

In the simulation, neutrino p and p_T momenta are generated from the 2D spectrum stored from the proton simulation. The ϕ angle, instead, is uniformly generated between 0 and 2π .

Neutrino interaction vertices are produced uniformly along the z coordinate. On the other side, x and y positions are computed by projecting the neutrino from the SHiP proton target to the interaction point. The final step of the generation is to account for the material composition along the neutrino path in the SND, by computing the relative interaction probability as a density ratio ρ/ρ_{max} , finally used to sample the accepted vertex positions. The interactions are more frequent in higher density materials: Figure 3.6 shows the position distribution of neutrino interaction vertices in the zy plane, from a simulation of 100k events in the SND whole region. There is the SND target, surrounded by the iron and coil of the magnet. Downstream, the interactions are mostly in the iron blocks of the muon filter.

Each neutrino interaction is weighted according to the total material density encountered during the simulation step:

$$W = \sum_i \rho_i l_i, \quad (3.3)$$

where the sum goes over the different materials encountered, each one with density ρ_i and length l_i . Therefore, the weight W allows to compute the number of equivalent incoming neutrinos for each simulated event, by inverting Equation 3.2.

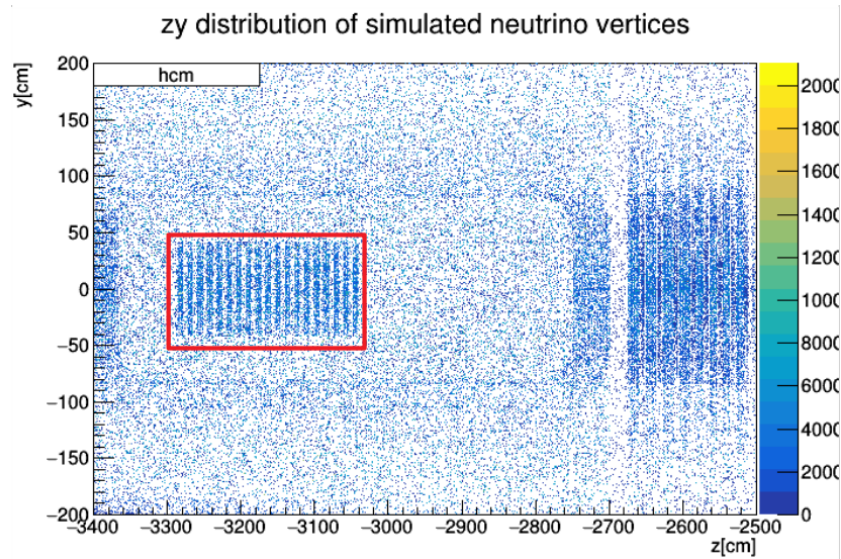


Figure 3.6: Distribution of simulated neutrino interaction vertices, in the SND area. The emulsion target, dedicated to the reconstruction of neutrino interactions, is marked in red. The range of the y axis matches the height of the SND magnet.

3.2.1 SND layout

The technical structure of each subdetector has been presented in section 2.2. Here, a quick overview of the detector is reported, describing the physics task of each component. There are two main sections: the 720 cm magnet, which contains the emulsion target and spectrometer planes, and a 180 cm muon filter.

The magnetized target is dedicated to the localization and reconstruction of the neutrino interaction vertices. Its design has been subjected to an optimization in the last years, following two main requirements:

- Maximising the acceptance to the incoming neutrino flux;
- Reducing background interactions by residual muons, coming from the SHiP target.

The number of neutrino interactions and the position of muons are shown in Figure 3.7. The spatial region free from muons defines an hourglass shape in the transverse plane, which was applied to the design of the magnet. On the other side, the neutrino flux shows a significant decrease with the radius, making it more convenient to extend the overall size of the detector longitudinally.

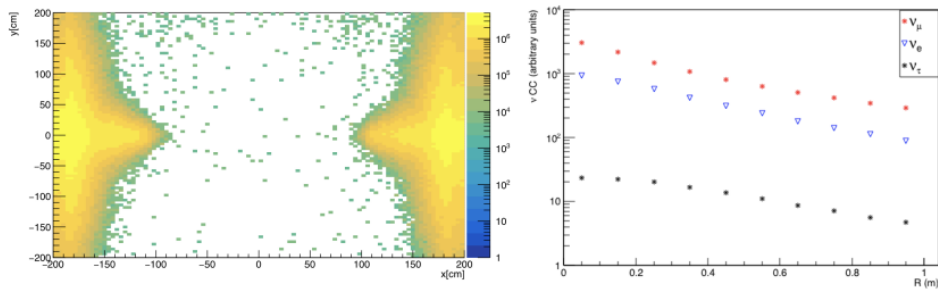


Figure 3.7: Distributions that have driven the SND design. On the right: the signal from neutrinos, on the left, the muon background [39].

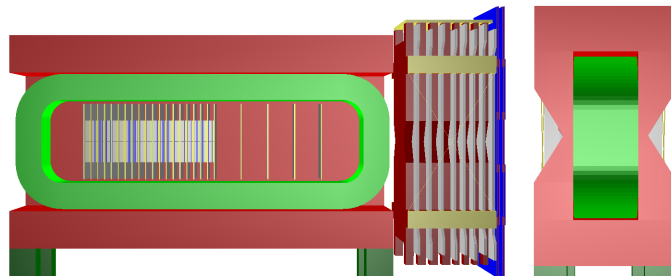


Figure 3.8: Layout of the Scattering Neutrino Detector. On the left, the lateral view. On the right, the front view.

The downstream section has the task of detecting muons produced in neutrino interactions and tagging background muons, providing data for the downstream SHiP Hidden Sector detectors. The upstream 8 RPC stations, interleaved with iron slabs, address the first function, while the two downstream MRPC stations, without any passive material in between, are designed for the latter.

The lateral and front views of SND are shown in Figure 3.8, as they have been implemented in the geometry of the simulation, using the ROOT TGeo interface.

3.2.2 Lepton identification

SND has the task of detecting charged current interactions of all neutrino flavours. The discrimination between different neutrinos is achieved through a clear identification of the associated charged lepton. The three possible topologies are shown in Figure 3.9:

- Electron neutrino interactions are identified through the detection of the electromagnetic showers produced by the associated electrons.

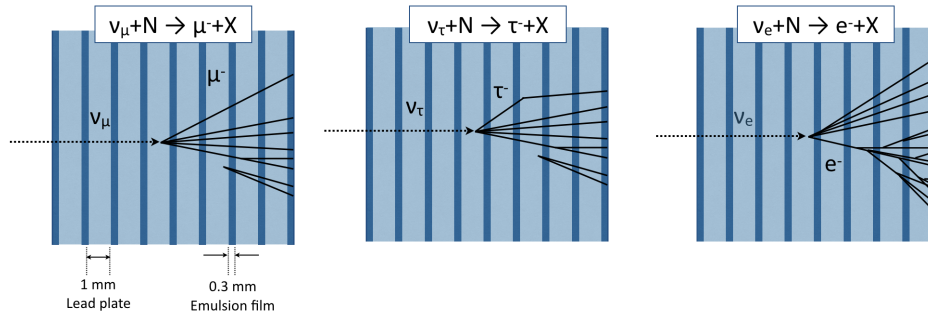


Figure 3.9: Schematics of CCDIS neutrino interactions in the Emulsion Cloud Chamber: muon neutrino (left), tau neutrino (middle) and electron neutrino (right).

All the tracks originated in a shower are directed towards the source electron, so they can be followed backwards up to the production point. The electron energy can be measured by exploiting the relationship between the number of tracks belonging to the reconstructed shower and the electron energy. A shower reconstruction algorithm dedicated to high track densities is currently being developed. In chapter 4, its application to the data from an electron test beam are discussed;

- Muon neutrino interactions produce high penetrating particles, which are identified by the RPC stations in the muon filter downstream of the spectrometer. The first requirement is to enter the first RPC plane, but the muons need to be also separated from charged hadrons. The selection of the muon candidates has been optimized by analyzing simulations of muon neutrino interactions. The resulted requirement is the presence of at least four particle clusters, which are defined with a radius of 2 cm, according to the spatial resolution of the RPCs. The found efficiency is $\epsilon = (56.0 \pm 0.4)\%$ [57];
- The short mean life of the tau lepton leads to a second decay vertex near the tau neutrino interaction. The high spatial resolution of the emulsions allows to separate the two vertices, thus identifying the neutrino interactions. The details of the tau decay search are provided in the following sections.

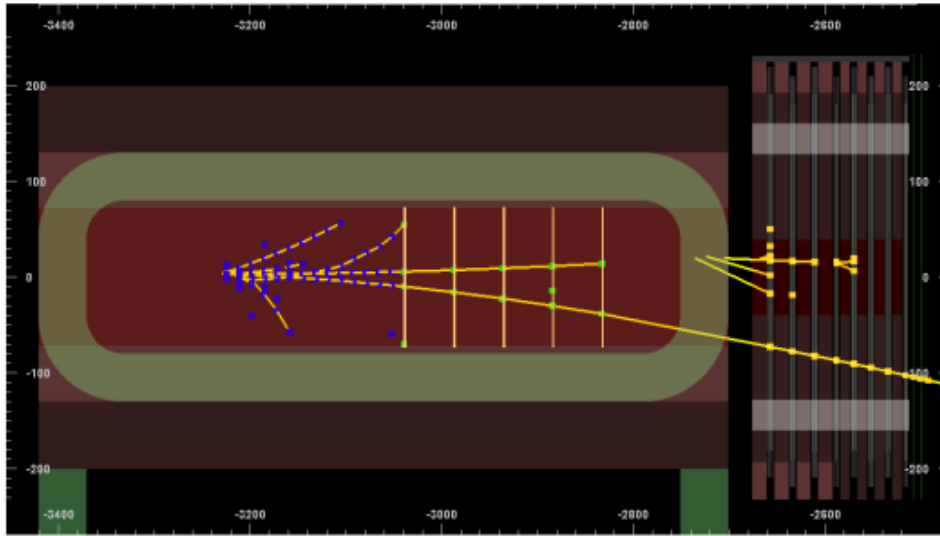


Figure 3.10: Display of a simulated muon neutrino event in the SND [57].

3.2.3 Tau neutrino interaction within the ECC target

The SND target is designed by implementing the Emulsion Cloud Chamber (ECC) technique, and it is composed of 76 bricks. Each brick covers a transverse surface of $40 \times 40 \text{ cm}^2$ and it is made of 56 1 mm-thick lead passive layers, interleaved by 57 nuclear emulsion films. It overall acts as a standalone detector, where the tracks of charged particles are reconstructed in its whole volume. The possibility of tungsten as a passive material with higher density is currently under study, to increase the number of radiation lengths covered by the target.

A display of a simulated CCDIS tau neutrino interaction within the detector is shown in Figure 3.11. While the process is simulated with GENIE [58], particle propagation and detection are performed by Geant4 [59].

The first step is the location of the neutrino interaction vertex. A conservative fiducial volume is considered, by excluding the regions at a distance of less than 1 mm from the transverse edges of the brick. Also, the presence of at least 4 emulsion films from the vertex to the downstream end of the target is required.

In the fiducial volume, a vertex is considered visible if there is at least one track with momentum above $1 \text{ GeV}/c$ and slope $\tan\theta < 1$. Since the tau lepton decays shortly after its production, this track alone cannot be considered enough for a good location of the primary neutrino vertex.

The tau lepton can decay in the following visible final states:

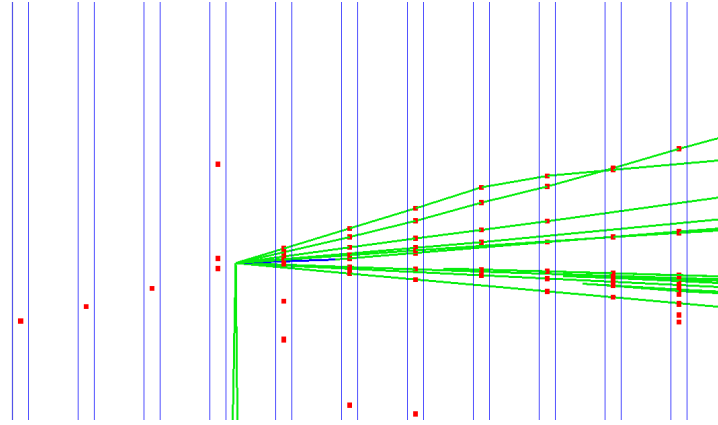


Figure 3.11: Display of a simulated tau neutrino interaction in an Emulsion Cloud Chamber of the SND. The tau lepton is drawn in blue.

Decay Channel	Branching Ratio
$\tau^- \rightarrow e^- \nu_\tau \bar{\nu}_e$	17.8%
$\tau^- \rightarrow \mu^- \nu_\tau \bar{\nu}_\mu$	17.4%
$\tau^- \rightarrow h^- \nu_\tau (n\pi^0)$	49.6%
$\tau^- \rightarrow h^- h^+ h^- \nu_\tau (n\pi^0)$	15.2%

Table 3.2: Branching ratios for τ decay channels [53].

- one single electron, from the $\tau^- \rightarrow e^- \nu_\tau \bar{\nu}_e$ decay;
- one single muon, from the $\tau^- \rightarrow \mu^- \nu_\tau \bar{\nu}_\mu$ decay;
- one charged hadron, from the $\tau^- \rightarrow h^- \nu_\tau (n\pi^0)$ decay channels;
- three charged hadrons, from the $\tau^- \rightarrow h^- h^+ h^- \nu_\tau (n\pi^0)$ decay channels.

The reconstruction of the decay vertex requires the presence of at least one track with momentum above 100 MeV/c, slope $\tan\theta < 1$ and Impact Parameter (IP) larger than 10 μm , with respect to the production vertex. In addition, the kink angle between the tau and the daughter track must be at least 20 mrad. Finally, the maximum decay length allowed is 4 mm, in order to reject background from hadronic re-interactions.

The overall efficiencies are reported in Table 3.3, as estimated from a simulation of tau neutrino and antineutrino interactions in the emulsion target, for a total of 53923 events.

Efficiency	$\tau \rightarrow 1e$	$\tau \rightarrow 1\mu$	$\tau \rightarrow 1h$	$\tau \rightarrow 3h$
Fiducial volume	$(92.8 \pm 0.1)\%$			
Visible interaction	$(75.8 \pm 0.2)\%$			
Decay search	$(46.4 \pm 0.5)\%$	$(46.1 \pm 0.5)\%$	$(45.5 \pm 0.3)\%$	$(57.0 \pm 0.6)\%$

Table 3.3: Topological requirements for a tau decay event detected in an emulsion target. Decay search efficiency is reported for each decay channel separately.

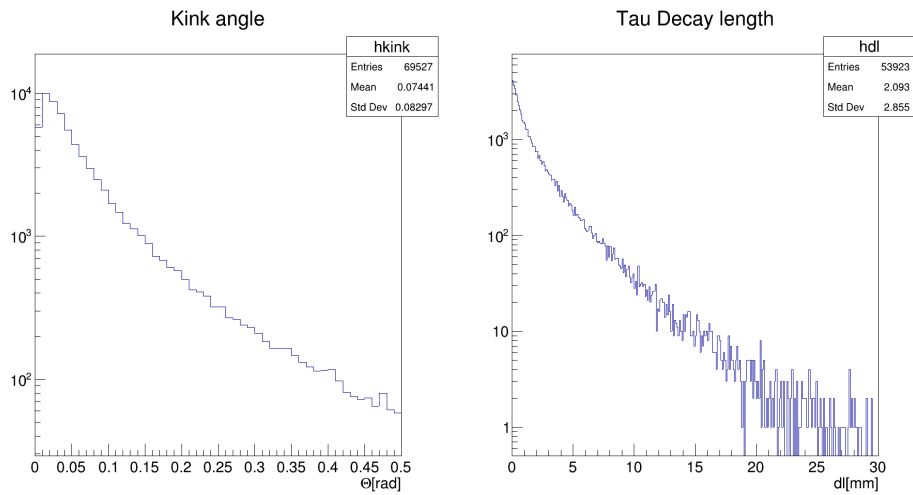


Figure 3.12: Features of tau lepton decay: on the left, the kink angle. On the right, the flight length.

3.2.4 Momentum and charge measurement of tau daughters

Full reconstruction of the tau neutrino interaction requires to collect data about the kinematics of the tau decay.

Charge and momentum of muons and hadrons can be measured from the curvature detected in the magnetic spectrometer. When the charge of all tau decay daughters is identified, lepton number conservation can be applied to distinguish tau neutrinos from the anti-neutrinos.

SND spectrometer

A particle with unit charge, traveling through a region with an homogeneous magnetic field B , is deflected into a circular path in the transverse plane to the field direction, with radius

$$R[m] = \frac{p_T}{eB} = 3.3 \frac{p_T[GeV/c]}{B[T]}, \quad (3.4)$$

where e is the electron charge and p_T is the orthogonal component of the momentum, with respect to the magnetic field. Since along the field direction the particle is not deflected, the overall three-dimensional trajectory is an helix.

This equation is the basis for all magnetic spectrometers. Particles with higher momentum are subjected to a minor deflection by the magnetic field, therefore the momentum resolution decreases with energy. Therefore, at high energies magnets with large magnetic fields and field lengths are required, in order to achieve the desired resolution. Moreover, the magnet should provide the field as uniform as possible in the spectrometer region, to avoid complications in the track reconstruction.

If the detectors can be operated in a magnetic field, a widespread method is to measure the sagitta of the particle trajectory $s = R(1 - \cos(\theta/2))$. In this case, the relative momentum resolution can be estimated as

$$\sigma_p/p = \sigma_s/s = \frac{8p}{0.3BL^2} \sigma_s. \quad (3.5)$$

For the magnetic spectrometer of the SND detector, detailed field maps have been provided from the Engineering Department of our University, according to the design of the magnet reported in Ref [47]. They have been then implemented in the simulation, and provided as input for the Geant4 simulation. They can be seen in Figure 3.13. In our reference system, the

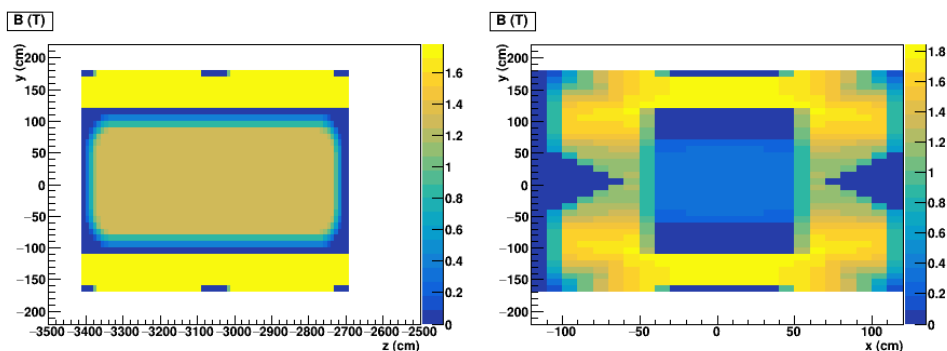


Figure 3.13: Implementation of the magnetic field maps in the simulation. On the left, the lateral view (zy plane), on the right, the front view (xy plane).

magnetic field in the area of the SND target is directed along the x axis.

The sagitta values obtained from the simulation are reported in Figure 3.14, for negative and positive decay daughters. The y component is from the magnetic deflection, while the not deflected x component provides an estimation of the resolution σ_s .

The efficiency has been estimated from Monte Carlo simulation, by applying a Gaussian smearing on the hit positions with resolution $1.5 \mu\text{m}$ for CES stations and $100 \mu\text{m}$ for DT stations. A clear charge identification requires a value at least three times larger than the resolution. This requirement of charge identification leads to an efficiency of $(35.2 \pm 0.5)\%$ for the muon decay channel and of $(11.0 \pm 0.2)\%$ for the single hadron decay channel.

3.2.5 Tau lepton decay channels

Electrons and muons from the tau lepton decays can be identified with a similar procedure as the leptons directly associated to charged electron and muon interactions, described in section 3.2.2.

Particle identification and measurement of the electron energy is done by reconstructing the electromagnetic shower, using the Emulsion Cloud Chamber as a calorimeter. The energy of the electrons produced by tau decay in the SND is shown in Figure 3.15, along with the number of the plate where the electron is produced. When the electron starts near the end of the brick, largest part of the shower develops in the following chambers. Shower reconstruction is then performed from the data of the Target

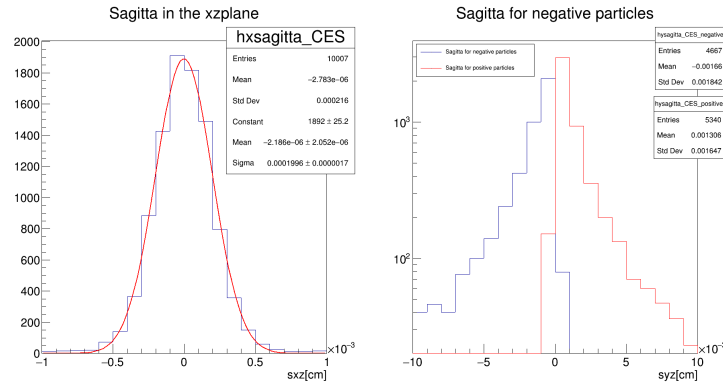


Figure 3.14: Sagitta distributions for tau decay daughters, from CES detectors. On the left, sagitta in the xz plane, without magnetic bending. On the right, sagitta in the zy plane, with magnetic bending, separating positive (in red) and negative (in blue) particles.

Tracker planes, which need to be combined with emulsion data in a global reconstruction framework.

On the other side, the first requirement for muon identification is the geometrical acceptance of the first RPC plane. Figure 3.16 shows the spectrum of all muons produced from the tau lepton decays, and the component which enters the first plane.

The identification of the muons from the hadron background is performed with the same algorithm used for charged muon neutrino interactions. In the RPC stations of the muon filter at least four isolated particle clusters are required. The clusters are defined with a radius of 2 cm and they are centered in the muon hit positions. The application of the muon selection to the tau neutrino simulation (within the muon decay channel) results in a detection efficiency of $(27.6 \pm 0.5)\%$.

3.3 Background from neutrino-induced charm events

As discussed in section 1.4.5, the detection of neutrino-induced charm production events is one of the physics goals of the SHiP experiment, since it allows to investigate the structure of the nucleon. However, since charmed hadrons have lifetimes similar to the tau lepton and present analogous decay topologies, they act also as background for the tau neutrino search. Therefore, an essential step in designing the detector is the separation between charmed events and tau neutrino events.

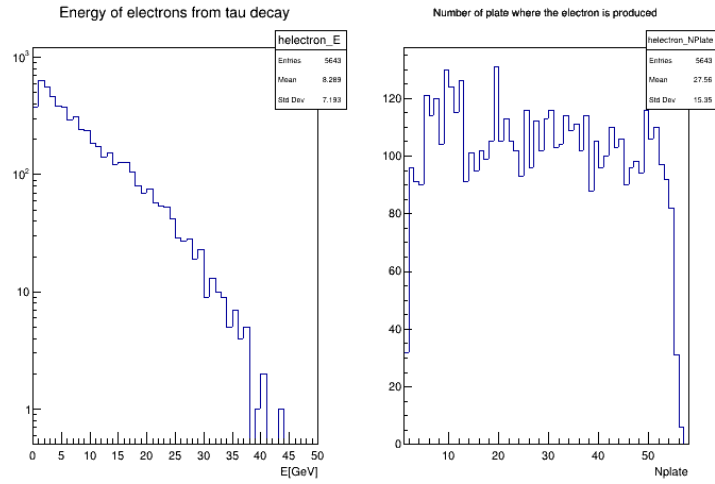


Figure 3.15: Electrons produced by tau decay, from a tau neutrino interaction. On the left, their energy spectrum. On the right, the plate number where they have been produced.

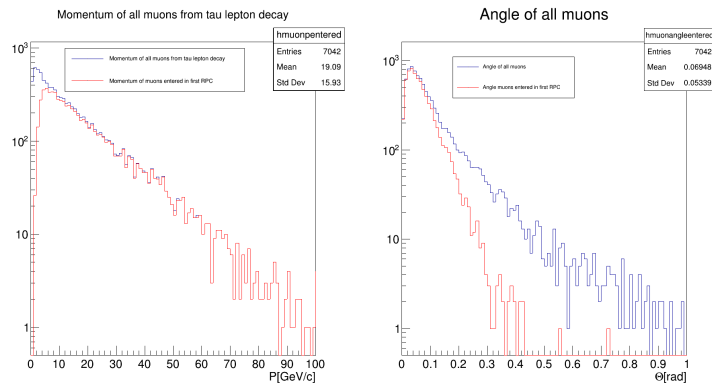


Figure 3.16: Momentum and angle of muons from tau decay. The red component is the one which enters the first RPC plane.

Selection	Charm background efficiency
Geometrical	$(93.0 \pm 0.1)\%$
Primary Vertex Location	$(92.0 \pm 0.1)\%$
Decay Search	$(74.4 \pm 0.2)\%$
Charge identification	$(33.7 \pm 0.2)\%$
Primary muon not identified	$(10.6 \pm 0.2)\%$

Table 3.4: Breakdown of efficiencies for the background induced by charmed hadron production in ν_μ CC interactions. Decay search requirements are the same applied for tau lepton identification. The requirement of the primary muon to be not identified is applied for the event to be classified as background.

Charmed hadrons are produced with a rate of a few percent in charged current muon and electron neutrino interactions. They are a background source for tau neutrino interactions if the charged lepton at the primary vertex is not detected. High efficiency in the primary lepton detection is therefore needed to reduce this relevant background source. A simulation of 39391 charged current muon neutrino events with charm production has been studied, to evaluate the muon detection efficiency, by applying the same procedure followed for the tau neutrino events. The resulting efficiencies are reported in Table 3.4. The muon identification reduces the background to $(10.6 \pm 0.2)\%$, which are the events with a similar topology of the tau decay.

Neutrino	CCDIS with charm production	Estimated background events
N_{ν_μ}	1.3×10^5	1.4×10^4
$N_{\bar{\nu}_\mu}$	2.5×10^4	2.6×10^3
Total	1.5×10^5	1.6×10^4

Table 3.5: Expected CCDIS muon neutrino interactions with charm production for 2×10^{20} protons on target [39] and expected number of observed events, after all the selections.

The estimated amount of expected charm production events induced from CCDIS muon neutrino interactions is reported in Table 3.5. The total number of expected background events after five years of data taking is 1.6×10^4 . Assuming a detection efficiency of 28% for all tau neutrino events, 1.5×10^4 signal events can be predicted from the yields in Table 3.1. The signal/noise ratio needs thus to be improved with additional information.

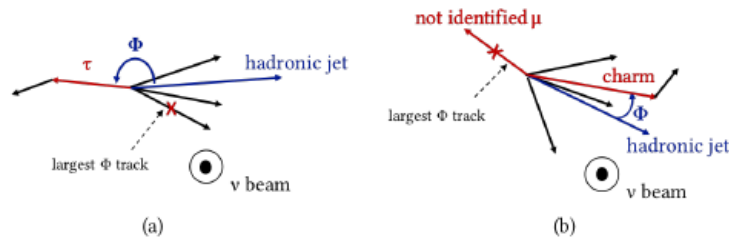


Figure 3.17: Diagram explaining the difference between tau neutrino interaction (a) and charm background events (b).

If the primary lepton is not identified, charm background can be separated from tau neutrinos by exploiting different kinematic features between the two categories. In a neutrino interaction, the primary lepton and the hadronic jet are expected to be back-to-back in the transverse plane. Therefore, the tau lepton is expected to have a large phi angle ϕ with respect to hadronic tracks at the neutrino vertex, as shown in Figure 3.17. The OPERA experiment demonstrated that the application of a cut-based analysis following this kinematic feature allows a further background reduction of a factor 3 [60].

The distribution at SHiP energy regime is reported in Figure 3.18, both for signal and background. Adding the requirement $\phi \geq \phi_{min} = 2.2$ rad to the selection results in a expected number of 7.4×10^3 detected tau neutrinos, with respect to 4.8×10^3 events of charmed hadrons induced by muon neutrino interactions. The signal/noise is thus improved, becoming ~ 1.5 .

3.4 Current status of SND design

The plan of the SHiP Collaboration in the near future is to build prototypes of the SHiP components and to adapt them to compact setups. These additional experiments should not only provide technical tuning, but also new physics data.

The conceptual idea of the Scattering and Neutrino Detector, in particular, will be employed in a new neutrino detector at the LHC, at 480 m from ATLAS collision point. The design is adapted to the limited space available and described in the recent Technical Proposal [24].

In general, the next steps will involve the design of updated reconstruction algorithms, to cope with the larger area of the emulsion tar-

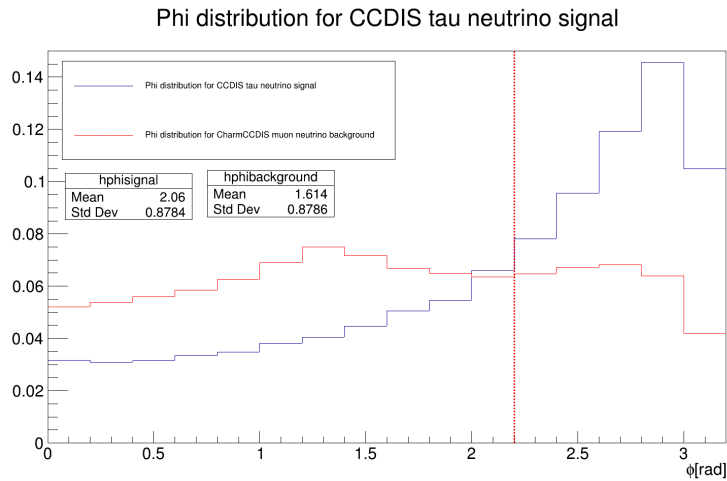


Figure 3.18: Distribution of phi angle between the tau lepton (in blue) or charmed hadron (in red) with respect to the hadrons produced in the neutrino interaction. The red line shows the minimum angle $\phi_{min} = 2.2$ rad required.

get ($40 \times 40 \text{ cm}^2$, with respect to the standard OPERA brick $12 \times 10 \text{ cm}^2$). The performance of tungsten as passive material will be compared with lead, evaluating both the advantages and the challenges of this more dense medium in the ECC.

Chapter 4

Electromagnetic shower reconstruction

Nuclear emulsion films interleaved with layers of passive material act as a high-resolution and effective tracker unit for most of high-energy particles, following them while they traverse the Emulsion Cloud Chamber. Electrons, however, interact almost immediately with the medium, leading to wide electromagnetic showers made of a large number of electron-positron pairs. A dedicated reconstruction procedure needs to be applied to this situation, with the aims of separating overlapping showers, identifying the electrons originating them and measuring their energies.

Electron identification provides a wide range of physics applications, according to the aim of the considered experiment. Concerning the area of interest of the SHiP experiment, the main processes to be studied are:

- Charged current electron neutrino interactions, with the shower coming directly from the associated lepton;
- Charged current tau neutrino interactions, where the tau lepton decays into an electron. The electromagnetic shower starts from the lepton produced in the decay vertex;
- Light dark matter scattering off electron, producing an isolated electromagnetic shower;

After a brief overview of the physics of electromagnetic showers, the algorithms used for shower reconstruction in an ECC are described, along with their application in a dedicated test beam, performed at DESY laboratories in 2019.

4.1 Energy loss and shower development

When a particle traverses matter, it generally loses part of its energy by interacting with it. The most common process is ionization, but at high energies the latter is dominated by bremsstrahlung, which consists in the emission of photons. The parameter commonly used to compare the contribution of these two processes is the critical energy ϵ_c , which represents the value where the average energy loss per ionization equals the radiation loss¹. The energy loss per radiation depends on the incoming particle and the material, according to the following formula [61]:

$$\frac{-dE}{dx} = 4\alpha N_A \left(\frac{e^2}{mc^2} \right)^2 \ln \left(\frac{183}{Z^{\frac{1}{3}}} \right) \frac{z(z+1)}{A} Q^2 E, \quad (4.1)$$

where α is the fine structure constant, N_A the Avogadro number, m and Q are the mass and charge of incoming particle, while A and Z are mass and atomic number of the material. The average energy loss from radiation decreases for heavier particles. The critical energy ϵ_c of a particle of mass m increases with respect of the electron of mass m_e , with the ratio $(m/m_e)^2$. If for electron and positrons already at 100 MeV the main source of energy loss is bremsstrahlung, for the next lightest charged particle, the muon, the critical energy becomes more than 40000 times larger. Therefore, even if radiative process can happen for all charged particles, they are dominant only for electrons and positrons.

The quantum of electromagnetic field, the photon (γ), mainly loses energy in three processes: the photoelectric effect, most likely to occur at low energies, the Compton scattering, happening mostly in an intermediate energy range, and the pair-production, which dominates at high energies and leads to an electron-positron pair in the final state. Figure 4.1 shows the contribution of different processes to the total photon cross section, as function of the energy. In addition, photons are also subject at low energies at the Rayleigh coherent scattering, where the photon is deflected without losing energy.

Starting from the bremsstrahlung of a single high energy electron, the radiated photon produces a pair, which then emits new photons. The result is an electromagnetic shower, increasing the number of particles exponen-

¹Various textbooks and the Particle Data Group prefer another definition, requiring the ionization loss per radiation length (X_0) to be equal to the electron energy. Please check Ref.[53] for more details.

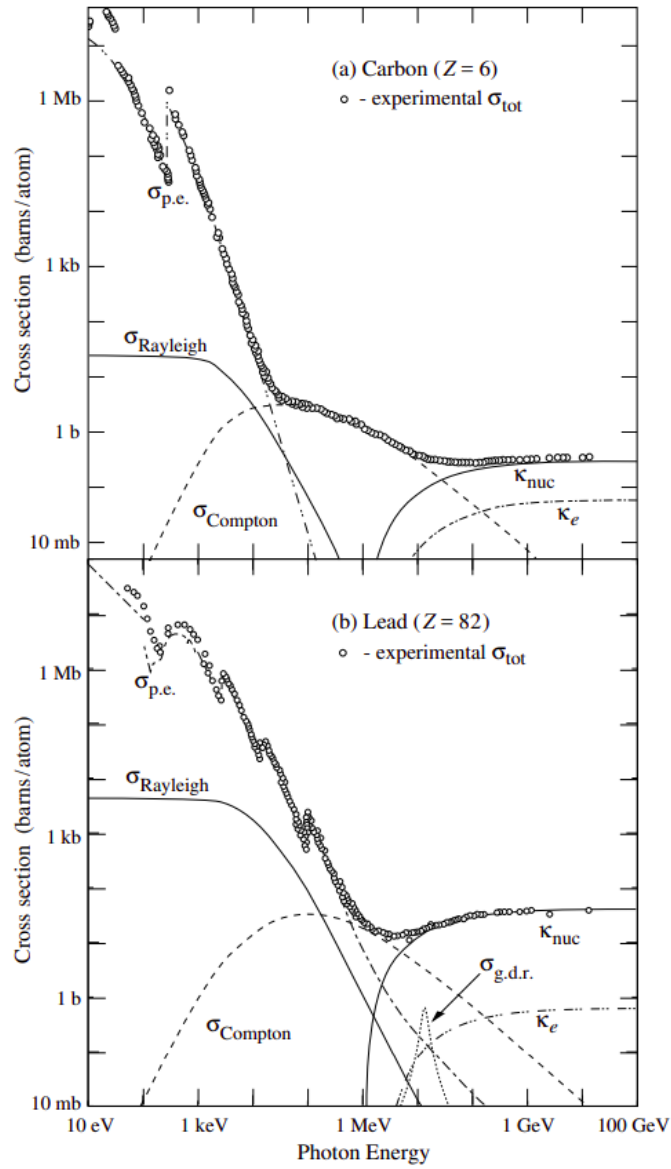


Figure 4.1: Photon total cross section in carbon and lead as function of the energy. The contributions of different processes are shown [53].

tially until their energy decreases to the critical energy, and the cascade gradually stops.

For electrons the energy loss formula can be simplified in

$$-\frac{dE}{dx} = \frac{1}{X_0}E, \quad (4.2)$$

where X_0 is called the radiation length of the material. It is defined as the required thickness to reduce the mean energy of an electron by a factor e . When the distances are measured in units of X_0 , material-dependent effects are significantly reduced.

One of the most important requirements of a detector is the containment of the shower to an adequate level, since escaping particles are a source of fluctuations, affecting the accuracy of the energy measurement. The longitudinal distance covered by the shower increases with its energy. The absorber thickness needed to contain longitudinally 95% of the shower energy ranges from $\sim 11X_0$ at the energy of 1 GeV to $\sim 22X_0$ at the energy of 1 TeV.

On the other side, the spread of the shower in the transverse plane is dominated by two processes: multiple scattering of the electrons away from the shower axis and relatively long mean-free path of the photons. A parameter commonly used to describe the transverse development is the Molière radius

$$R_M = \frac{21 \text{ MeV}}{E_c} X_0. \quad (4.3)$$

About 90% of the shower is contained in one R_M [61]. This value is almost completely independent on the particle energy, which instead affects the longitudinal development of the shower.

4.2 Electron beam exposure at DESY

4.2.1 Motivation

An electromagnetic calorimeter has the purpose of detecting electromagnetic showers and measuring their energies. Sampling the target by interleaving layers of passive material with sensitive layers (usually scintillators) is a common procedure, which reduces the cost of a massive detector, at the expense of a slightly worse energy resolution.

Emulsion Cloud Chambers act as sampling calorimeters with higher spatial resolution than scintillators, and the absence of electronics makes them easy to handle and to assemble in a compact detector. On the other side, since nuclear emulsions do not provide time information, they cannot be used as trigger, a role usually performed by electromagnetic calorimeters in large experiments.

The capability of ECCs to clearly reconstruct electromagnetic showers has been already successfully employed by the OPERA experiment. However, SHiP target will be characterized by a high beam intensity, leading to high track densities in the emulsion target. All the framework of the electromagnetic shower reconstruction needs to be then designed for this environment.

A test beam has been performed in DESY at the end of October 2019, to apply new reconstruction algorithms to real data from an electron beam. Other than emulsion detectors, Scintillating Fibres (SciFi) stations have been employed in a SHiP-like configuration, in order to test the connection between the ECC target and the downstream Target Tracker and to evaluate the complementarity of the two detectors in the electromagnetic energy estimation.

4.2.2 Experimental apparatus

The beam has been provided by DESY II synchrotron [62], which can accelerate electrons and positrons up to an energy of 7 GeV. Electrons having energy of 2, 4 or 6 GeV (depending on the exposure run) were selected by a dipole magnet, then collimated to be directed towards the experimental area. Here, the electron beam impinged in a ECC target, followed by a set of SciFi trackers.

Both the ECC chamber and the SciFi trackers were placed on a moving table, which allowed the beam to scan uniformly the whole active surface of the detector, in the transverse (xy) plane (Figure 4.2).

Emulsion Cloud Chamber

Nuclear emulsion films used in this exposure have a transverse size of (125×99) mm². 9 ECC bricks have been prepared, with different thickness of passive material: from 14 mm to 56 mm (Figure 4.3). Reconstruction can thus be analyzed in different conditions of shower containment in the



Figure 4.2: Picture of the detector installed in the moving table, in preparation for the test beam.

chamber. The passive material used in the ECC target is lead for all the chambers, except one, referred to as “RUN7”. In the latter, tungsten has been employed as passive material, in order to study data quality and to compare the electromagnetic showers with the ones reconstructed in lead bricks.

A total of 8 exposure runs has been performed, as reported in Table 4.1. In RUN8, two ECC bricks have been exposed, with RUN8B replacing a passive lead layer between the SciFi trackers, to study shower reconstruction in multiple ECC bricks.

Scintillating Fibre Tracker

The SciFi detector (Figure 4.4) is made of 6 planes, covering a transverse surface of $(130 \times 130) \text{ mm}^2$. Each plane consists of two layers for measurements in the X and Y directions, leading to a total of 12 trackers.

The SciFi tracker is made of plastic scintillating fibres with a diameter of $250 \mu\text{m}$. The core of each fibre is clad with two scintillators: the primary one de-excites quasi instantaneously, emitting UV photons. The light is then propagated to the second scintillator, which absorbs the primary photon and fluoresces at blue wavelengths, acting as a wavelength shifter. Finally, the light is transported and received by a multichannel array of silicon photomultipliers, which convert it into electric signal.

Each single SciFi plane provides a time resolution better than 500 ps,

Configuration	Energy	ECC Passive Plates	N emulsion films
RUN1	6 GeV	56×1 mm Pb	57
RUN2	6 GeV	42×1 mm Pb	43
RUN3	6 GeV	28×1 mm Pb	29
RUN4	6 GeV	14×1 mm Pb	15
RUN5	2 GeV	28×1 mm Pb	29
RUN6	4 GeV	28×1 mm Pb	29
RUN7	6 GeV	18×0.9 mm W	19
RUN8A	6 GeV	14×1 mm Pb	15
RUN8B	6 GeV	28×1 mm Pb	29
TOTAL	-	238 mm Pb 18 mm W	265 $\sim 3.3 \text{ m}^2$

Table 4.1: Summary of exposures at DESY19. The two ECC targets in RUN8 have been exposed to the same electron beam.

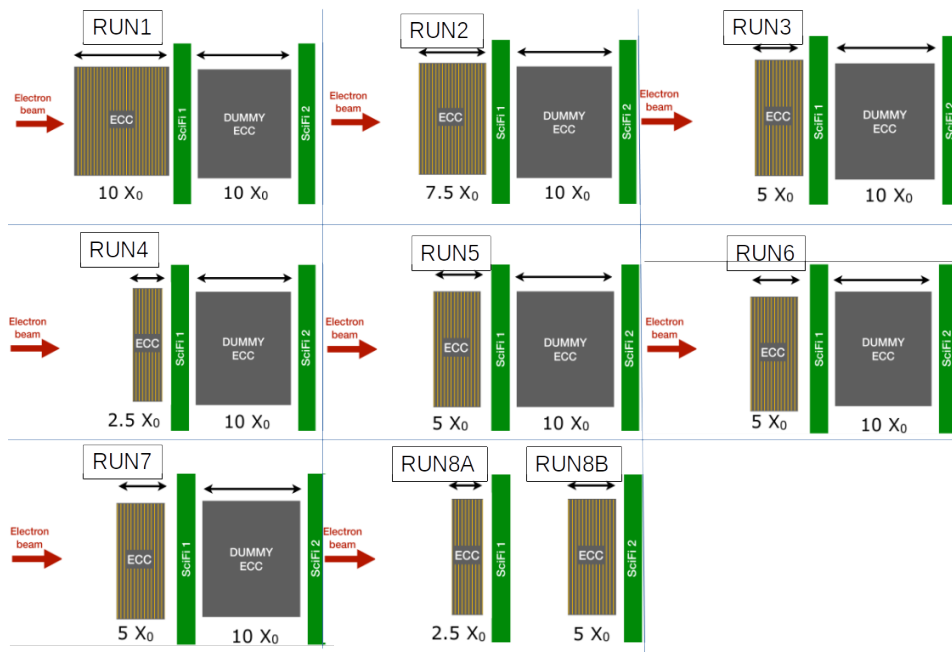


Figure 4.3: Drawing of run configurations during DESY test beam.

allowing to acquire at a trigger rate of 50 kHz for single track and better than 1 kHz for shower readout.

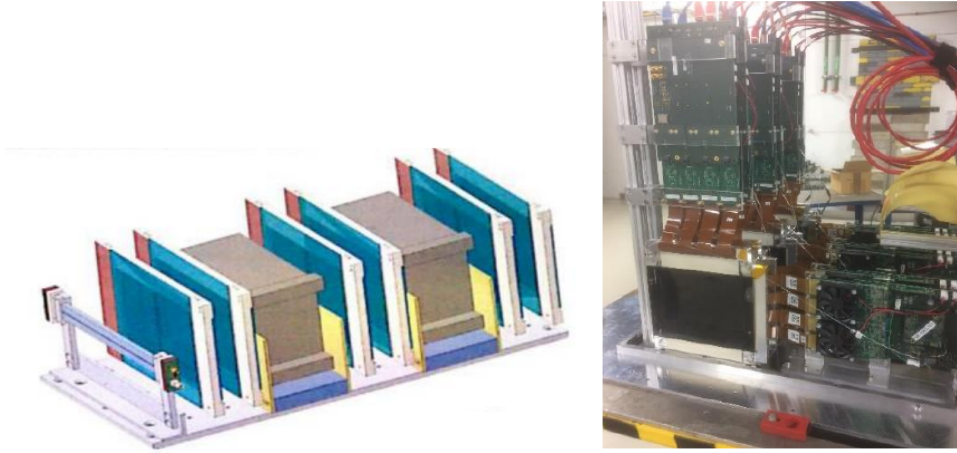


Figure 4.4: Geometry and picture of the SciFi trackers configuration [63].

4.2.3 Emulsion data reconstruction

Emulsion films have been produced by Slavich company. After the exposure, they have been developed in the emulsion facility in Naples, where they have been prepared for data analysis.

Emulsions films are then scanned with automated optical microscopes in Naples and Zurich laboratories, by employing an improved version of the European Scanning System microscope [64], used in the OPERA experiment. The emulsion scanning system takes place on a mechanical stage,

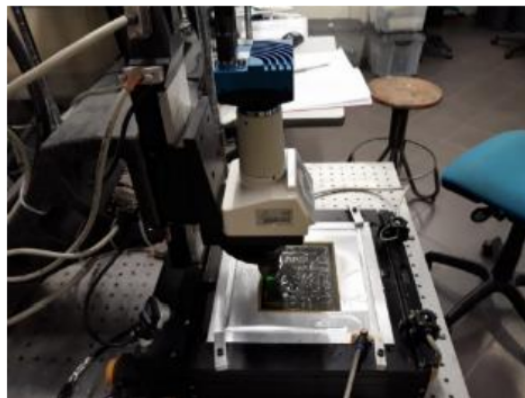


Figure 4.5: An optical microscope used for the scanning of nuclear emulsion films.

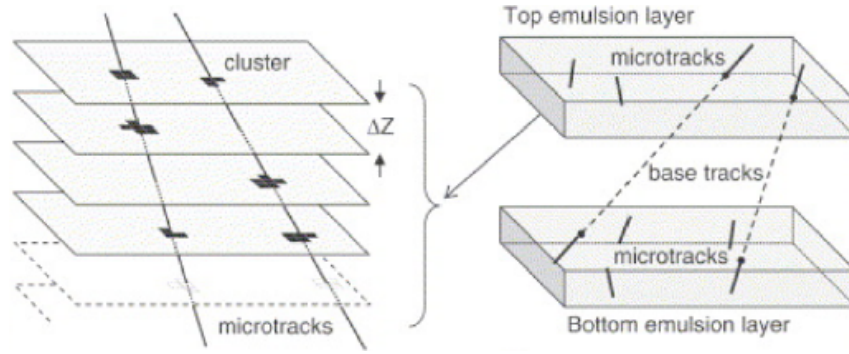


Figure 4.6: Reconstruction of scanned emulsion information. On the left, reconstruction of micro-tracks from digitized clusters. On the right, reconstruction of base-tracks from two matched micro-tracks.

movable along both x and y axes. The microscope is moved along z with a vertical resolution of a few microns, covering the entire emulsion thickness. The three-dimensional structure of the track is reconstructed from topographic images collected by a CMOS Mega-Pixel camera, converting the emulsion grains into digital pixels. The system has been upgraded by the emulsion group in Naples: the current version implements the new scanning software LASSO [65] and a faster camera. It can reach a scanning speed of $190 \text{ cm}^2/\text{h}$, ten times larger than before [66]. A picture of a microscope is shown in Figure 4.5.

Immediately after the scanning, the acquired images are digitized and an image processor recognizes aligned clusters, i.e. groups of pixels of determined size and shape. Clusters belonging to different levels are connected separately for both emulsion layers, resulting in two *micro-tracks*. Linking the matching micro-tracks from the closest points to the plastic base provides the particle trajectory in the emulsion film, stored in the *base-track*. The reconstruction process is shown in Figure 4.6.

The angles of a base-track are usually represented as the components in the zx and zy planes, called T_x and T_y . The angular agreement between the base-track and the two source micro-tracks is expressed by the following χ^2 ,

$$\chi^2 = \frac{1}{4} \left[\left(\frac{T_{tra}^{top} - T_{tra}}{\sigma_{tra}} \right)^2 + \left(\frac{T_{lon}^{top} - T_{long}}{\sigma_{long}} \right)^2 + \left(\frac{T_{tra}^{bot} - T_{tra}}{\sigma_{tra}} \right)^2 + \left(\frac{T_{lon}^{bot} - T_{long}}{\sigma_{long}} \right)^2 \right], \quad (4.4)$$

where the angles of the two microtracks $T^{top,bot}$ are compared with the

angles of the base-track T . To isolate asymmetries along ϕ , the reference system is rotated by an angle $\delta = -\phi$, to the plane (T_{long}, T_{tra}) :

$$\begin{bmatrix} T_{long} \\ T_{tra} \end{bmatrix} = \begin{bmatrix} \cos(\delta) & \sin(-\delta) \\ \sin(\delta) & \cos(\delta) \end{bmatrix} \begin{bmatrix} T_x \\ T_y \end{bmatrix}. \quad (4.5)$$

The angular resolution σ_{tra} has a constant value of 13 mrad, while the longitudinal resolution σ_{lon} worsens with the angle of the base-track:

$$\sigma_{lon} = (1 + 5 \tan\theta)\sigma_{tra}. \quad (4.6)$$

Low momentum particles are subjected to higher scattering and are then reconstructed with a worse χ^2 .

Angles and positions of the base-track are initially in the local reference system of the single plate, centered in the middle of the plastic base. In order to connect the data of several consecutive films, a global system needs to be defined. A set of affine transformations is computed, correcting relative misalignments between the plates:

$$x'_i = A_{ij}x_j + B_i, \quad (4.7)$$

where x_i and x_j are the track position coordinates in the two plates. The affine transformations A_{ij} and B_i are determined from the data of cosmic rays and other penetrating particles.

4.3 Shower reconstruction algorithms

4.3.1 Introduction

The geometry of the detectors employed during the DESY test beam has been implemented in the FairShip Monte Carlo framework, for all runs. Electron propagation and interactions in the apparatus are simulated through Geant4 software [59]. For each run, 360 electrons are fired at the start of the ECC target, uniformly in the transverse plane. The amount of simulated electrons represents the total beam expected to be exposed in each ECC during the test beam.

The distribution of simulated showers in the transverse plane is shown in Figure 4.7. Since the lead thickness between two consecutive emulsion films amounts to about $0.18 X_0$, on average showers start after the fifth

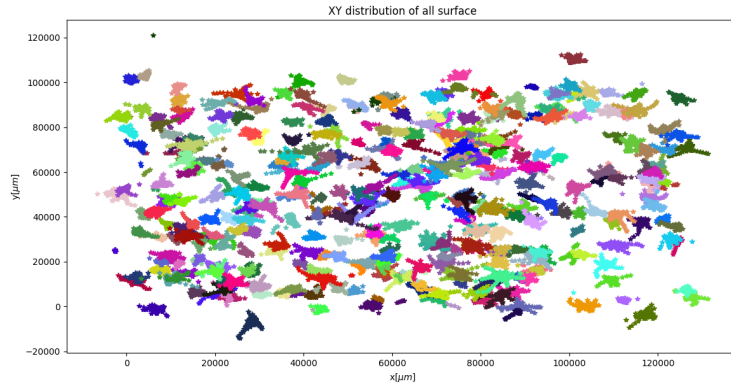


Figure 4.7: Position distribution of all showers in a run, in the frontal view (xy plane).

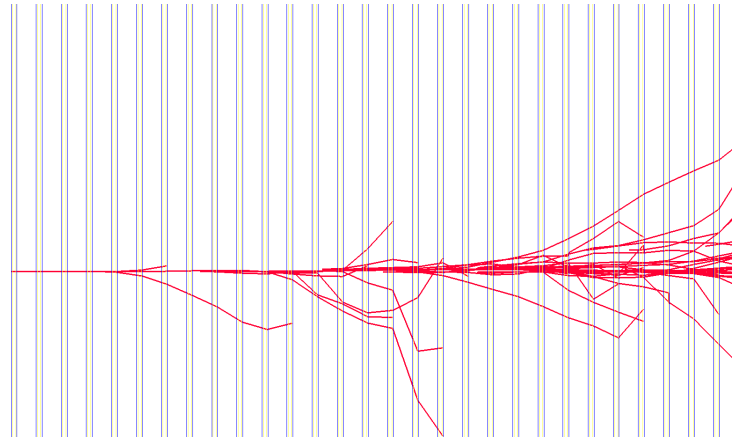


Figure 4.8: Display of a simulated shower in the Emulsion Cloud Chamber.

plate.

After the simulation, hits stored in the emulsion layers are saved if they satisfy the following visibility cuts:

$$P > 30 \text{ MeV}/c, \theta < 1 \text{ rad.}$$

The lower momentum threshold is required to accurately track a real particle traversing the emulsion plate, while the upper angular threshold correspond to the maximum angle acquired during the scanning of the emulsions in this detector configuration. The display of a 6 GeV shower in the ECC calorimeter after this selection is shown in Figure 4.8.

4.3.2 Background

Since the energy response is linearly dependent on the number of base-tracks reconstructed in the shower, background rejection is critical to achieve a good energy resolution. In the analyzed data sets, there are two main background sources:

- Instrumental background, defined as uncorrelated grains deposited in the nuclear emulsion films.
- Physical background, defined as all the particles which have been exposed after the assembling of the brick, but they are not related to the electromagnetic shower events. They are characterized by correlation between consecutive plates, which makes them more difficult to separate from overlapping showers.

At the beginning of the shower, the slope of signal segments is expected to be similar to the direction of the electron beam, which is perpendicular to the emulsion surface. On the other side, cosmic rays accumulated before the assembly of the brick are mostly parallel to the surface, due to the flipped position of the films during the transport. Figure 4.9 shows the distribution of the θ angle with respect to the beam direction, for both signal and background tracks in the first ten emulsion films. This angular difference can be used in locating the beginning of the shower. However, it becomes less significant in downstream films, due to the development of the shower. Improving the background rejection requires to take into account angular and position correlations between segments from the same shower. Two different solutions will be presented in the next sections.

4.3.3 Standard reconstruction procedure

The standard algorithm for electromagnetic shower reconstruction in the ECC has been developed for the OPERA experiment [67]. The process is shown in Figure 4.10. From a single base-track, a cone of a given opening angle α is defined, collecting the hits within it. Additionally, the hits must also be in a cylinder of radius ΔR_{max} . Starting from the initial base-track, each other collected segment is connected to the shower, if the angular displacement $\delta\theta$ and position displacement δr with respect to one track already added to the shower are below 0.15 rad and 150 μm , respectively.

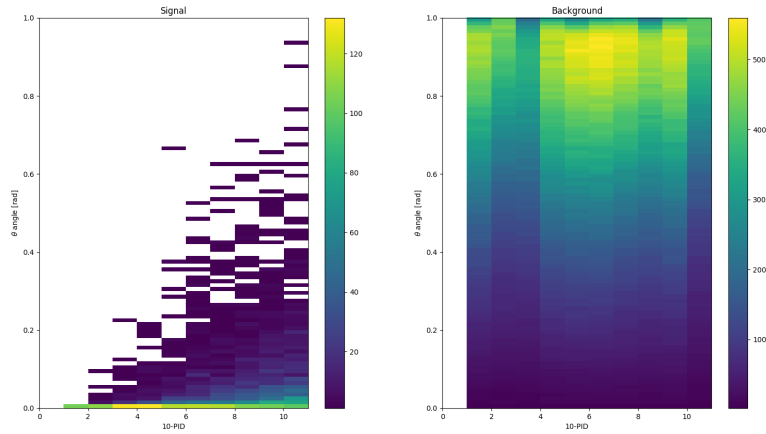


Figure 4.9: Distribution of the slope of the shower tracks, with respect to emulsion film number. On the left the signal distribution, on the right the background distribution. Film number 1 is the most upstream in the ECC target.

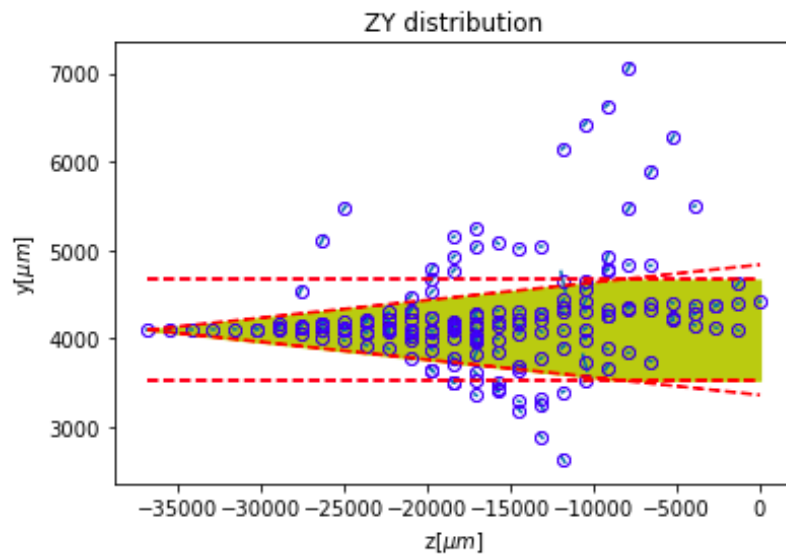


Figure 4.10: 2D representation of electromagnetic shower hit search. The base tracks in the yellow region area are collected, and they are accepted if the position and angular displacements are satisfied.

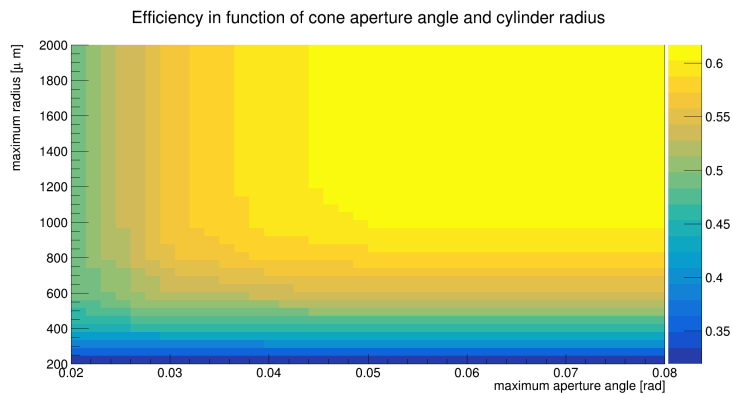


Figure 4.11: Shower reconstruction efficiency as a function of the cone aperture angle and cylinder radius.

The total efficiency of the shower reconstruction algorithm, including the requirements on $\delta\theta$ and δr , is reported in Figure 4.11, as a function of the cone angle and the cylinder radius. Building a cone with angle $\alpha = 0.04$ rad and requiring a maximum radius $\Delta R_{max} = 1000 \mu\text{m}$ leads to an efficiency of $(59.2 \pm 0.2)\%$.

This reconstruction requires the position and angle of the first track of the shower, in order to be able to construct the search cone. Moreover, this algorithm is unable to separate near showers, since the hits are assigned to the wrong cone. New algorithms based on machine learning have been tested to solve these problems.

Application to data from DESY test beam

In the data from DESY test beam, all the initial electrons enter the ECC brick from the most upstream plate, at very small angles. The selection of volume tracks starting from the first three plates of the brick, with a conservative angular requirement $\tan\theta < 0.05$, provides the starting points of the electromagnetic showers produced in the brick (Figure 4.12).

The results of the application of the standard reconstruction algorithm on data from DESY RUN7 are shown in Figure 4.13. Two populations can be recognized: a descending distribution, due to random combinations of segments, and a second distribution, corresponding to the expected signal from electromagnetic showers. The signal contribution can be selected by requiring at least 50 associated segments in the reconstructed shower.

The development of the reconstructed showers in the ECC brick can be

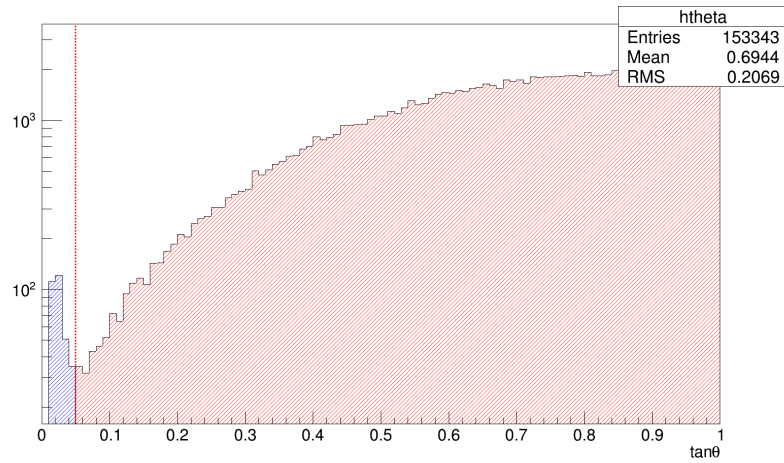


Figure 4.12: Angular spectrum of tracks starting from first three emulsion films. Tracks selected as possible shower injectors are shown in blue, below the red line at $\tan\theta < 0.05$.

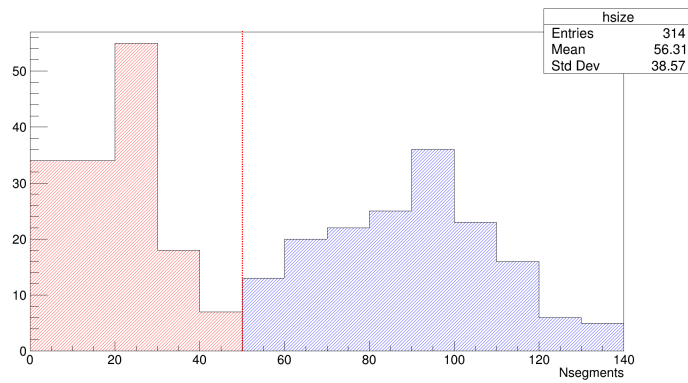


Figure 4.13: Number of segments associated to each reconstructed shower. The red line shows the applied selection $N_{segments} \geq 50$.

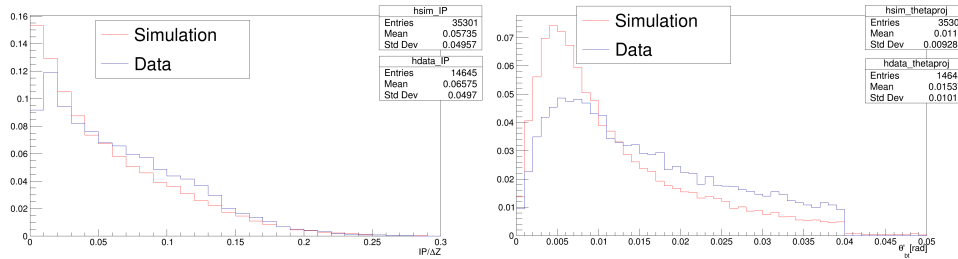


Figure 4.14: Comparison between reconstructed showers from Monte Carlo simulations (in red) and from real data (in blue). On the left, the impact parameter over the longitudinal distance $IP/\Delta Z$. On the right, the angle with respect to the shower vertex θ'_{bt} .

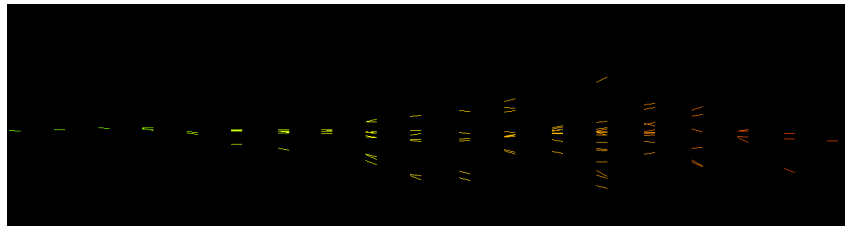


Figure 4.15: Display of a reconstructed shower in the zy plane from DESY RUN7 data.

studied with the following variables:

- θ'_{bt} : the angle that each base-track forms with the shower vertex;
- $IP/\Delta Z$: the impact parameter IP of each segment, with respect to the shower vertex, divided by the longitudinal distance ΔZ .

The distributions are shown in Figure 4.14, from a Monte Carlo sample of simulated showers (in red) and the reconstructed showers in the real data (in blue). A display of a shower is shown in Figure 4.15. It starts from a 6 GeV electron in a tungsten target and it develops in 106 base-tracks, traversing a total of 18 passive plates and 16.2 mm of passive thickness.

4.3.4 Machine Learning classification

The standard reconstruction procedure described in the previous section has been widely used in the past for its good performance and clear signature of the reconstructed shower events. However, it does not perform as well in higher background environments. Indeed, the cone becomes quickly highly contaminated with background base-tracks, needing more

stringent reconstruction parameters and the consequent loss of a large signal fraction.

To cope with the high intensity planned for future experiments, such as SHiP, new algorithms and procedures are being designed, often exploiting the performances of Machine Learning to find patterns and relations between the features of many data.

The feasibility of a Machine Learning algorithm for shower reconstruction in a ECC target has been already shown [68]. Positions and angles of the single base-tracks are not sufficient as features for a classifier, due to the large amount of background. Additional features can be computed as position differences between the track projection in the next emulsion film and near tracks. These features can be used to train the classifier to recognize the development of the shower in the ECC. The steps of this algorithm and its performances are described here.

Building the dataset

The spatial and angular position of each base-track in an emulsion film N_{plate} is represented by the four-dimensional vector $\vec{x} = (X, Y, T_X, T_Y)$. Each shower candidate is built starting from a single track, representing an electron at the start of the ECC target. The steps of the process are the following:

1. In the transverse plane, a square of $1 \text{ cm} \times 1 \text{ cm}$ area is constructed around the center of each shower. All segments within it are collected;
2. From the initial base-track, a pyramid with a square section is built to contain the shower development, as shown in Figure 4.16. The maximum (x, y) position of segments to be within it increases with plate number N_{plate} as

$$x(y) = p_1 \cdot (N_{plate} - N_0) + p_0, \quad (4.8)$$

where N_0 is the film where the shower starts. Parameters are set as $p_0 = 500 \mu\text{m}$ and $p_1 = 140 \mu\text{m}$.

3. Defining $\theta_{bt} - \theta_e$ as the difference between the angle of each base-track and the angle of the shower axis, a sharp cut $\theta_{bt} - \theta_e \leq 0.6 \text{ rad}$

is applied, to suppress a large fraction of noise, reducing the computational cost of the next step;

- Each shower base-track from emulsion film number N_{plate} is projected in the most downstream film $N_{plate} + 1$, leading to a new vector \vec{x}_{next} . Segments found in this film are accepted if the angular distance is less than $d\theta_{max} = 0.4$ rad. They are added to the dataset, storing both their absolute positions \vec{x}_i and the distances from the projected track $\vec{x}_i - \vec{x}_{next}$.

The added segments are projected to the next downstream film, and the procedure is repeated until the last downstream film containing shower segments. The signal efficiency of all the reconstruction steps has been estimated to be $(83.70 \pm 0.02)\%$ [69]. In addition, the angle θ'_{bt} and the distance $IP/\Delta Z$ are computed for each base-track (Figure 4.17).

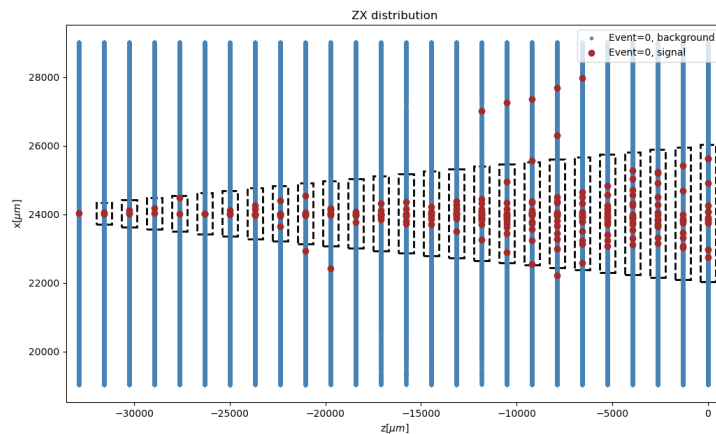


Figure 4.16: Display of the reconstruction of an electromagnetic shower in the ECC, showing the x coordinate of each base-track with respect to z . The dotted rectangles represent the research region for associated base-tracks in each film. Signal segments are marked in red, while background ones in blue [69].

Random Forest classifier

The dataset produced in the previous section needs to be provided to a classifier, in order to discriminate segments from electromagnetic showers and background. The employed model is the Random Forest [70] provided

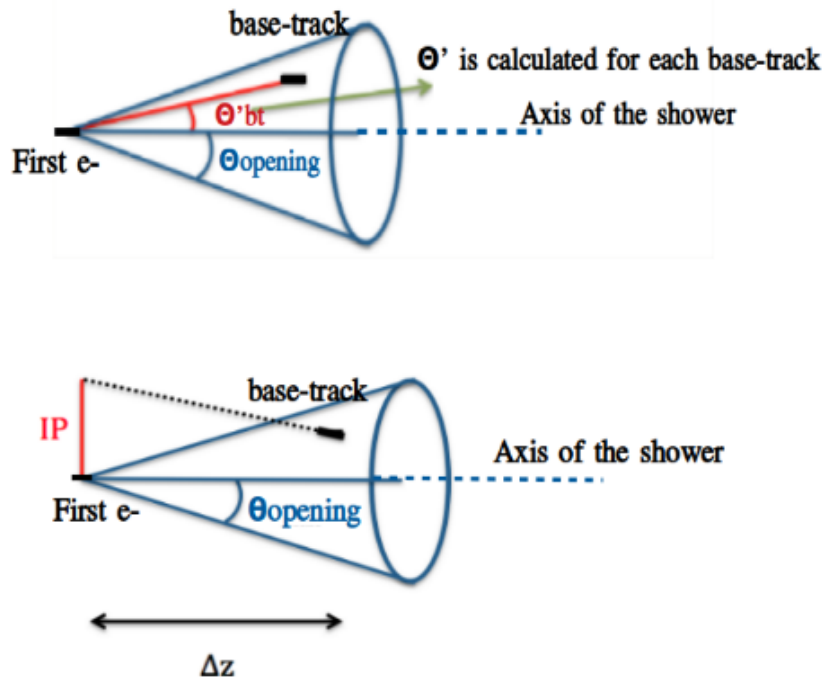


Figure 4.17: Drawing explaining two additional variables provided as input for discrimination between signal and noise segments in the Machine Learning classifier: the θ'_{bt} angle (above) and $IP/\Delta Z$ (below).

by scikit-learn [71]. The Random Forest can be defined as an ensemble of decision trees, combining “weak” learning systems to build a “strong” learning model. A decision tree is a sequence of binary selections, applied in a specific order on a given dataset. Each cut splits the sample in two nodes, which are followed through more selection until either signal or background largely dominates. A single tree allows for a straightforward interpretation, as it can be visualized by a simplified two-dimensional tree structure shown in Figure 4.18, but it is very unstable with respect to statistical fluctuations in the training sample.

In the Random Forest implementation, each tree is grown using only a random subset of all considered variables, and from a sample of the original dataset of training events. This reduces the variance of the resulting estimator, with respect to the single trees which are highly subject to overfitting.

The hyperparameters of the Random Forest model have been optimized with a grid search, evaluating the performances of the model for each combination of a list of possible hyperparameters. The final model employs 500 estimators and the maximum depth allowed for the trees is 200.

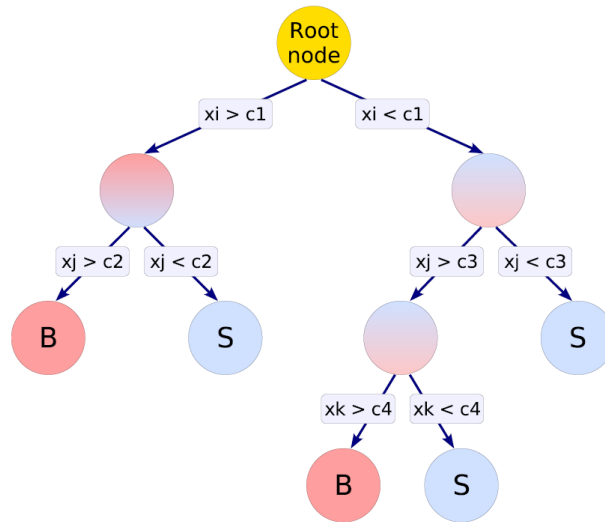


Figure 4.18: Schematic representation of a decision tree [72].

Application of Random Forest to data

The application of the Machine Learning classifier has been performed to the data from the RUN3 configuration. Starting positions of candidate showers are selected by requiring segments from the first three emulsion films, with $\tan\theta < 0.05$ and which have been associated to volume tracks.

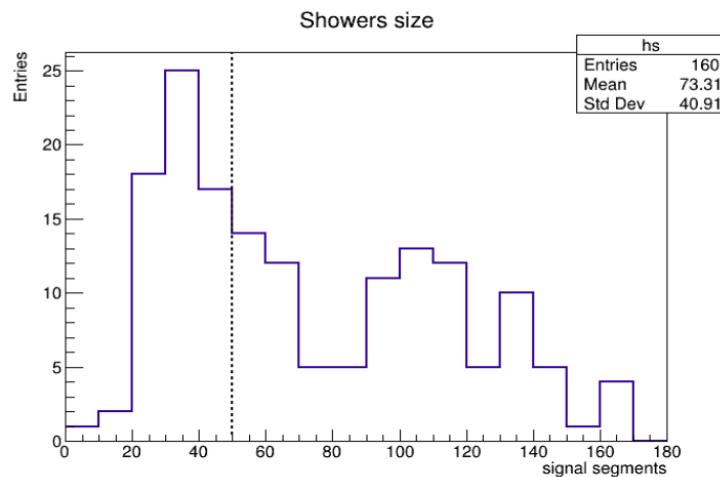


Figure 4.19: Size of reconstructed showers from RUN3 data. The dashed line shows the applied selection $N_{segments} \geq 50$.

A total of 160 showers has been reconstructed, their size is reported in Figure 4.19. Requiring a minimum number of 50 associated segments, 97 showers have been selected for topology studies. These showers have been

then compared with reconstructed electromagnetic showers from Monte Carlo simulation, according to the impact parameter $IP/\Delta Z$ and the cone angle θ'_{bt} . The compared distributions are shown in Figure 4.20. Segments from real data exhibit a larger spatial displacement from the shower vertex, effect assumed to be caused by misalignment between the emulsion films composing the bricks. This will be checked in future iterations of the optimization of the classifier, testing its stability to different misalignment conditions, after they are added to the simulation.

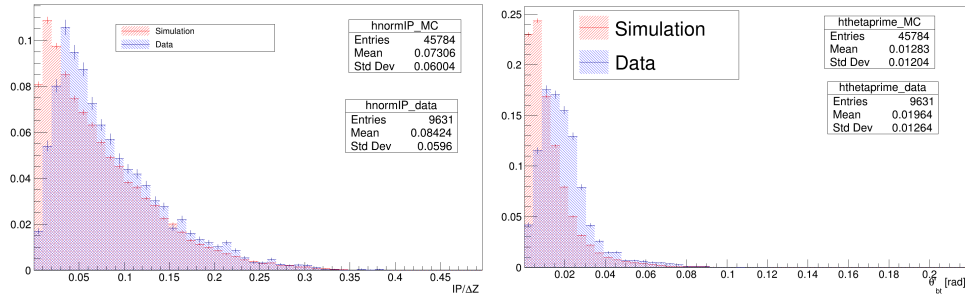


Figure 4.20: Showers provided by the Random Forest classifier from Monte Carlo simulations (in red) and from real data (in blue). On the left, the distance $IP/\Delta Z$. On the right, the angle θ'_{bt} .

Comparison with standard reconstruction

The performances of the classifier are evaluated according to the number of True Positive (TP) and False Negative (FN) segments from the true Monte Carlo signal, and to the number of True Negative (TN) and False Positive (FP) from the background. The following estimators are defined: the precision P

$$P = \frac{TP}{TP + FP} \quad (4.9)$$

and the recall R :

$$R = \frac{TP}{TP + FN} \quad (4.10)$$

The precision is defined by the ratio of real signal tracks in the classified sample, therefore describing the purity of the sample. On the other side, the recall is defined by the ratio of correctly recognized tracks over the total sample of signal tracks, representing the efficiency of the classification. A

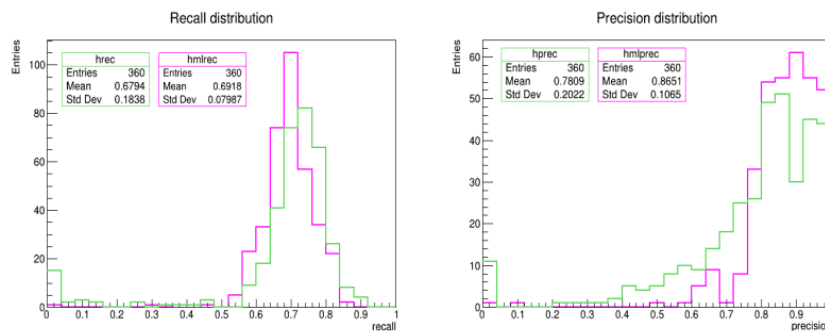


Figure 4.21: Comparison of performances between standard shower reconstruction (in green) and machine learning reconstruction (in purple) algorithms. On the left, recall distribution of electromagnetic shower reconstruction. On the right, precision distribution.

Classification	Mean Precision (\bar{P})	Mean Recall (\bar{R})
Standard	$(78.1 \pm 1.0)\%$	$(67.9 \pm 0.9)\%$
Random Forest	$(86.5 \pm 0.5)\%$	$(69.2 \pm 0.4)\%$

Table 4.2: Table of average performances of the two reconstruction algorithms in the overall sample.

comparison between the standard and Machine Learning electromagnetic shower reconstruction has been performed, providing as input the same dataset from a simulation of a DESY RUN3 exposure. The obtained performances for both algorithms are shown in Figure 4.21 for each shower, and Table 4.2 reports the average precision and recall.

4.3.5 Energy resolution

Once an electromagnetic shower is reconstructed, the energy can be measured from the number of associated segments. The reconstructed showers from ten Monte Carlo simulations of electrons at discrete energies between 1 GeV and 10 GeV have been provided as input. The resulting distribution is shown in Figure 4.22, where a linearity region between 50 and 210 segments can be identified. Above 210 segments the simulated energy range is not sufficient to correctly reproduce the linearity, and a larger fraction of the shower is not contained in the ECC brick of “RUN3” geometry (28 mm of lead). A linear fit $y = p_0 + p_1 \cdot x$ provides the following parameters:

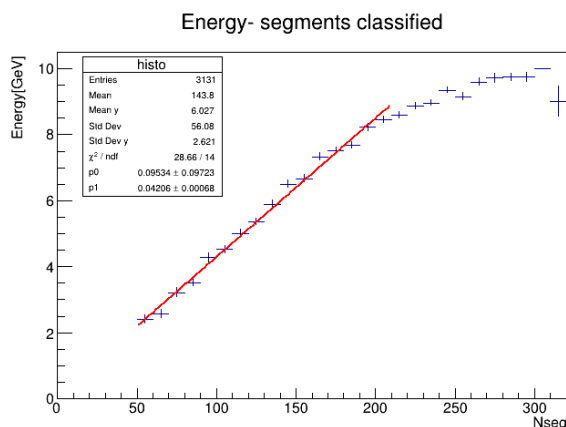


Figure 4.22: Calibration of shower energy measurement from the number of associated base-tracks [69].

$$\begin{aligned} p_0 &= (0.095 \pm 0.097) \text{ GeV} \\ p_1 &= (4.21 \pm 0.07) \times 10^{-2} \text{ GeV} \end{aligned} \quad (4.11)$$

The calibration function has then been used to determine the reconstructed energy E_{rec} from a separate sample of ten Monte Carlo simulations, with the same energies. The resolution for each energy is estimated as the σ of the Gaussian fit applied to the distribution

$$\Delta E / E = \frac{E_{true} - E_{rec}}{E_{rec}}. \quad (4.12)$$

The resolution dependence on the shower energy in a sampling electromagnetic calorimeter is usually parameterized as

$$\frac{\sigma_E}{E} = \sqrt{\left(\frac{a}{\sqrt{E}}\right)^2 + \left(\frac{b}{E}\right)^2 + c^2}, \quad (4.13)$$

where a is a “sampling term”, related to the statistical fluctuations of the number of times a high electron shower is sampled, b is an energy independent contribution from electronic noise, c includes material and detector effects [73]. The fit is shown in Figure 4.23 and the results are:

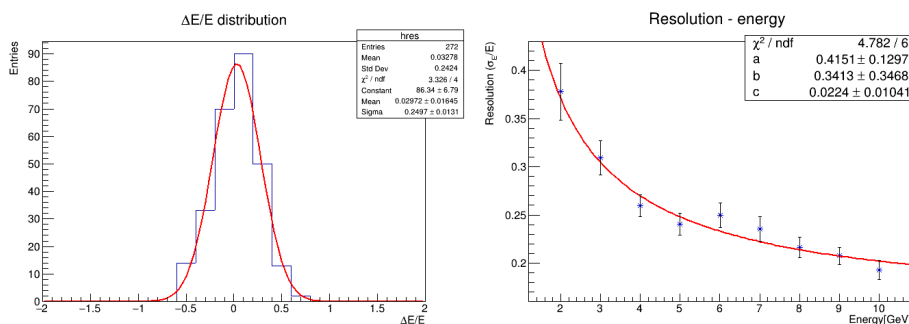


Figure 4.23: On the left: energy resolution of the ECC calorimeter from a simulation of 6 GeV electron showers. On the right: resolution dependence on the shower energy [69].

$$\begin{aligned}
 a &= (0.41 \pm 0.13) \text{ GeV}^{1/2} \\
 b &= (0.3 \pm 0.3) \text{ GeV} \\
 c &= 0.02 \pm 0.01
 \end{aligned}
 \tag{4.14}$$

The energy resolution estimated for a shower having energy 6 GeV is $(25 \pm 1)\%$ [69].

4.4 Conclusions and next steps

Thanks to the study of the data from the test beam performed at DESY in 2019, a new Machine Learning model for electromagnetic shower reconstruction has been developed, and its performances have been compared with a standard algorithm.

Still, the same test beam has provided a large variety of data, from different beam and target configurations. The next step of the analysis will be to compare the reconstructed electromagnetic showers from both algorithms with the Monte Carlo prediction in each configuration, testing the stability of the reconstruction to different conditions.

A more challenging task is the reconstruction of the shower without previous knowledge of the initial track. This requirement is fundamental for Light Dark Matter research, where each signal event is a single scattered electron, in a non predictable position within the target. This can be addressed by building a more complex model, which would recognize the shower directly from the features of the base-tracks in the emulsion films.

Chapter 5

SHiP-charm experiment

5.1 Introduction

The decay of charmed hadrons plays a fundamental role both in the SHiP sensitivity to hidden particles and in the search for tau neutrino interactions. Accurate knowledge of the expected yields of produced charmed hadrons is therefore needed for an accurate evaluation of SHiP performances.

A dedicated experiment, called SHiP-charm, has been proposed, aiming at measuring the associated charm production cross section, induced by the interaction of 400 GeV/c protons impinging on a thick target.

Here, after a brief review of the discovery of the charm quark and the current status of the cross section measurements, the first data-taking session of SHiP-charm, taken in 2018, is presented, by describing the experimental apparatus and the details of the runs. Even if all subdetectors are introduced, the main focus will be dedicated to the structure of the emulsion target, being the subject of my PhD work. Finally, the implementation of this layout in the Monte Carlo framework is discussed.

5.2 Physical background

5.2.1 Observation of the first charm pair production event

During the '60 decade, only the up, down and strange quarks were known, and the quark model itself was yet to be proposed. At that time, the particle physics community was puzzled by the absence of strangeness-changing

neutral currents (SCNC), predicted with the introduction of the Cabibbo angle in 1963 [74]. This suppression was explained by S. Glashow, I. Iliopoulos and L. Maiani in 1970, with the introduction of the so-called GIM mechanism [75]. This mechanism predicted the existence of a fourth quark, c , which motivated searches for new compatible hadron states at the start of the seventies.

Due to the expected short life of the new particles, nuclear emulsions were a suitable detector, thanks to their high resolving power. The Emulsion Cloud Chamber technique, already developed by M.F. Kaplon to study the interaction of heavy particles [76], made it possible to reduce the costs by replacing a pure emulsion detector with a sandwich of passive material and thin emulsion films.

A main advantage of an ECC target is the freedom in the choice of the material for the passive layers. The research group lead by Nishimura and Niu combined low and high Z material sections, in order to separate charged cosmic rays interactions from secondary electromagnetic showers produced by gamma rays. Moreover, the tracking of charged particles was aided by the introduction of a two-fold emulsion tracker, where two layers of nuclear emulsions were coated on both sides of a plastic base.

Analyzing the data collected from a set of emulsion chambers (like the

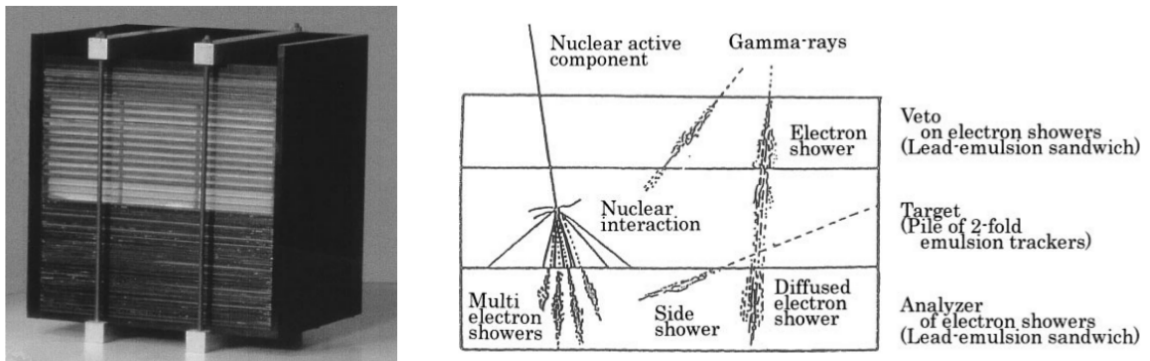


Figure 5.1: Picture and schematics of the compact emulsion chamber used at airplane altitude [77].

one shown in Figure 5.1) exposed in an airplane, in 1971 Niu's group observed a production of two short lived particles, not compatible with any of the strange and resonance states known at the time [78]. The original displays of the event are shown in Figure 5.2: there are two clear separate kinks, represented between B and B' and C and C'. The observation of elec-

tromagnetic showers coming from π^0 decays confirmed two-body decays into a neutral pion and a charged hadron. Further analyses of this event confirmed the observation of the first charm pair production, three years before the discovery of the J/ψ particle [79] (the first charm-anticharm single state observed, marking the discovery of the charm quark).

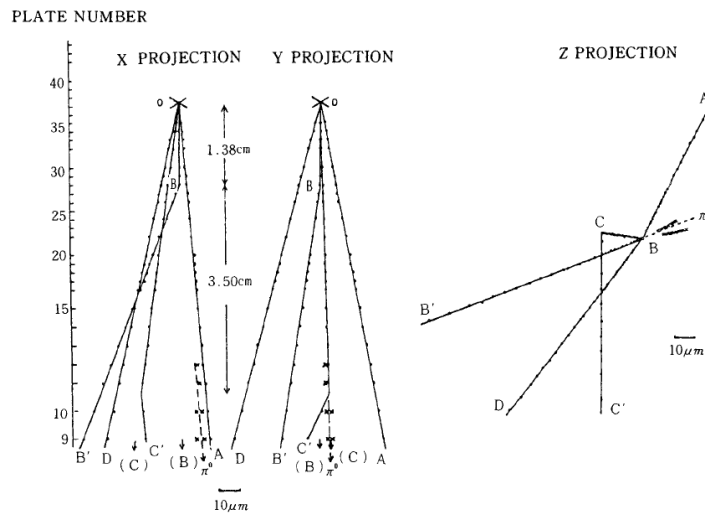


Figure 5.2: First charm pair production observed in 1971, from detection of cosmic ray interactions in nuclear emulsions. Two kinks have been observed, at distance 1.38 cm and 4.88 cm from the main vertex, along with showers from π^0 decays [78].

As the search for new particles gradually moved from cosmic rays to high-energy accelerators, the history of nuclear emulsion films has encountered periods of great breakthroughs and discoveries in particle physics, but also long years of decline due to the low efficiency in processing the enormous amount of data coming from accelerator experiments. In a review of 2008 dedicated to this charm event [77], Niu asserted that ‘what is its strength is also its weakness.’ In the last decades, the technological advances in automated scanning and reconstruction systems provided a great help in addressing this issue, allowing the usage of nuclear emulsion in large experiments. However, the principle still applies, and further research should be pursued towards innovative data reconstruction and analysis algorithms, able to cope with increasing particle intensities and densities.

5.2.2 Current knowledge of charm hadroproduction

In the Standard Model of Particle Physics there are three quarks with mass heavier than the QCD scale (Λ_{QCD}): the charm, bottom and top quarks, whose production cross sections can be predicted with perturbative QCD. Processes involving hadrons in initial states are usually studied by applying the parton model: an incoming hadron beam H is considered equivalent to a beam of constituents, quarks and gluons, with a longitudinal momentum distribution characterized by the parton density functions (pdfs), $f_i^{(H)}(x, \mu)$, depending on the scale μ and on the longitudinal momentum fraction x of the parton. The total hadronic cross section can therefore be derived from the convolution of the partonic hard scattering cross section and the parton distribution functions of the colliding hadrons:

$$\sigma_{H_1, H_2}(p_1, p_2) = \sum_{i,j} \int dx_1 dx_2 f_i^{(H_1)}(x_1, \mu) f_j^{(H_2)}(x_2, \mu) \hat{\sigma}_{ij}(x_1 p_1, x_2 p_2, \alpha_s(\mu), \mu), \quad (5.1)$$

where the last term is a perturbative expansion in the strong coupling constant α_s ,

$$\hat{\sigma}_{ij}(x_1 p_1, x_2 p_2, \alpha_s(\mu), \mu) = \sum_l \hat{\sigma}_{ij}(x_1 p_1, x_2 p_2, \mu) \alpha_s^l(\mu). \quad (5.2)$$

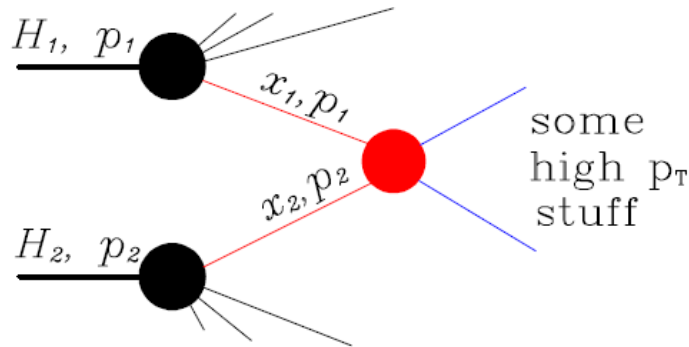


Figure 5.3: Representation of the parton model description of an interaction involving two hadrons H_1 and H_2 . Taken from the lecture notes in Ref.[80].

The pdfs are universal, in the sense that they do not depend on the particular process considered. A pictorial representation is given in Figure 5.3.

Even if the above procedure can be applied to all three heavy quarks, some fundamental differences need to be acknowledged. The top quark,

having the largest mass and the shortest lifetime, decays well before hadronizing, while the bottom and charm quarks are always observed as intermediate hadron states. For the latter particles, therefore, the hadronization transient needs to be included in the theoretical computation, but unfortunately it cannot be described by perturbative QCD, increasing the uncertainty on the predicted cross section.

Figure 5.4 shows the prediction of the charm hadroproduction cross section at the Next-To-Leading Order (NLO), along with a collection of measurements from fixed-target and collider experiments.

Even if there is a good agreement, the systematic errors on predictions are dominated by large theoretical uncertainties: the renormalisation and factorization scale dependence, the value of the heavy quark mass, and the parton distribution functions themselves. Since m_c is not so far above the Λ_{QCD} scale, a large contribution is expected from higher order corrections, causing perturbative QCD to lose predictive power. Experimental measurements become thus necessary to constrain theoretical calculations.

Focusing on the configuration of the SHiP experiment, which is a 400 GeV/c proton beam dump facility, the measured and predicted cross-sections are reported in Table 5.1. Due to the thickness of the SHiP target, particular attention is devoted to the study of the generation of charmed resonances from secondary hadrons. A “cascade production” is referred to as an associated charm production happened after any previous elastic or inelastic interaction of the proton beam. A Monte Carlo simulation of this effect has been performed with iterative generations of events from Pythia6, tuned with the differential cross section data provided from the E769 experiment (the details of the algorithm have been explained in section 3.1.1). This simulation predicts a charm yield of a factor 2.3 times larger than the production from prompt protons only [54], which should be compared with experimental data. This is the starting point in the design of a new experiment aiming at measuring charm production cross section.

	exp NA27	th NLO ($m_c = 1.3$)	th NLO ($m_c = 1.5$)	th NLO ($m_c = 1.8$)
$\sigma[\mu\text{b}]$	18.1 ± 1.7	$24.3^{+80.1}_{-12.4}$	$10.1^{+22.6}_{-4.8}$	$3.12^{+4.86}_{-1.36}$

Table 5.1: Comparison of charm production cross sections in pp collisions from the NA27 experimental measurement [82] and the NLO theoretical predictions, with typical values of the charm mass (in GeV). From the SHiP-charm proposal [81].

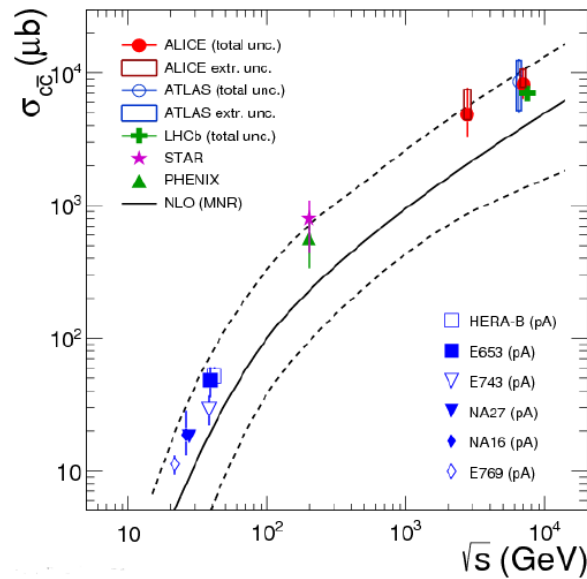


Figure 5.4: Charm production cross section in nucleon-nucleon collision as a function of \sqrt{s} , compared to measurements from different experiments. Solid and dashed lines represent the theoretical predictions at NLO order and its uncertainties, respectively [81].

5.3 Optimization run of the SHiP-charm experiment

At the start of October 2017, the SHiP Collaboration submitted the proposal of a new experiment to measure the double-differential cross section $\frac{d^2\sigma}{dE d\theta}$ of associated charm hadro-production [81]. A first run has been performed in 2018, collecting about one tenth of the total SHiP-charm statistics, at the same time providing a prototype used as input to optimize the design of the larger data taking run.

5.3.1 Experimental layout

The 400 GeV/c SPS proton beam impinges on a ECC target, where the production and decay vertices of charmed hadrons are identified. The target is followed by a magnetic spectrometer, designed to measure the momentum and charge of decay daughters, through their deflection in a magnetic field of about 1 T. The downstream section of the detector is dedicated to muon identification, through a dedicated filter. The lateral view of the general

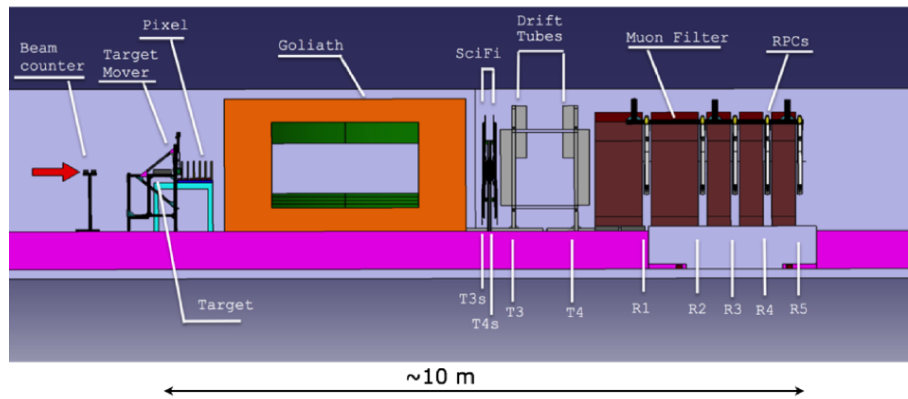


Figure 5.5: Lateral view of the experimental apparatus used in the 2018 optimization run.

layout is shown in Figure 5.5.

ECC target

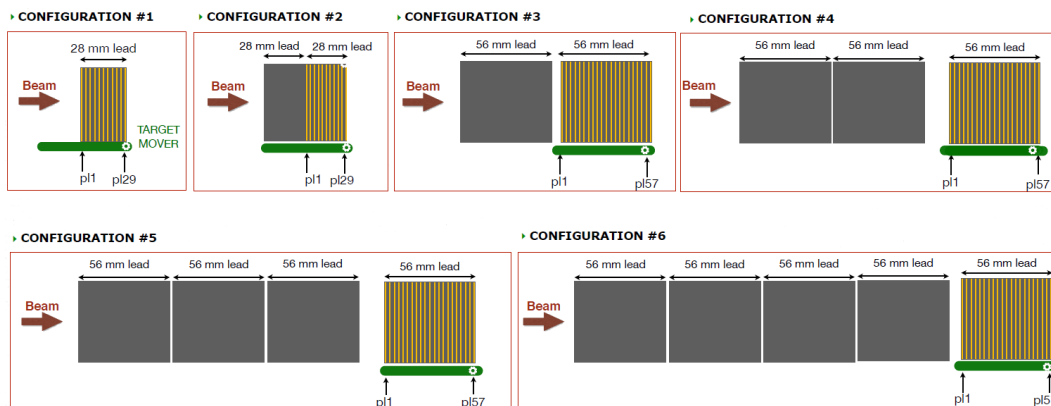


Figure 5.6: Layout of the six different SHiP-charm target configurations.

In order to study the production of charmed hadrons at different depths, six different target configurations have been designed, where the ECC detector is placed after an increasing number of lead passive blocks (Figure 5.6). The first two configurations employ an ECC target with 29 emulsions and 28 passive layers: six replicas have been prepared, from here onwards referred as “runs”. Instead, the other configurations employ an ECC target with 57 emulsions and 56 passive layers, and three runs have been prepared for each configuration. 1 mm-thick lead slabs are used as passive material for almost all the runs, and the lead depth in the whole

target goes from 28 mm to 280 mm, covering a maximum of 2.79 nuclear collision lengths (1.59 interaction lengths).

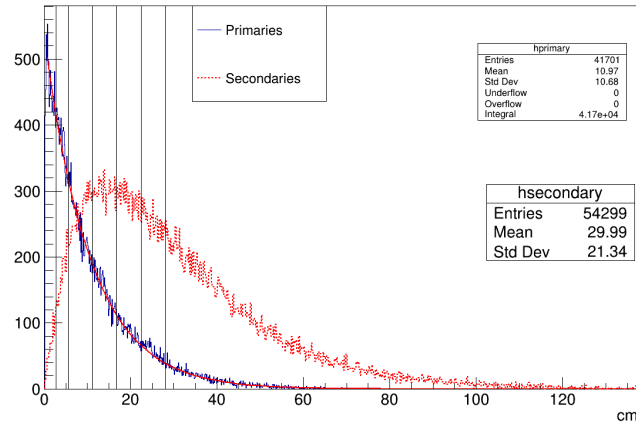


Figure 5.7: Z position of produced charm vertices, comparing primary and cascade production. The lines represent the regions covered by the 2018 runs.

The position of charmed hadron interaction vertices along the beam direction in the target is reported in Figure 5.7, as obtained from the Monte Carlo simulation. Production from prompt protons is shown in blue, and the cascade production in red.

Emulsion films have a transverse surface of $(12.5 \times 9.9) \text{ cm}^2$, required to be exposed to a beam less than 1 cm wide with uniform density. Therefore, a mechanical stage has been designed (Figure 5.8), moving the target in order to receive the beam on its whole area. The movement pattern is synchronized with the proton spills provided by the SPS accelerator, each of them lasting 4.8 s. Defining as z the beam direction, the moving pattern is the following: during a spill, the target moves along the x direction at the uniform speed of 2.6 cm/s, covering the horizontal length. Between two spills, the target is moved vertically and the same length is covered in the opposite direction during the next spill. The procedure is repeated until the end of the target area, after 5 or 10 spills, depending if the vertical gap is set to 2 cm or 1 cm (Figure 5.9). These two configurations allow to test the alignment with the fixed downstream detectors in different conditions.

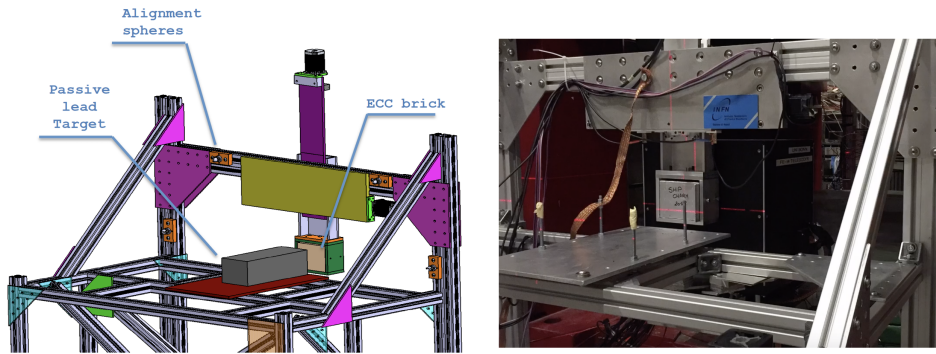


Figure 5.8: On the left, technical drawing of the target mover. On the right, a picture of the installed stage during a test exposure on a ECC target.



Figure 5.9: Pattern of the target movement in the 5 spills (left) and 10 spills (right) configurations.

Magnetic Spectrometer

The magnetic field is provided by the Goliath magnet, which is permanently present in the H4 Area at CERN. Its dimensions are $3.6 \times 2.79 \times 4.5 \text{ m}^3$.

Three subdetectors are employed for the spectrometer: one upstream of the magnet, and a combination of two different technologies downstream.

Immediately downstream of target, a pixel tracking detector is installed, made of six planes, each formed by two ATLAS IBL hybrid pixel detector modules. The modules consist of a pixelated silicon sensor and a FE-I4 readout chip [83]. The FE-I4 clock runs at 40 MHz, which is therefore the maximum timing resolution. The sensor structure is composed by 160 columns and 336 rows, with a pitch of $50 \mu\text{m}$ for the rows and $250 \mu\text{m}$ for the columns. To compensate for the different pixel resolution in the two dimensions, the stations are alternatively rotated by $\pi/2$ around the beam axis. The total active area covered by the pixel tracker is 11.3 cm^2 per plane. A picture of the box containing the pixel modules is shown in Figure 5.10.

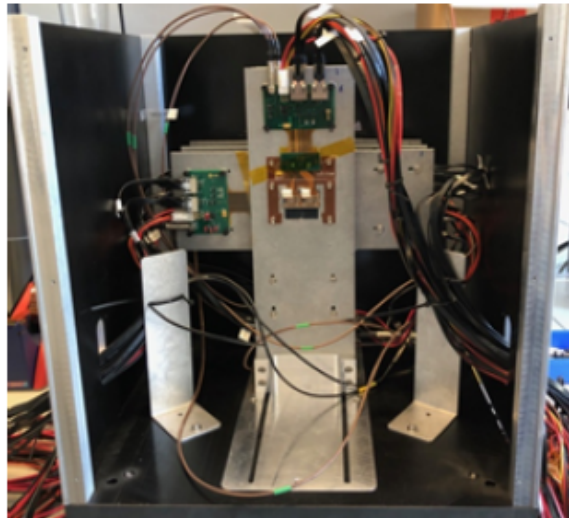


Figure 5.10: Picture of the box containing the pixel modules, as seen from the beam.

Downstream of the magnet, Scintillating Fibre Trackers (SciFis) cover a transverse size of $40 \times 40 \text{ cm}^2$ (readout in the central $13 \times 13 \text{ cm}^2$ area) centered in the beam axis, where the track density is higher. This detector is made of $3 \times 12 \text{ cm}^2$ wide *mats* of scintillating fibers, emitting photons when traversed by a charged particle. A *mat* is a matrix structure, consisting of six staggered fibre layers with horizontal pitch of $270 \mu\text{m}$ and a total length of

40 cm. Each module consist of two different planes, providing XU and YU coordinates, where the U direction is defined by applying a stereo angle of $\sim 2^\circ$ to the X or Y direction.



Figure 5.11: Picture of SciFi and Drift Tubes detector configurations.

Lower energy charged particles are swept off by the magnetic field from the Goliath, outside of the acceptance of SciFi modules. The detection of these particles is assigned to drift tubes stations, already installed for a muon flux measurement for SHiP [84], happened immediately before the SHiP-charm optimization run. The drift tubes are prototypes from the OPERA experiment, built with 38 mm outer diameter of aluminum tubes, filled with Argon and CO_2 , in a mixing ratio of 80:20. The hit positions in the drift tubes are obtained from the relation between the measured drift-time and the distance of the track to the wire, called $r - t$. This relation is first established from the time distributions of simpler events, then applied to all the data. The pattern recognition algorithm selects hits and clusters to form track candidates, finally leading to the track fit. The drift tube resolution has been measured to be $373 \mu\text{m}$ during the muon flux measurement.

The configuration of the two subdetectors downstream of the magnet is shown in Figure 5.11.

Muon Tagger

The muon tagger is the most downstream element of the experimental apparatus, with the task of identifying muons with high purity and thus tagging the muon decay channel of charmed hadrons.

The detector is made of five planes of single-gap Resistive Plate Chambers (RPCs), interleaved with 1×80 cm and 3×40 cm-thick iron slabs. In addition, a 80 cm-thick iron slab is positioned immediately upstream of the first chamber. The layout is shown in Figure 5.12.

The RPCs cover an active area of 1.9×1.2 m² and they consist of 2 mm-thick Bakelite electrodes covered with graphite paint and a 2 mm wide gas gap. They are operated in avalanche mode with a standard mixture ($\sim 95\% C_2H_2F_4 \sim 4.5\% C_4H_{10} \sim 0.5\% SF_6$). The chambers are read out by two orthogonal panels of copper strips, with 1.0625 cm pitch and a maximum length of about 2 m.

The performance of the RPCs have been tested with cosmic rays at CERN: when one chamber is tested, data acquisition is triggered by the coincidence of the remaining RPCs, placed both upstream and downstream of the studied detector. Improvement has been achieved with better system alignment during the actual data run. The RPCs reached efficiency levels above 98% with a position resolution of about 3 mm [85].

5.3.2 Summary of the data taking

The first data for the SHiP-charm measurement have been taken at the end of July 2018. This optimization run has the objective of studying the reconstruction of hadronic interactions and decay vertices in emulsion in a high density environment. It also needs to match the data in the moving ECC with the stationary pixel telescope. Finally, this run studies the challenges of a global reconstruction, performing momentum measurement by including the data from detectors upstream and downstream of the Goliath magnet.

A total of 24 runs with ECC targets have been performed, and the number of protons on target ($N_{p.o.t.}$) has been measured by a scintillator counter installed upstream of the target. The number of expected charm pairs produced in the target can be estimated from the currently known cross section and the fraction of hadrons produced in each configuration, according to

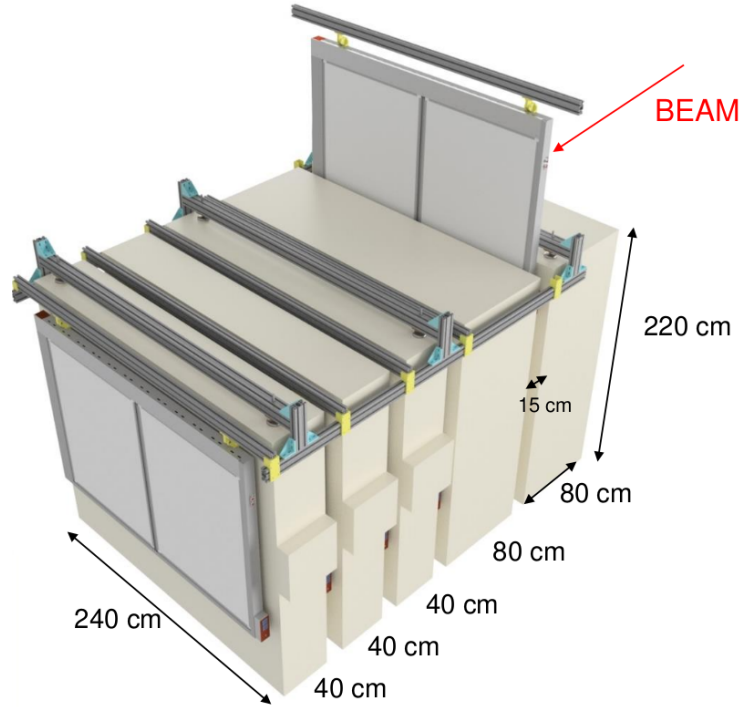


Figure 5.12: Schematics of the muon tagger, showing the thickness of the five iron slabs and the position of the RPCs.

the Monte Carlo simulation of primary and cascade production:

$$N_{pair}^{prim} = N_{p.o.t.} \cdot \frac{\sigma_{c\bar{c}}}{\sigma_{pN}} \cdot f_{ECC}^{prim} \quad (5.3)$$

$$N_{pair}^{cascade} = N_{p.o.t.} \cdot \frac{\sigma_{c\bar{c}}}{\sigma_{pN}} \frac{N_{tot}^{casc}}{N_{tot}^{prim}} \cdot f_{ECC}^{cascade} \quad (5.4)$$

where:

- $\frac{\sigma_{c\bar{c}}}{\sigma_{pN}}$ is the fraction of charm pairs produced in proton interactions, for a 400 GeV proton beam colliding on a molybdenum target;
- N_{tot}^{casc} and N_{tot}^{prim} are the total numbers of generated charmed hadrons, given from the Monte Carlo simulation, from cascade interaction and proton interaction, respectively;
- f_{ECC}^{prim} and $f_{ECC}^{cascade}$ are the fractions of charm pairs produced in a specific ECC target, for primary interactions and cascade production, respectively.

Table 5.2 shows a summary of the exposure runs, separating the different six configurations of the emulsion target. A total of 1.56×10^6 protons on target have been integrated on 1032 emulsion films. For the details of the single runs, please refer to Appendix A.

Configuration	N runs	N Emu. films	Integrated p.o.t.	Expected produced primary charm	Expected produced cascade charm
CHARM1	6	174	5.4×10^5	142	11
CHARM2	6	174	5.2×10^5	116	31
CHARM3	3	171	1.0×10^5	32	20
CHARM4	3	171	0.8×10^5	15	18
CHARM5	3	171	1.6×10^5	17	33
CHARM6	3	171	1.6×10^5	11	31
TOTAL	24	1032	1.56×10^6	333	144

Table 5.2: Summary of the 2018 data taking session for the SHiP-charm experiment.

The hits from protons passing through the target without interacting have been the first and clearest data to be analyzed, providing accurate information on the beam structure. The profile of the beam in the transverse plane can be seen in Figure 5.13, as recorded by the pixel detectors. Within the spill time of 4.8s, a clear variation of the center of gravity has been observed, hinting to a movement of the beam spot during a single spill.

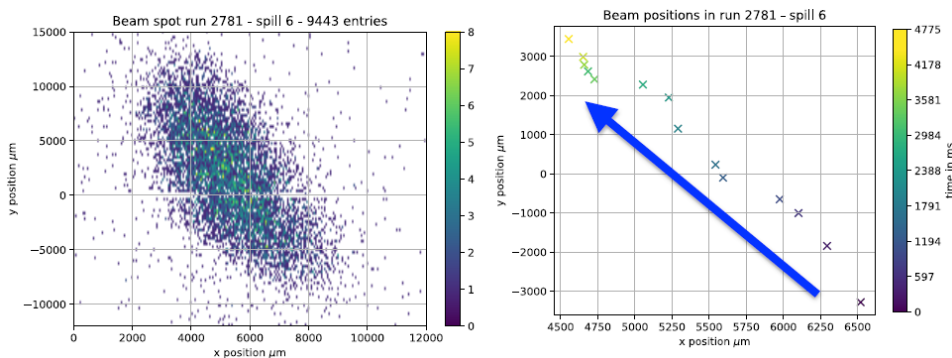


Figure 5.13: Shape of the proton beam, from the pixel hits belonging to the CHARM2-RUN1 dataset.

In the emulsion data, the beam is spread in five or ten lines due to the movement of the target, with each line corresponding to a spill. The distribution of the spills can be seen by selecting low angle base-tracks

($\tan\theta < 0.1$), as reported in Figure 5.14 from the data in the most downstream emulsion film.

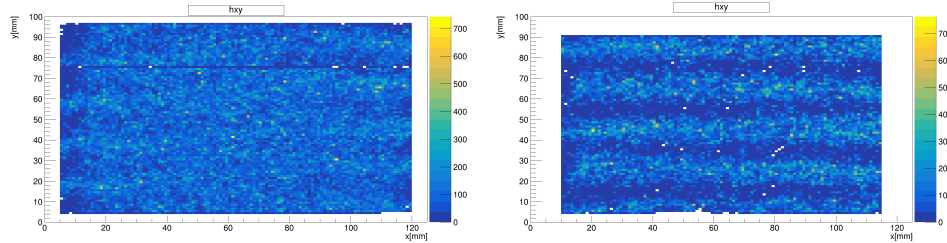


Figure 5.14: Low angle emulsion base-tracks ($\tan\theta < 0.1$), in a configuration with ten proton spills (CHARM1-RUN2, left) and five proton spills (CHARM1-RUN6, right), taken from the most downstream emulsion film.

5.4 Event simulation

The experimental apparatus employed in the 2018 data run has been implemented in the FairShip software framework (Figure 5.15), setting the position of the subdetectors according to the measurements provided by the CERN survey team.

General simulations of all interactions of the 400 GeV protons are produced with Geant4, to replicate the hits registered by the subdetectors during the runs. On the other side, the charm production is simulated with the Pythia 6 generator, tuned with the differential cross section data from the E791 experiment [86] and including the contribution of cascade production. The produced event is then passed to Geant4 for the standard particle propagation.

5.4.1 Acceptance of the magnetic spectrometer

The magnetic field produced by the Goliath magnet has been accurately mapped by the CERN staff in 2017 [87], which has interpolated the measurements from 18 Hall probes in an equally-spaced full three-dimensional grid of the field. The B_y component of the field is shown in Figure 5.16, from the imported map in the FairShip software framework.

The geometrical acceptance of the SHiP-charm magnetic spectrometer to the charged daughters of charmed hadrons has been estimated with the following two requirements:

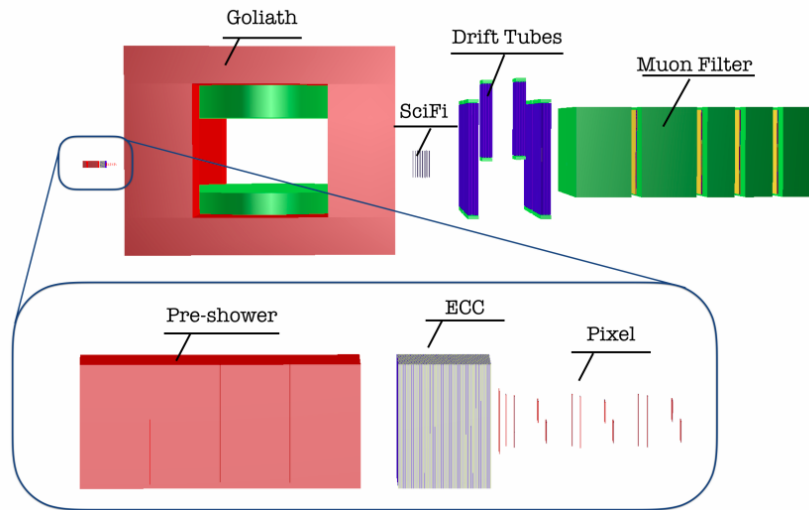


Figure 5.15: Layout of the SHiP-charm geometry implemented in FairShip.

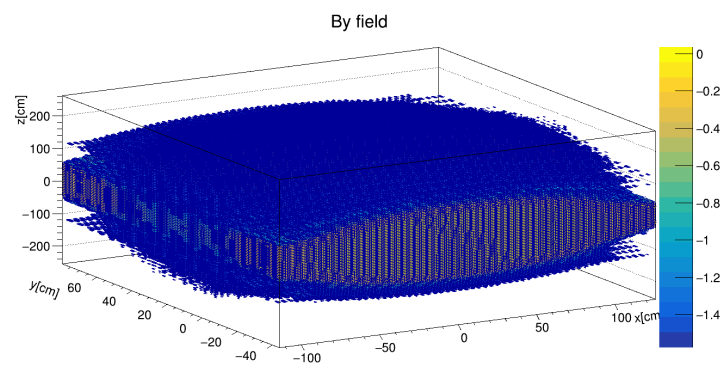


Figure 5.16: 3D map of the B_y field component, units are in Tesla (T).

- The track exits the ECC target and enters in the pixel detector upstream of the magnet. The fraction of decay daughters entering the pixel detectors amounts to $(89.3 \pm 0.1)\%$;
- The track is detected in the downstream stations. The acceptance of SciFi stations amounts to $(26.1 \pm 0.1)\%$. The contribution of drift tubes allows to increase this acceptance to $(60.5 \pm 0.2)\%$.

The acceptance as a function of the particle momentum is reported in Figure 5.17.

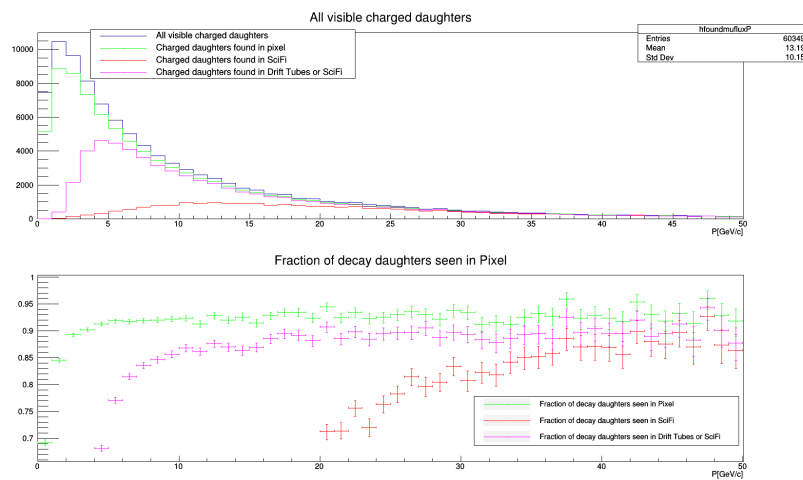


Figure 5.17: Momentum distributions of charged charmed hadrons decay daughters, and the components which arrive at the various subdetectors of the SHiP-charm magnetic spectrometer. On the lower side, the corresponding acceptances are reported.

5.4.2 Event simulation in the emulsion target

Initially, the Monte Carlo events are produced by assuming the emulsion target fixed, and simulating the beam impinging on its center. The event display can be used to check the track trajectory in all the subdetectors for each simulated event, by connecting the MC hits recorded in each active volume. A display of such event is reported in Figure 5.18.

After the simulation, the hits recorded in the emulsion films are spread within the target, reproducing its movement in the transverse plane.. The simulated Monte Carlo events are grouped in five or ten virtual proton spills, then a virtual timestamp t_{pot} is randomly generated between 0 and

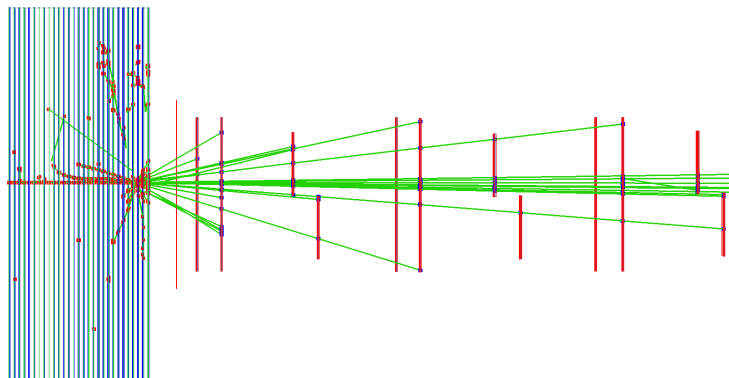


Figure 5.18: Event display of a simulated proton interaction in the emulsion target. Downstream of the target, hits from the pixel detectors can be seen.

4.8 s for each MC event. Defining $dimX$ and $dimY$ as the transverse emulsion dimensions, all hits from that event are spread along x assuming a uniform movement of the target with $v_x = 2.6$ cm/s:

$$x_{em} = x_{sim} + (v_x \cdot t_{pot} - dimX/2) \quad (5.5)$$

On the other side, the y coordinate is set according to the virtual proton spill the MC event is assigned to:

$$y_{em} = y_{sim} + (nspill \cdot y_{gap} - dimY/2 + offsety), \quad (5.6)$$

where y_{gap} is the distance between two consecutive spills and $offsety$ is the position of the first spill.

Each MC hit records the position and the angles of the particle passing through the virtual volume. A Gaussian smearing with $\sigma_{Tx, Ty} = 3$ mrad is applied to the angles, to simulate the angular resolution of the emulsion.

Hits from charged particles are finally passed to the reconstruction algorithm, if their kinetic energy is larger than 30 MeV and the θ angle is lower than 1 rad. The lower energy threshold is required to accurately track a real particle traversing the emulsion plate, while the upper angular threshold correspond to the maximum angle acquired during the scanning of the emulsions in this detector configuration. Additionally, a random fraction of the hits can be discarded, to reproduce inefficiencies of the single films.

Chapter 6

Analysis of the SHiP-charm emulsion data

6.1 Reconstruction of emulsion data

The optimisation run of the SHiP-charm experiment was performed in 2018, with two main objectives: the reconstruction of hadronic interactions from the 400 GeV proton beam in a high density environment, and search for charmed hadron decays.

A total of 1032 nuclear emulsions films were exposed. Emulsion films have been scanned in Naples and Zurich laboratories. Deposited grains are converted into digitized clusters and analyzed. The tracks left by charged particles in the single films are reconstructed as *base-tracks*. The description of this procedure has been provided in section 4.2.3. From these data, the next tasks are to reconstruct the tracks of the particles in the whole emulsion target, and the vertices pointed by these tracks.

The vertex topologies searched in this analysis are proton interaction vertices and charmed hadron decay vertices. The selection is performed through Boosted Decision Trees, trained from Monte Carlo simulations of protons impinging into SHiP-charm target. The details are presented in this chapter, after a brief overview of track and vertex reconstruction procedure in the emulsions. Finally, current results and next steps are discussed.

6.1.1 Track reconstruction

Tracking is the task of estimating the trajectory of a charged particle, starting from a dataset of hits in a group of detector units. First, a track is found by grouping together the hits belonging to the same particle. Then a fit is performed, to estimate track parameters and their associated covariance matrix.

A common track finding procedure is *track following*: tracks are found sequentially in the detector units, starting from an initial track segment (the *seed*), which is usually placed as the most upstream or most downstream detector unit. The algorithm used to reconstruct tracks from SHiP-charm emulsion data has been originally designed for the OPERA experiment [88] and applies a *Kalman filter*, an improved version of the track following procedure. A Kalman filter alternates the track finding and track fitting tasks, by applying the following prediction and update steps for each detector unit:

- At the prediction step, the track is extrapolated to the next detector unit, estimating its position there;
- At the update step, if a measurement is found compatible with the prediction, it is included in the track candidate, and the track parameters and covariance matrices are updated with the new information.

Each track is followed until it is not found for more than three consecutive detector units.

The track reconstruction has been tested in Monte Carlo simulations of the SHiP-charm emulsions in CHARM1 target configuration, integrating a total of 135000 protons on target. The goodness of the track is given by the following estimators:

- True hit efficiency (or hit utilisation): the ratio of segments correctly associated to the same Monte Carlo particle, with respect to the true total number of segments left by the particle;
- Track purity: the ratio of segments correctly associated to the same Monte Carlo particle, with respect to the total number of segments reconstructed in the track.

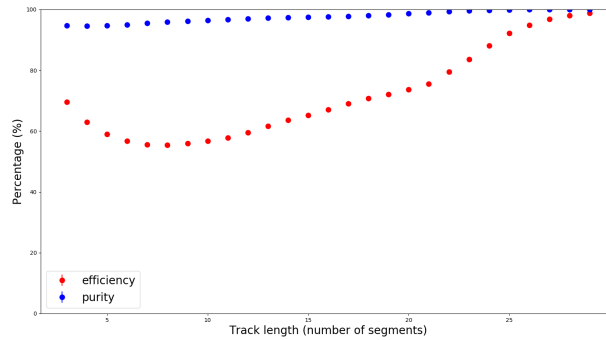


Figure 6.1: Track reconstruction efficiency (in red) and purity (in blue), as a function of the length of the tracks, expressed as the number of traversed emulsion films.

The estimators are evaluated for all reconstructed tracks, as a function of their length in number of associated base-tracks. The results are shown in Figure 6.1: longer particles are tracked more clearly and with larger efficiency.

6.1.2 Vertex reconstruction

Vertex reconstruction is the task of finding and estimating the production point of a set of particles. Several types of vertices can be distinguished:

- The primary vertex, given as the collision point of the beam with the target particle (or two beam particles, in case of a collider experiment);
- A secondary interaction vertex, where a particle interacts with the material of a detector. This category includes both electromagnetic and hadronic interactions;
- A secondary decay vertex, where an unstable particle decays in the detector volume.

In the ECC geometry, the majority of the vertices lie in the more dense and thicker passive layers, while the thinner and lighter emulsion films contain the data used as input for track and vertex reconstruction. A Kalman filter is applied with steps similar to the tracking algorithm, with the aim of finding the tracks belonging to a same vertex (*vertex finding*) and

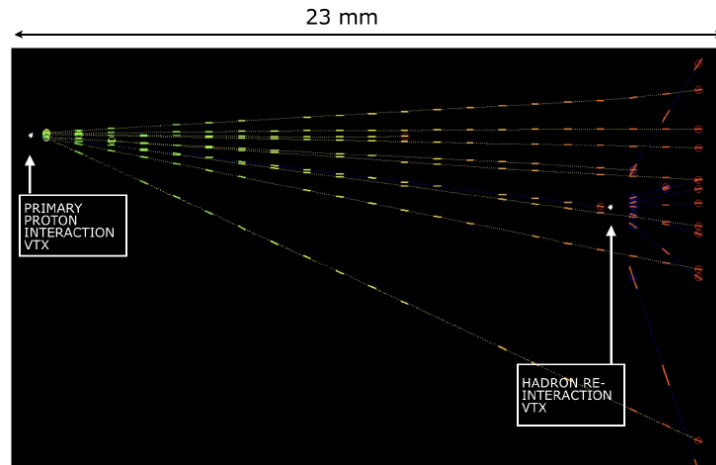


Figure 6.2: Display of a primary proton vertex and an hadronic interaction vertex.

estimating the parameters (*vertex fitting*). The vertex finding is initiated by pairs of neighbor tracks, then the combinations of 2-tracks vertices are fitted into n-tracks vertices, ranked according to the number of tracks $ntrks$ and the fit probability $Prob_{vtx}$:

$$R_{vtx} = 10 * ntrks + Prob_{vtx} \quad (6.1)$$

Each extremity of a track (start and end point) can be associated to at most one vertex, chosen as the one with the best rank R_{vtx} .

Figure 6.2 shows a proton interaction vertex from the simulation of an exposed SHiP-charm brick, after all the reconstruction algorithms. A second vertex can be seen, from an hadronic re-interaction.

6.2 Reconstruction of proton interactions

In each ECC, the density of protons on target varies from $10^2/\text{cm}^2$ to $10^3/\text{cm}^2$, depending on the conditions of the exposure. As the depth of the target increases, the protons start sequences of primary interactions, hadronic re-interactions and electromagnetic showers, increasing the density of segments reconstructed in each emulsion film up to $5 \times 10^4/\text{cm}^2$.

Each proton interaction produces about 15 charged particles and 10 photons. Simulations predict about 10^5 vertices within a single ECC, from which thousands come from primary inelastic proton interactions.

6.2.1 Boosted Decision Tree classification

After reconstruction, vertices from inelastic hadronic interactions need to be identified, separating them from the background of random combinations and electromagnetic showers.

The Boosted Decision Tree (BDT) is a multivariate classifier commonly used in Particle Physics, where the performances of many decision trees are “boosted” by updating the weights assigned to each one. In the Adaptive Boost (AdaBoost [89]) algorithm, provided by the ROOT TMVA framework[72], the weights are computed iteratively, using as input parameter the misclassification rate err at the previous iteration:

$$\alpha = \frac{1 - err}{err}. \quad (6.2)$$

Misclassified events are given a higher event weight in the training of the following tree. Let us assume to have a number of decision trees equal to $N_{collection}$, each of them giving a binary output $h_i(x)$ (which can be 0 or 1) with a misclassification rate α_i . The boosted event classification is given by

$$y_{Boost}(x) = \frac{1}{N_{collection}} \cdot \sum_i^{N_{collection}} \ln(\alpha_i) \cdot h_i(x). \quad (6.3)$$

An optimal performance of the *AdaBoost* is achieved by combining small individual decision trees, with a depth of about 3 selections. In this way, even if each tree has very little discrimination power by himself, it is less prone to overtraining and thus it can more easily adapt to fluctuations of the data sample.

Starting from a reconstructed vertex in the ECC target with number of tracks N_{trks} , the following variables, shown in Figure 6.3, are used as input for the BDT classification:

- **Probability:** this is computed from the χ^2 and the number of degrees of freedom $ndeg$ of the vertex fit, with $ndeg = 2 * N_{trks} - 3$. This probability is close to 1 for true interaction vertices, and it is much lower for random combinations;
- **Maximum angular distance** between all the tracks associated to the vertex;

- **Mean impact parameter** of tracks with respect to the reconstructed vertex;
- **Maximum impact parameter** of tracks with respect to the reconstructed vertex;
- **Fill factor of tracks at the vertex**, defined as the ratio between the number of base-tracks building the vertex and the number of emulsion films downstream of the vertex.

For each of the six SHiP-charm target configurations, the weights of the BDT are optimized according to the vertices reconstructed in Monte Carlo simulations of 400 GeV protons impinging on an ECC target. The output of the BDT for both signal and background in a training and test sample are shown in Figure 6.4. The vertices reconstructed from the simulations are employed to determine the efficiency of analyzed data runs, which is affected by the different conditions of the exposures and of the nuclear emulsion films. The efficiencies are reported in Table 6.1.

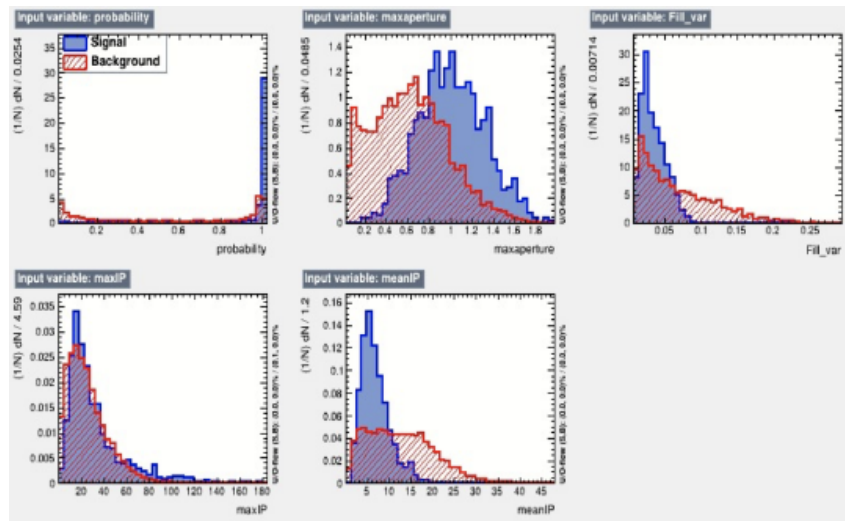


Figure 6.3: Distributions of input variables used for the training of the BDT [90]. Spatial units are μm .

6.2.2 Results and interaction length fit

The absorption of a proton beam due to inelastic hadronic interactions in the material is described by an exponential decrease of the number of protons as a function of the depth x of the target:

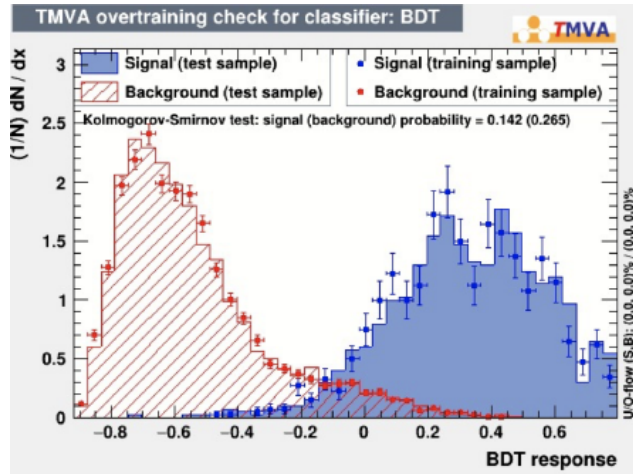


Figure 6.4: Output of the BDT classifier for training and test sample [90].

Configuration	Efficiency (%)	Configuration	Efficiency (%)
CHARM1-RUN1	83	CHARM2-RUN4	55
CHARM1-RUN2	99	CHARM3-RUN1	70
CHARM1-RUN4	53	CHARM4-RUN1	38
CHARM1-RUN5	49	CHARM5-RUN1	51
CHARM2-RUN2	57	CHARM6-RUN1	66
CHARM2-RUN3	41		

Table 6.1: Vertex reconstruction efficiency for different analyzed data runs.

$$N(x) = N_0 e^{-\frac{x}{\lambda_{int}}}, \quad (6.4)$$

where N_0 is the initial number of protons and λ_{int} is the nuclear interaction length of the material.

The reconstructed vertices in the SHiP-charm dataset come from configurations at different depths: a normalizing factor is applied, to correct for the inefficiency of each run and to scale all runs to the same number of incoming protons on target. The overall distribution of the position of interaction vertex candidates in a ~ 365 mm long emulsion target is obtained. The contributions of both primary proton beam interactions and hadronic re-interactions are included, as it can be observed from the data-MC comparison shown in Figure 6.5.

While the primary proton component follows an exponential distribution, hadron re-interactions can be parameterized as a second-order polynomial. The fit on the data leads to an observed value of interaction length:

$$\lambda_{int}^{data} = (182_{-16}^{+19}) \text{ mm}, \quad (6.5)$$

for the Monte Carlo sample, a compatible value $\lambda_{int}^{MC} = (175 \pm 5)$ mm is obtained.

6.2.3 Matching with pixel telescope

The pixel tracker is the first electronic detector downstream of the ECC, placed at a distance of 1.8 cm from the last emulsion layer. Matching the emulsion tracks with the pixel ones allows to provide a timestamp for the event, and it is the most challenging step of global event reconstruction.

Obtaining a good set of matched tracks requires an accurate alignment between the two different subdetectors. The target moves at about 2.6 cm/s during each spill, while the pixel station is stationary. A dedicated alignment and matching procedure has been designed [91], using as input reconstructed tracks from emulsions and from the first electronic detector downstream, the pixel telescope. A short description of this procedure is provided here, due to its fundamental role in the overall data analysis.

Before the matching, the timestamp from the pixel detector is used to translate the hits into the moving emulsion frame. On the other side, emulsion tracks are selected from matching if they have a segment in the last

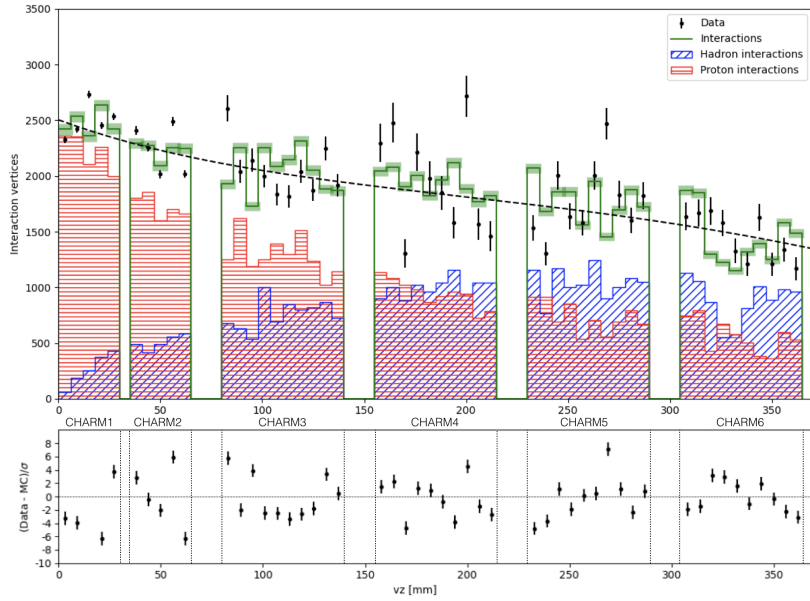


Figure 6.5: Position of reconstructed vertices along the beam axis. The primary proton and hadron re-interaction components are distinguished in the Monte Carlo sample, while a global fit is performed on the data sample [90].

emulsion layer, with angle less than 150 mrad in order to be within the pixel detector acceptance. Fully penetrating tracks are excluded to suppress the contribution of the proton beam. The alignment is performed by minimizing the total χ^2 of the emulsion-pixel track pairs:

$$\chi^2 = \sum_j (\mathbf{r}^T \mathbf{V}^{-1} \mathbf{r})_j, \quad (6.6)$$

with \mathbf{r} defined as the 4-vector $\mathbf{r} = \mathbf{x}^{pix} - \mathbf{x}^{emu} = (\Delta x, \Delta y, \Delta\theta_{xz}, \Delta\theta_{yz})$, and a minimum $\frac{d\chi^2}{d\alpha} = 0$ is found with respect to 8 alignment parameters $\alpha = (x_0, y_0, z_0, \theta_{xz_0}, \theta_{yz_0}, \theta_{xy}, v_x, v_y)$:

- 3 position transformations: x_0, y_0, z_0 ;
- 3 rotation angle offsets: $\theta_{xz_0}, \theta_{yz_0}, \theta_{xy}$;
- 2 components of the target mover velocity: v_x and v_y .

New alignment parameters are then computed as

$$\alpha^1 = \alpha^0 - \left(\frac{d^2\chi^2}{d\alpha^2} \right)^{-1} \bigg|_{\alpha_0} \frac{d\chi^2}{d\alpha} \bigg|_{\alpha_0} \quad (6.7)$$

and the above procedure is repeated. The performance of this alignment has been estimated from 27296 tracks, associated to vertices in the CHARM1-RUN6 emulsion dataset with output of the BDT classifier larger than 0.15 and containing at least six tracks. This requirement allows to select a high-quality sample of reconstructed tracks to study the matching performances. The resulting χ^2 is shown in Figure 6.6. A good matching with the pixel detectors has been found for a total of 16922 tracks, amounting to 62% of the original sample. After alignment, tracks from the moving ECC could be matched to the static pixel detector tracks with spatial resolutions $\sigma_x = 44 \mu\text{m}$ and $\sigma_y = 80 \mu\text{m}$ (Figure 6.7) and angular resolutions $\sigma_{\theta_{xz}} = 4 \text{ mrad}$ and $\sigma_{\theta_{yz}} = 3 \text{ mrad}$ (Figure 6.8).

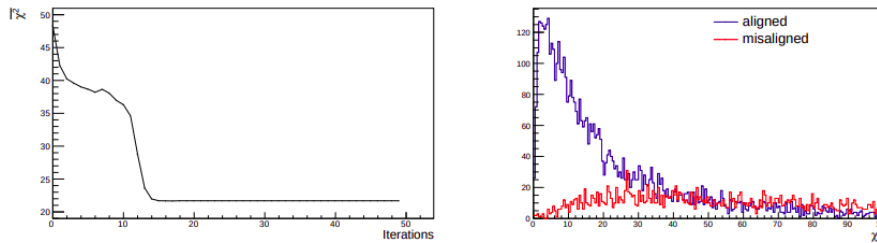


Figure 6.6: Results of the alignment between emulsion and pixel tracks. On the left, the average χ^2 per track with respect to the number of alignment iterations. On the right, the χ^2 distribution before and after alignment [91].

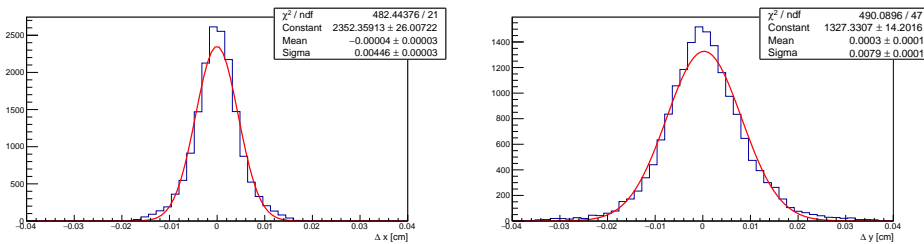


Figure 6.7: Position residuals along x (on the left) and along y (on the right) coordinates, after matching between emulsion and pixel tracks [91].

6.3 Search for associated charm production

6.3.1 Event topology

About one every thousand of proton interactions in the lead target produces a $c\bar{c}$ pair, which immediately hadronizes in two charmed hadrons.

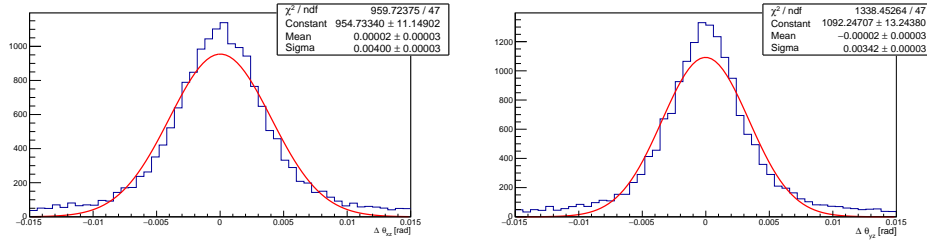


Figure 6.8: Angular residuals in the zx plane (on the left) and in the zy plane (on the right) coordinates, after matching between emulsion and pixel tracks [91].

The most common ones are the D_0 , D^\pm and D_s^\pm mesons, along with the Λ_c^\pm baryons. The energy spectra are shown in Figure 6.9, from a Monte Carlo simulation of charm pairs produced in a CHARM1 configuration.

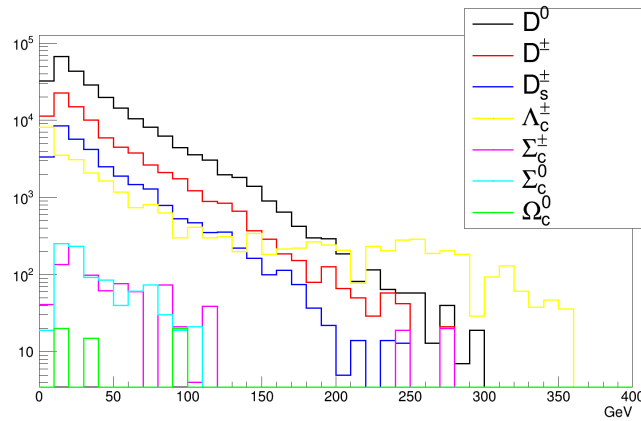


Figure 6.9: Energy spectra of simulated charmed hadrons, from a beam of 400 GeV protons.

The accurate prediction of charm hadroproduction rates is an essential ingredient to establish the sensitivity of the SHiP experiment, to detect new particles possibly produced in charm decays and to make a precision estimate of the tau neutrino yield.

The topology of an associated charm production in an ECC target features three vertices: the most upstream (referred to as “primary vertex”) is the inelastic hadronic interaction producing the charmed hadrons, coming from the primary 400 GeV proton or a less energetic hadron. The identification of this vertex topology has been described in the previous section. The complete event reconstruction requires to separate both decay vertices (referred to as “secondary vertices”) from the primary interaction, thus

providing two charmed hadron candidates connecting them. Background from pion and electromagnetic interactions, along with random track combinations in the area near the proton interaction, need to be rejected, providing clear signal identification.

Particle	Mass	$c\tau$
D^0	1.86 GeV	123 μm
D^\pm	1.87 GeV	312 μm
D_s^\pm	1.97 GeV	151 μm
λ_c^\pm	2.29 GeV	61 μm

Table 6.2: Known properties of the most frequent charmed hadrons expected in SHiP-charm data. Values from Particle Data Group 2020 [53].

The charm production vertex is followed by two decay vertices, one for each of the two produced charmed hadrons. At SHiP-charm energies, the flight length amounts to a few millimeters. The decay is classified as short if it happened before the particle could traverse an emulsion film, otherwise it is classified as long (Figure 6.10). The latter amount to $\sim 70\%$ of charmed hadron decays.

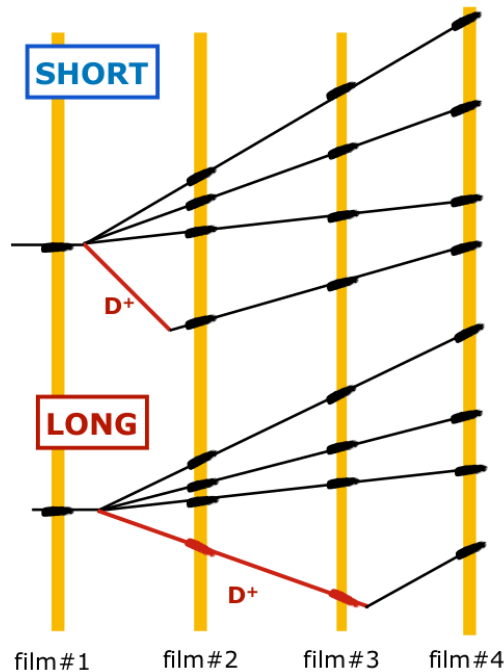


Figure 6.10: Drawing showing the definitions of “short” (top) and “long” decay (bottom) in an Emulsion Cloud Chamber.

6.3.2 Decay search procedure

The event selection procedure starts by looking for the inelastic hadronic interaction producing the pair of charmed hadrons, within a **fiducial volume** ending 3.9 mm before the end of the ECC target. The interaction vertex needs first to have been reconstructed (**Primary vertex visibility**), then it has to be recognized by the BDT primary vertex identification described in section 6.2.1 (**Primary vertex identification**).

The analysis presented here focuses on a long charged charmed hadron's decay, which presents a clearer topology. The search is performed in a 55 mm^3 volume around the recognized interaction vertex (**Secondary vertex visibility**). Decay candidates are separated from background interactions by a second BDT classifier, acting on the following variables (Figure 6.11) computed for all tracks associated to the vertex:

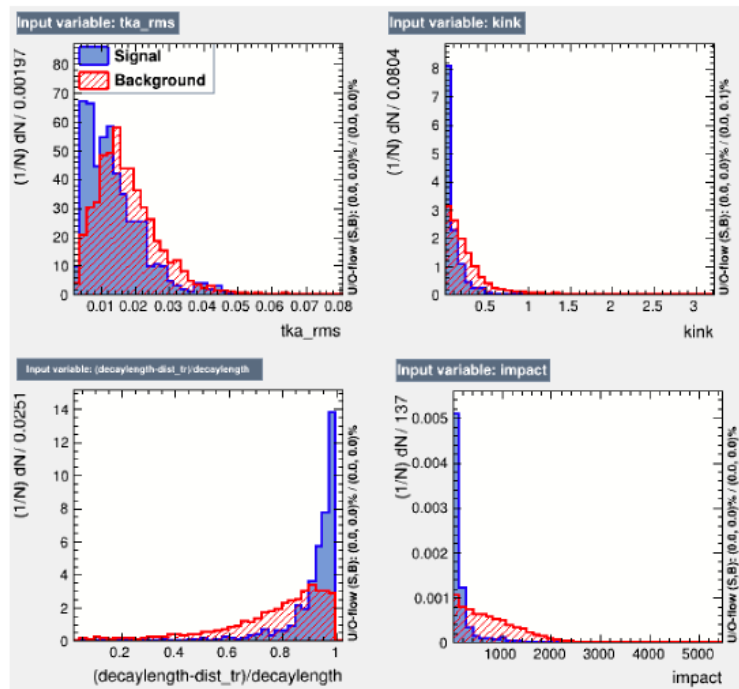


Figure 6.11: Variables for BDT classification of decay vertices. Shown for signal (in blue) and background (in red). Spatial units are μm .

- **Kink angle** between the daughter track and the line connecting the interaction vertex with the candidate decay vertex;
- **Root Mean Square (RMS) of angle differences** between all the segments belonging to the same track. A sudden large angle variation is

hint of a in-track kink;

- **Impact parameter** of the track with respect to the primary vertex. This should be compatible with the $c\tau$ of a charmed hadron decay;
- **Transverse distance** between the interaction vertex and the candidate decay vertex.

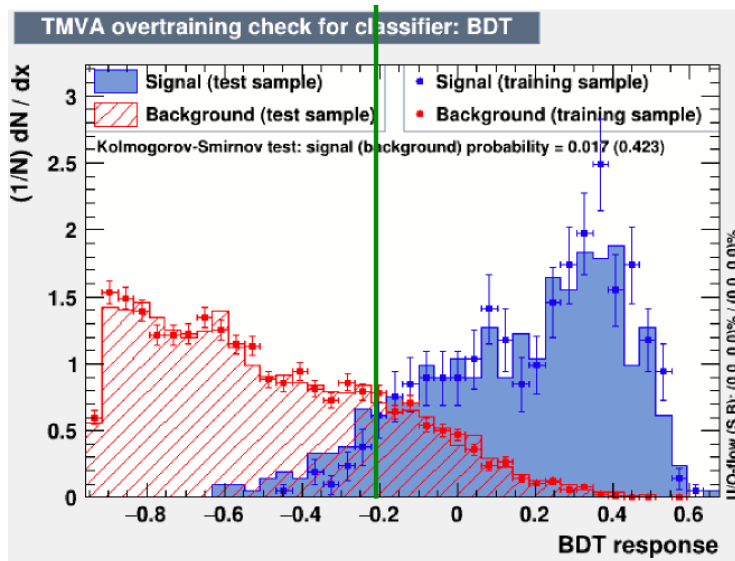


Figure 6.12: Output of BDT classification of decay vertices. Shown for signal (in blue) and background (in red). The green line shows the applied selection at $BDT_{min} = -0.2$.

The output of the **decay search** BDT classifier for signal and background vertices is reported in Figure 6.12, the decay is accepted if the output of the BDT is larger than $BDT_{min} = -0.2$. If a single decay is found, a second V_0 decay vertex is searched for in the same volume, in order to find a candidate for another charmed hadron decay. When also this search provides a candidate decay vertex, the overall event is accepted as a double charm production event.

The selection efficiency has been estimated from a sample of 2500 Monte Carlo simulated events in the CHARM1-RUN6 configuration. The obtained values from each step, starting from the identification of the primary hadron interaction vertex and ending with the decay search, are reported in Table 6.3. The application of the same selection to a sample of 106412 background vertices resulted in 787 candidates.

Selection	Signal events	Efficiency
Fiducial volume	2230	$(89.2 \pm 0.6)\%$
1ry vertex visibility	1911	$(76.4 \pm 0.8)\%$
1ry vertex identification	1745	$(69.8 \pm 0.9)\%$
2ry vertex visibility	1187	$(47.5 \pm 1.0)\%$
Decay search	584	$(23.4 \pm 0.8)\%$

Table 6.3: Number of signal events and efficiency at each selection, as estimated from Monte Carlo simulations.

However, the current selection leads to a prediction of 4.4 signal events detected in CHARM1-RUN6 data, over a background of 2072 events, resulting in a noise/signal ratio of 480. Further rejection requires the momentum measurement of the decay daughters.

Example of candidates

As reference, an event of associated charm production is described here, from the CHARM1-RUN6 dataset. This event has passed all the selection steps described in the previous sections. The display is shown in Figure 6.13.

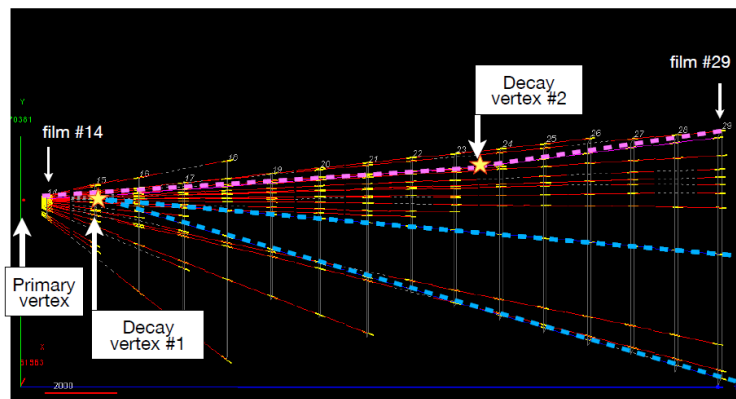


Figure 6.13: Display of double charm candidate from CHARM1-RUN6 data.

In this run configuration, protons impinge directly on the target, without any passive material upstream. A total of 29 nuclear emulsion films compose the ECC brick. The primary vertex was detected in the center of the target, in the passive layer upstream of film 14. A total of 31 tracks has been associated to this vertex. A charged particle decays after 12.7 mm from the primary vertex, as seen by a clear kink of 31 mrad. This topol-

ogy is compatible with a 1 prong decay of a high-energy charged charmed hadron. In addition, a V0-like decay is observed at a distance of 2.1 mm from the primary vertex. The two associated tracks have an impact parameter of $594 \mu\text{m}$ and $253 \mu\text{m}$ with respect to the primary vertex. From the measured flight length and average decay angle, one can infer an estimate of the particle lifetime [92], therefore its $c\tau$: this gives $420 \mu\text{m}$ for the neutral particle and $390 \mu\text{m}$ for the charged one.

6.3.3 Momentum measurement through Multiple Coulomb Scattering

Even after the BDT and decay search selections, topological requirements alone are not enough to reduce the background to signal levels, without further spoiling the signal efficiency to zero events. Full reconstruction of the event is therefore needed, with the addition of kinematic data about charm decay daughters. Momentum measurement in the Emulsion Cloud Chamber can be performed by employing Multiple Coulomb Scattering of the charged particles traversing it.

A charged particle traversing a medium of radiation length X_0 is affected by many small-angle deflections, mostly due to Coulomb scattering from nuclei. The central limit theorem asserts that the resulting angular distribution from this Multiple Coulomb Scattering is a Gaussian, with sigma θ_0 given by Lynch-Dahl formula [93]:

$$\theta_0 = \frac{13.6 \text{ MeV}}{\beta c p} z \sqrt{\frac{x}{X_0}} \left[1 + 0.038 \ln \left(\frac{x z^2}{X_0 \beta^2} \right) \right], \quad (6.8)$$

where p , βc and z are the momentum, velocity and charge number of the incident particle, and $\frac{x}{X_0}$ is the thickness of the scattering medium in radiation lengths.

Momentum of a particle in a ECC chamber can be then measured from the angular differences of the detected base-tracks between pairs of emulsion films. The scattering is dominated by the passive blocks between the films, since the radiation length in the emulsion layers and in the plastic base is larger by more than one order of magnitude. Defining the number of cells crossed by a particle track N^{cell} and the distance traversed in each cell Δx^{cell} (depending on the track angle), the above-mentioned expression becomes:

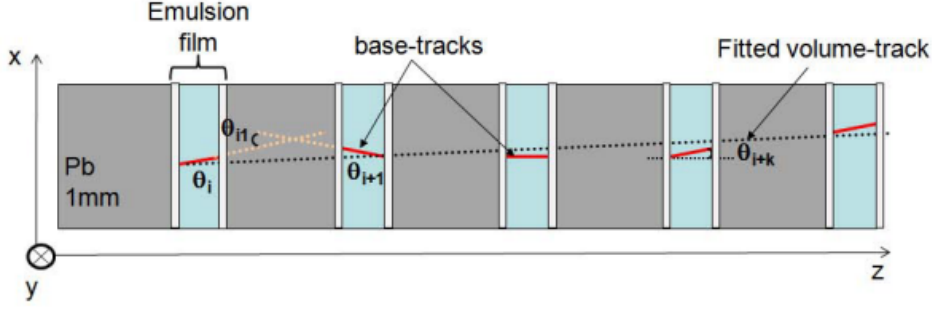


Figure 6.14: Measurement of multiple scattering from the angles of base-tracks in nuclear emulsion films [94].

$$\theta_0 \simeq \frac{13.6 \text{ MeV}}{\beta c p} \sqrt{\frac{N^{cell} \Delta x^{cell}}{X_0}} \left[1 + 0.038 \ln \left(\frac{N^{cell} \Delta x^{cell}}{X_0} \right) \right]. \quad (6.9)$$

Assuming a given cell depth $N^{cell} = k$, the difference between the base-track angles in the i th emulsion film and after k films is $\theta_{ik} = \theta_{i+k} - \theta_i$. Therefore, the variance of the scattering angle distribution is computed as

$$\langle \theta_{meas}^2 \rangle_k = \sum_i \frac{(\theta_{ik})^2}{N_{meas}} = \theta_0^2 + \delta\theta^2, \quad (6.10)$$

where $\delta\theta$ is the angular resolution of the emulsions. Finally, track momentum p is determined from a fit of θ_{meas} on the number of crossed planes, treating p as a free parameter and fixing the resolution. The angular resolution of the emulsions allow the determination of charged particle momenta from several hundreds of MeV/c to a few GeV/c, as demonstrated by the OPERA experiment [94].

This algorithm has been applied to the Monte Carlo simulation, for the sample of charged daughters of charmed hadrons, passing the decay search selections and having momentum less than 5 GeV/c. The relative momentum resolution $(P_{rec} - P_{true})/P_{true}$ is shown in Figure 6.15, as estimated from MC particles with momentum less than 5 GeV/c. A resolution of $\sim 30\%$ can be achieved.

6.4 Conclusions

The optimization run of SHiP-charm has been performed in 2018, collecting 1.56×10^6 protons on target. The proton beam has been provided through

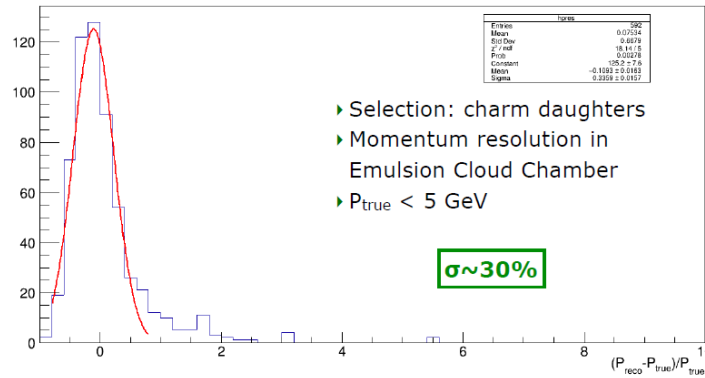


Figure 6.15: Momentum resolution of MCS measurement in ECC, for $P < 5 \text{ GeV}/c$. Tracks are daughters of charmed hadrons from CHARM1 simulation.

spills from the SPS accelerator, each lasting 4.8 s and intensity between 7.7×10^3 and 13.8×10^3 protons per spill. The high intensity has provided a challenging environment for all subdetectors, in particular in the region upstream of the Goliath magnet. The two subdetectors located there, the pixel telescope and the Emulsion Cloud Chamber, performed as expected during both data collection and analysis.

The analysis of the data in the nuclear emulsion films has started with the reconstruction of proton interactions, which have been separated from the background of fake combinations and other particles. Proton interaction vertices have been reconstructed for all six target configurations, and the data analysis is moving to the charmed hadron decays as planned. The low number of events and the high surrounding background makes decay search challenging, and topological features from emulsion data alone are not enough for a clear event identification. The addition of momentum information is thus required, with the measurement from multiple coulomb scattering and the addition of data from downstream detectors.

Alignment between the moving Emulsion Cloud Chamber and the static pixel telescope has been successfully performed. Tracks from both subdetectors have been matched, starting the global track reconstruction in the whole experimental apparatus. An event display is shown in Figure 6.16. Unfortunately, matching with the downstream detectors has been affected by a readout malfunctioning in the SciFi system, impending data acquisition in this run. Matching of the data between pixel and the other detectors

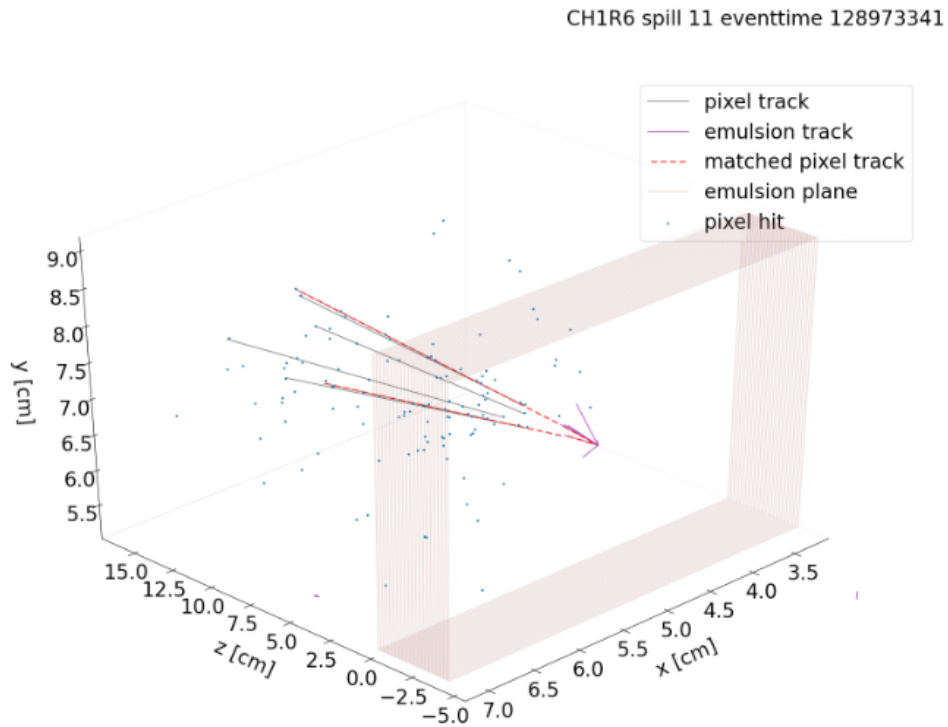


Figure 6.16: Display of a matched event in SHiP-charm. Tracks reconstructed in the ECC are marked purple, tracks reconstructed in the pixel detector are gray and matched tracks are marked with the dashed red line [91].

is under study.

The results from the proton interactions and the matching are being submitted in scientific papers. Both the design of the experimental apparatus and the data analysis chain will then be finalized for the full SHiP-charm run. The time schedule is under preparation, as it will follow the SND@LHC planned during LHC RUN3 next year. This experiment will provide another application of emulsion reconstruction techniques in a high intensity neutrino detector.

Conclusions

SHiP (Search for Hidden Particles) is a new general purpose experiment, aimed at searching for Beyond the Standard Model physics in the high intensity frontier. A new beam dump facility has been proposed at the CERN SPS accelerator, allowing for a clear environment, suitable also for neutrino detection. The Scattering and Neutrino Detector (SND), placed in the middle of the SHiP apparatus, can detect a high number of neutrino interactions, leading to interesting studies of neutrino physics. It can also be employed for the search of light dark matter scattering.

During my three years of Ph.D., I have studied tau neutrino simulations in the SHiP apparatus, to evaluate the performance of the SND. This detector uses the Emulsion Cloud Chamber (ECC) brick as the fundamental component, employing nuclear emulsion films to reconstruct the neutrino interaction vertex and the decay vertex of the associated tau lepton. The detection efficiency amounts to $(27.6 \pm 0.5)\%$ in the muon decay channel of the associated tau lepton. The main background source are neutrino-induced charm events, since the short life of the charmed hadrons leads to a similar decay topology for a fraction $(10.6 \pm 0.2)\%$ of the events. However, the estimated signal-noise ratio remains less than 1, requiring further background discrimination by exploiting different kinematic features, such as the phi angle between the primary lepton and the hadronic jet. Including this variable in the event reconstruction requirements results in an increase of the signal-noise ratio to 1.5.

I have also tested the emulsion reconstruction framework with data from test beams dedicated to critical points. Electromagnetic shower reconstruction is needed to identify charged interactions of electron neutrinos and to provide energy measurement. It can be achieved by employing the ECC bricks as sampling calorimeters, estimating the energy from the number of tracks associated to the shower. However, the classical cone reconstruction software from the OPERA experiment does not comply well with

the high intensity planned for the SHiP experiment. A novel alternative based on Machine Learning has been proposed and tested with electron beams at DESY in 2019. The new algorithm allows for a larger purity of $(86.5 \pm 0.5)\%$, with respect to $(78.1 \pm 1.0)\%$ from the classical one, without loss in efficiency. The energy resolution has been estimated to be $(25 \pm 1)\%$ for showers of 6 GeV energy from Monte Carlo simulations.

The vertex reconstruction, instead, has been tested in a high intensity environment from the optimization run for a charm cross section measurement. This run has been performed at CERN SPS in 2018, providing ECC bricks exposed from 400 GeV protons at different intensities. The data analysis has led to a measurement of the proton interaction length in the ECC lead/emulsion bricks, amounting to (182^{+19}_{-16}) mm. At the same time, the challenges and experimental requirements for the identification of associated charm events have been studied, opening room for improvements in future runs.

In conclusion, my thesis has provided a comprehensive study of the challenges in emulsion data reconstruction, updated to current techniques and technologies. The acquired experience will be essential for the analysis of large future projects at CERN involving emulsions. As the preparation of the SHiP experiment continues, the nearest project will be the detection of neutrinos from the LHC collider. This experiment employs a similar SND detector as the one designed for SHiP, and it is therefore referred to as SND@LHC. It will start taking data at LHC RUN3, from 2022 onwards.

Appendix A

List of ECC configurations for SHiP-charm optimization run

The optimization run for the charm measurement has been performed in 2018. 24 ECC bricks have been employed, grouped in 6 different configurations (usually referred to as CHARM1 - CHARM6). Half of the targets has been exposed to 10 proton spills (spaced of 1 cm along the y axis), while the other half has been exposed to 5 spills (spaced of 2 cm along the y axis).

Nuclear emulsions have been provided by Nagoya University and Slavich company. The provenience of the films employed in each brick is reported.

A.1 CHARM1 configuration

RUN NAME	Emulsion Provenience	N Spills	Total number of p.o.t.
CHARM1-RUN1	Nagoya	10	136270
CHARM1-RUN2	Nagoya	10	110352
CHARM1-RUN3	Slavich	10	107442
CHARM1-RUN4	Slavich	10	76307
CHARM1-RUN5	Slavich	10	73575
CHARM1-RUN6	Slavich	5	38892

Table A.1: Exposure details for CHARM1 target bricks.

The first configuration employs the smallest proton target, fully instrumented as an Emulsion Cloud Chamber. Each brick presents 29 emulsion films, interleaved by 28 passive blocks. One brick, CHARM1-RUN6, employs tungsten instead of lead as passive material, in order to replicate the

planned composition of the SHiP SND bricks. The thickness of tungsten slabs is 0.9 mm (instead of 1.0 mm-thick lead slabs).

A.2 CHARM2 configuration

The second configuration is still a single target block, but only the downstream section is instrumented as an ECC detector, which follows 28 mm of completely passive lead. The ECC detector itself maintains the composition of the CHARM1 configuration: 29 emulsion films interleaved by 28 passive layers.

RUN NAME	Emulsion Provenience	N Spills	Total number of p.o.t.
CHARM2-RUN1	Nagoya	10	132415
CHARM2-RUN2	Nagoya	5	35763
CHARM2-RUN3	Slavich	5	38853
CHARM2-RUN4	Slavich	5	43131
CHARM2-RUN5	Slavich	10	143988
CHARM2-RUN6	Slavich	10	123288

Table A.2: Exposure details for CHARM2 target bricks.

A.3 CHARM3 configuration

The third configuration introduces the “pre-shower” target blocks: A completely passive 56 mm lead block is placed ~ 3 cm upstream of the emulsion detector. From this configuration and in all the others, the ECC brick employs 57 emulsion films, interleaved by 56 passive layers, doubling the amount of passive material in the chamber.

RUN NAME	Emulsion Provenience	N Spills	Total number of p.o.t.
CHARM3-RUN1	Nagoya	5	29586
CHARM3-RUN2	Slavich	5	38839
CHARM3-RUN3	Slavich	5	34027

Table A.3: Exposure details for CHARM3 target bricks.

A.4 CHARM4 configuration

The fourth configuration employs a “pre-shower” of 2 lead blocks, each of them 56 mm-thick. The ECC brick employs 57 emulsion films, interleaved by 56 passive layers.

RUN NAME	Emulsion Provenience	N Spills	Total number of p.o.t.
CHARM4-RUN1	Nagoya	5	24578
CHARM4-RUN2	Slavich	5	26661
CHARM4-RUN3	Slavich	5	26160

Table A.4: Exposure details for CHARM4 target bricks.

A.5 CHARM5 configuration

The fifth configuration employs a “pre-shower” of 3 lead blocks, each of them 56 mm-thick. The ECC brick employs 57 emulsion films, interleaved by 56 passive layers.

RUN NAME	Emulsion Provenience	N Spills	Total number of p.o.t.
CHARM5-RUN1	Nagoya	5	25593
CHARM5-RUN2	Slavich	5	34030
CHARM5-RUN3	Slavich	10	98436

Table A.5: Exposure details for CHARM5 target bricks.

A.6 CHARM6 configuration

The sixth configuration employs a “pre-shower” of 4 lead blocks, each of them 56 mm-thick. The ECC brick employs 57 emulsion films, interleaved by 56 passive layers.

RUN NAME	Emulsion Provenience	N Spills	Total number of p.o.t.
CHARM6-RUN1	Nagoya	5	20443
CHARM6-RUN2	Slavich	5	17123
CHARM6-RUN3	Slavich	10	119894

Table A.6: Exposure details for CHARM6 target bricks.

Bibliography

- [1] G. Aad et al. *Observation of a new particle in the search for the Standard Model Higgs boson with the ATLAS detector at the LHC. Phys. Lett., B716*, pp. 1-29, (2012).
- [2] S. Chatrchyan et al. *Observation of a new boson at a mass of 125 GeV with the CMS experiment at the LHC. Phys. Lett., B716*, pp. 30-61, (2012).
- [3] R. Alemany et al. *Summary Report of Physics Beyond Colliders at CERN. CERN-PBC-REPORT-2018-003*, (2018).
- [4] A. Abada et al. (FCC Collaboration). *Future Circular Collider Study. Volume 1: Physics Opportunities. Conceptual Design Report. Eur. Phys. J. C, 79* 6, 474, (2019).
- [5] S. Alekhin et al. (SHiP Collaboration). *A facility to search for hidden particles at the CERN SPS: the SHiP physics case. Rep. Prog. Phys., 79* 124201, (2016).
- [6] F. Bezrukov and D. Gorbunov. *Light inflaton after LHC8 and WMAP9 results. JHEP, 140*, (2013).
- [7] M. Deliyergiyev. *Recent Progress in Search for Dark Sector Signatures. Open Phys., 14*, (2016).
- [8] Esma Mobs. *The CERN accelerator complex - August 2018. Complexe des accélérateurs du CERN - Août 2018. CDS, General Photo, url = <https://cds.cern.ch/record/2636343>*.
- [9] N. Agafonova et al. (OPERA Collaboration). *Final Results of the OPERA Experiment on ν_τ Appearance in the CNGS Neutrino Beam. Phys. Rev. Lett., 120*, 211801, (2018).

- [10] M. Antonello et al. *Operation and performance of the ICARUS T600 cryogenic plant at Gran Sasso underground Laboratory*. *JINST*, **10** P12004, (2015).
- [11] C.Gatto (on behalf of REDTOP Collaboration). *The REDTOP experiment*. arXiv:1910.08505.
- [12] NA62 Collaboration. *2020 NA62 Status Report to the CERN SPSC*. CERN-SPSC-2020-007 / SPSC-SR-266.
- [13] NA64 Collaboration. *Prospects for exploring the Dark Sector physics and rare processes with NA64 at the CERN SPS*. Input to the Particle Physics Strategy Update, (2018).
- [14] W. Bartmann et al. *AWAKE++: the AWAKE Acceleration Scheme for New Particle Physics Experiments at CERN*. Input to the Particle Physics Strategy Update, (2018).
- [15] M.Anelli et al. (SHiP Collaboration). *A facility to Search for Hidden Particles (SHiP) at the CERN SPS*. CERN-SPSC-2015-016, SPSC-P-350.
- [16] G. Aielli et al. *Expression of Interest for the CODEX-b Detector*. *Eur. Phys. J. C*, **80**, (2020).
- [17] A. Ariga et al. FASER Collaboration. *FASER: ForwArd Search ExpeRiment at the LHC*. UCI-TR-2019-01, KYUSHU-RCAPP-2018-08.
- [18] C. Alpigiani et al. (MATHUSLA Collaboration). *A Letter of Intent for MATHUSLA: a dedicated displaced vertex detector above ATLAS or CMS*. CERN-LHCC-2018-025, LHCC-I-031.
- [19] W. Pauli. *Open letter to radioactive ladies and gentlemen (1930)*. *Phys. Today*, **31** 27, (1978).
- [20] C.A. Argüelles et al. *White Paper on New Opportunities at the Next-Generation Neutrino Experiments (Part 1: BSM Neutrino Physics and Dark Matter)*. FERMILAB-FN-1079-T, (2019).
- [21] M. G. Aartsen et al (IceCube Collaboration). *Measurement of the Multi-TeV Neutrino Cross Section with IceCube Using Earth Absorption*. *Nature*, **551**, (2017).

- [22] N Beni et al. *Physics potential of an experiment using LHC neutrinos*. *J. Phys. G: Nucl. Part. Phys.*, **46** 115008, (2019).
- [23] H. Abreu et al. (FASER Collaboration). *Technical Proposal: FASERnu*. CERN-LHCC-2019-017, (2020).
- [24] SND Collaboration. *SND@LHC - Scattering and Neutrino Detector at the LHC*. CERN-LHCC-2021-003 ; LHCC-P-016, (2021).
- [25] M. Bustamante and A. Connolly. *Extracting the energy-dependent neutrino-nucleon cross section above 10 tev using icecube showers*. *Phys. Rev. Lett.*, **122** 041101, (2019).
- [26] K. Kodama et al. *Final tau-neutrino results from the DONuT experiment*. *Phys. Rev. D - Particles, Fields, Gravitation and Cosmology*, **78**, pp. 1-20, (2008).
- [27] C. Albright and C. Jarlskog. *Neutrino production of M^+ and E^+ heavy leptons (I)*. *Nuc. Phys. B*, **84**, pp. 467-492, (1975).
- [28] M. Reno. *Electromagnetic structure functions and neutrino nucleon scattering*. *Phys. Rev.*, **D74**, 033001, (2006).
- [29] V.A. Bednyakov et al. *Neutrino physics and JINR*. *Phys.-Usp.*, **59**, 225, (2016).
- [30] A.G. Beda et al. *Gemma experiment: The results of neutrino magnetic moment search*. *Phys. Part. Nuclei Lett.*, **10** 139, (2013).
- [31] L.B. Auerbach et al. (LSND Collab.). *Measurement of electron-neutrino electron elastic scattering*. *Phys. Rev. D*, **63** 112001, (2001).
- [32] R. Schwienhorst et al. *A new upper limit for the tau-neutrino magnetic moment*. *Phys. Lett. B*, **513** 23-29, (2001).
- [33] G. Domogatsky and D. Nadezhin. *Modern theory of star evolution and experiments of f. reines on antineutrino-electron scattering detection*. *Yad.Fiz.*, **12** 1233–1242, (1970).
- [34] G. Radel and R. Beyer. *Neutrino electron scattering*. *Mod.Phys.Lett.*, **A8** 1067–1088, (1993).

- [35] A. Benvenuti et al. *Observation of New-Particle Production by High-Energy Neutrinos and Antineutrinos*. *Phys. Rev. Lett.*, **34** 419-422, (1975).
- [36] G. De Lellis, A. M. Guler, J. Kawada, U. Kose, O. Sato, and F. Tramontano. *Search for charmed pentaquarks in high energy anti-neutrino interactions*. *Nucl. Phys.*, **B763** 268-282, (2007).
- [37] R. Aaij et al. (LHCb Collaboration). *Observation of a Narrow Pentaquark State, $P_c(4312)^+$, and of the Two-Peak Structure of the $P_c(4450)^+$* . *Phys. Rev. Lett.*, **122** 222001, (2019).
- [38] C. Ahdida et al. (SHiP Collaboration). *SHiP Experiment. Comprehensive Design Study Report*. CERN-SPSC-2019-049/SPSC-SR-263, (2019).
- [39] C. Ahdida et al. (SHiP Collaboration). *SHiP Experiment. Progress Report*. CERN-SPSC-2019-010/SPSC-SR-248, (2019).
- [40] C. Ahdida et al. (SHiP Collaboration). *The experimental facility for the Search for Hidden Particles at the CERN SPS*. *JINST*, **14** P03025, (2019).
- [41] M. Calviani, B. Goddard, R. Jacobsson, and M. Lamont (eds.). *SPS Beam Dump Facility : Comprehensive Design Study*. CERN Yellow Reports: Monographs, cern-2020-002 edition, (2020).
- [42] E. Lopez Sola and M. Calviani et al. *Design of a high power production target for the beam dump facility at CERN*. *Phys. Rev. Accel. Beams*, **22** 113001, (2019).
- [43] G. Battistoni, T. Boehlen, F. Cerutti, P.W. Chin, A. Fassò L.S. Esposito, A. Ferrari, A. Lechner, A. Empl, A. Mairani, P. Garcia Ortega A. Mereghetti, J. Ranft, S. Roesler, P.R. Sala, V. Vlachoudis, and G. Smirnov. *Overview of the FLUKA code*. *Annals of Nuclear Energy*, **82** 10-18, (2015).
- [44] T.T. Bohlen, F. Cerutti, M.P.W. Chin, A. Fassò, A. Ferrari, P.G. Ortega, A. Mairani, P.R. Sala, G. Smirnov, and V. Vlachoudis. *The FLUKA Code: Developments and Challenges for High Energy and Medical Applications*. *Nuclear Data Sheets*, **120** 211-214, (2014).
- [45] A.Akmete et al. (SHiP Collaboration). *The active muon shield in the SHiP experiment*. *JINST*, **12** P05011, (2017).

- [46] Kunihiro Morishima, Akira Nishio, Masaki Moto, Toshiyuki Nakano, and Mitsuhiro Nakamura. *Development of nuclear emulsions for muography*. *Annals of Geophysics*, **60**, 1, S0112, (2017).
- [47] C. Ahdida et al. (SHiP Collaboration). *The magnet of the scattering and neutrino detector for the SHiP experiment at CERN*. *JINST*, **15** P01027, (2020).
- [48] O. Lantwin. *Optimisation of the SHiP experimental design*. PhD Thesis, Imperial College London, CERN-THESIS-2019-157.
- [49] T. Alexopoulos et al. *Development of large size Micromegas detector for the upgrade of the ATLAS muon system*. *Nucl. Instrum. Meth.*, **A617** 161–165, (2010).
- [50] The SHiP Collaboration. *Sensitivity of the SHiP experiment to Heavy Neutral Leptons*. *JHEP*, **04** 077, (2019).
- [51] M. Al-Turany, D. Bertini, R. Karabowicz, D. Kresan, P. Malzacher, and T. Stockmanns et al. *The FairRoot framework*. *J. Phys. Conf. Ser.*, **396** 022001, (2012).
- [52] R. Maciuła, A. Szczurek, J. Zaremba, and I. Babiarcz. *Production asymmetry of ν_τ neutrinos and $\bar{\nu}_\tau$ antineutrinos from a fixed target experiment SHiP*. *Institute of Nuclear Physics, Polish Academy of Sciences, ul. Radzikowskiego*, **152**, PL-31-342.
- [53] P. A. Zyla et al. *Particle Data Group*. *Prog. Theor. Exp. Phys.*, **2020** 083C01, (2020).
- [54] H. Dijkstra and T. Ruf. *Heavy Flavour Cascade Production in a Beam Dump*. *SHiP-Note-2015-009*.
- [55] Torbjorn Sjostrand (Lund University), Stephen Mrenna (Fermilab), and Peter Skands (Fermilab). *Pythia 6.4 Physics and Manual*. *FERMILAB-PUB-06-052-CD-T*.
- [56] C. Andreopoulos et al. *The GENIE Neutrino Monte Carlo Generator*. *Nucl. Instrum. Meth. A*, **614** 87-104, (2010).
- [57] D. Centanni. *Performance and optimisation of the Scattering and Neutrino Detector of the SHiP experiment*. CERN-THESIS-2020-289.

- [58] Costas Andreopoulos, Christopher Barry, Steve Dytman, Hugh Gallagher, Tomasz Golan, Robert Hatcher, Gabriel Perdue, and Julia Yarba. *The GENIE Neutrino Monte Carlo Generator: Physics and User Manual*. *arXiv:1510.05494* (2015).
- [59] J.Allison et al. *Recent developments in Geant4*. *Nucl. Instrum. Methods Phys. Res. A* **835** 186-225, (2016).
- [60] N. Agafonova et al. (OPERA Collaboration). *New results on $\nu_\mu \rightarrow \nu_\tau$ appearance with the OPERA experiment in the CNGS beam*. *JHEP*, **36**, (2013).
- [61] D.Barney. *Calorimetry in Particle Physics, and the CMS High-Granularity Calorimeter*. *JINST*, **15** C07018, (2020).
- [62] R. Diener, J. Dreyling-Eschweiler, H. Ehrlichmann, I.M. Gregor, U. Kötzt, U. Krämer, N. Meyners, N. Potylitsina-Kube, A. Schütz, P. Schütze, and M. Stanitzki. *The DESY II test beam facility*. *NIMA*, **922** 265-286, (2019).
- [63] M. Hartmann. *Study of a Scintillating Fibre Tracker using DESY testbeam data*. *LHPE reports*, (2019).
- [64] L.Arrabito et al. *Track reconstruction in the emulsion-lead target of the OPERA experiment using the ESS microscope*. *JINST*, **2** P05004, (2007).
- [65] A. Alexandrov et al. *A new generation scanning system for the high-speed analysis of nuclear emulsions*. *JINST*, **11** P06002, (2016).
- [66] A. Alexandrov et al. *The continuous motion technique for a new generation of scanning systems*. *Scientific reports*, **7**, (2017).
- [67] L. Arrabito et al. *Electron/pion separation with an Emulsion Cloud Chamber by using a Neural Network*. *JINST*, **2** P02001, (2007).
- [68] S.Shirobokov, A.Filatov, V.Belavin, and A.Ustyuzhanin. *Machine Learning for electromagnetic showers reconstruction in emulsion cloud chambers*. *J. Phys.: Conf. Ser.* **1085** 042025, (2018).
- [69] M. De Luca. *Electron identification in the Emulsion detector of SHiP experiment using machine learning techniques*. CERN-THESIS-2021-009.
- [70] L. Breiman. *Random Forests*. *Machine Learning*, **45**, 5-32, (2001).

- [71] F. Pedregosa et al. *Scikit-learn: Machine Learning in Python*. *Journal of Machine Learning Research*, **12**:2825–2830, (2011).
- [72] A. Hoecker et al. *TMVA - Toolkit for Multivariate Data Analysis*. CERN-OPEN-2007-007, (2007).
- [73] Christian Wolfgang Fabjan and Herwig Schopper, editors. *Particle Physics Reference Library: Volume 2: Detectors for Particles and Radiation*. Springer Nature, Cham, (2020).
- [74] N. Cabibbo. *Unitary Symmetry and Leptonic Decays*. *Phys. Rev. Lett.*, **10** 531, (1963).
- [75] S. L. Glashow, J. Iliopoulos, and L. Maiani. *Weak Interactions with Lepton-Hadron Symmetry*. *Phys. Rev. D*, **2** 1285, (1970).
- [76] M. Kaplon, B. Peters, and D. M. Ritson. *Emulsion cloud-chamber study of a high energy interaction in the cosmic radiation*. *Phys. Rev.*, **85** 900-903, (1952).
- [77] K.Niu. *Discovery of naked charm particles and lifetime differences among charm species using nuclear emulsion techniques innovated in Japan*. *Proc. Jpn. Acad., Ser.B* **84**, (2008).
- [78] K.Niu, E. Mikumo, and Y. Maeda. *A Possible Decay in Flight of a New Type Particle*. *Prog. Theor. Phys.*, **46** 1644, (1971).
- [79] J. E. Augustin and others (SLAC-SP-017 Collaboration). *Discovery of a Narrow Resonance in e^+e^- Annihilation*. *Phys. Rev. Lett.*, **33** 1406, (1974).
- [80] P. Nason. *Introduction to perturbative QCD. Particles and fields. Proceedings, 11th Jorge Andre Swieca Summer School, Campos do Jordao, Sao Paulo, Brazil, January 14-27, (2001)*.
- [81] The SHiP Collaboration. *Measurement of associated charm production induced by 400 GeV/c protons*. CERN-SPSC-2017-033 / SPSC-EOI-017, 2017.
- [82] M. Aguilar-Benitez et al. (LEBC-EHS Collaboration). *Charm Hadron Properties in 400-GeV/c $p p$ Interactions*. *Z.Phys.C*, **40** 321, (1988).
- [83] ATLAS IBL Collaboration. *Prototype ATLAS IBL Modules using the FE-I4A Front- 684 End Readout Chip*. *JINST*, **7** P11010, (2012).

- [84] SHiP Collaboration Ahdida, C. et al. *Measurement of the muon flux from 400 GeV/c protons interacting in a thick molybdenum/tungsten target.* *Eur. Phys. J. C*, **80** 284, (2020).
- [85] L. Congedo. *RPC and readout system for the neutrino detector of the SHiP experiment.* *JINST*, **15** C09014, (2020).
- [86] E791 Collaboration. *Total forward and differential cross sections of neutral D mesons produced in 500 GeV/c π^- -nucleon interactions.* *Phys.Lett.B*, **462**, (1999).
- [87] M. Rosenthal, N. Charitonidis, P. Chatzidaki, R. Margraf, H. Wilkens, F. Bergsma, and P. A. Giudici. *Magnetic Field Measurements of the GO-LIATH Magnet in EHN1.* CERN-ACC-NOTE-2018-0028, (2018).
- [88] V. Tioukov, I. Kreslo, Y. Petukhov, and G. Sirri. *The FEDRA — Framework for emulsion data reconstruction and analysis in the OPERA experiment.* *Nucl. Instrum. Methods Phys. Res., A* **559** 103-105, (2006).
- [89] Y. Freund and R.E. Schapire. *A Decision-Theoretic Generalization of On-Line Learning and an Application to Boosting.* *J. of Computer and System Science*, **55**, 119, (1997).
- [90] C. Ahdida et al. *Reconstruction of 400 GeV/c proton interactions with the SHiP-charm project.* CERN-SHiP-NOTE-2020-002.
- [91] C. Ahdida et al. *Track reconstruction and matching for SHiP-charm.* CERN-SHiP-NOTE-2020-003.
- [92] S. Petrera and G. Romano. *A method to evaluate the detection efficiency and the mean lifetime of short-lived particles.* *Nucl. Instrum. Meth.*, **174** 61-65, (1980).
- [93] G. R. Lynch and O. I. Dahl. *Approximations to multiple Coulomb scattering.* *Nucl. Instrum. Meth.*, **B58** 6, (1991).
- [94] OPERA Collaboration N. Agafonova et al. *Momentum measurement by the Multiple Coulomb scattering method in the OPERA lead emulsion target.* *New J. Phys.*, **14** 013026, (2012).

List of Figures

1.1	Current frontiers of new physics: the energy frontier, looking for particles with heavy masses and the intensity frontier, looking for weak couplings.	9
1.2	Scattering of a dark matter candidate χ with an SM electron, through the exchange of a mixed $\gamma - A'$ propagator.	10
1.3	Decay properties of a dark scalar in function of its mass m_S . On the left: predicted decay branching ratios. On the right: scalar lifetime as a function of its mass m_S for constant mixing angle with the Higgs boson, $\theta^2 = 10^{-6}$. From the SHiP physics proposal [5], reproduced from [6].	12
1.4	Decay diagram of a sterile neutrino $N_{2,3}$ into a muon and a pion.	12
1.5	Complementary Dark Matter (DM) research procedures: direct searches, looking for nuclear recoil from scattering with SM particles; indirect research, looking for bumps in the SM particle spectrum in cosmic rays with ground based or space observatories; artificial production from interactions of known particles produced at colliders [7].	15
1.6	Overview of the CERN accelerator complex in 2018 [8].	16

1.7	Schematic overview of the BSM landscape, based on a selection of specific models. The x-axis corresponds to the mass m_X of the lightest BSM state, and the y-axis to the scale of the effective new interaction where $M_{mediator}$ is the mass of a heavy mediator and g its dimensionless coupling constant to the Standard Model. The gray shaded area outlines the currently excluded regions, the red areas are schematic outlines of the areas targeted by the experiments considered in the PBC sensitivity studies. The true sensitivities of individual experiments can vary significantly as function of the model [3].	17
1.8	Existing data on νN CC scattering cross sections, where N refers to an isoscalar nucleon in target [25].	22
1.9	Feynman diagram for a charged current deep inelastic neutrino scattering. In the parton model, the constituent of the nucleon involved in the interaction has a fraction x of the nucleon's momentum.	23
1.10	ν_τ and $\bar{\nu}_\tau$ CCDIS cross sections predicted by the SM (solid) and in the $F_4 = F_5 = 0$ hypothesis (dashed) [28].	24
1.11	Neutrino and anti-neutrino induced charm production diagrams.	26
2.1	Global overview of the SHiP experiment.	29
2.2	Schematic layout of the SPS and its associated facilities. The planned additional beam line for the BDF is reported [40]. . .	30
2.3	Display from a slow beam extraction test for the Beam Dump Facility. The yellow line represents the proton beam intensity in the SPS and the white line represents the beam energy [40].	30
2.4	Layout of the BDF target assembly, showing the TZM and the tungsten blocks, together with the beam direction.	32
2.5	Maximum deposited energy density per proton in the target, as obtained from a Monte Carlo simulation [41].	33
2.6	Schematic representation of the active muon shield's principle. The paths of a 350 GeV/c muon and a 50 GeV/c muon are also shown [45].	34
2.7	Prompt dose rate from muons at the level of the beam axis, illustrating the function of the muon shield. The layout of the magnets is outlined in black [39].	35

2.8	Schematics of the Emulsion Target. On the left, the global structure, made of 19 walls. On the right, the composition of a single wall, with the bricks and CES components underlined.	35
2.9	Illustration of the principle of particle detection with nuclear emulsions: (a) is a picture of the nuclear emulsion, while (b) shows its internal structure. The silver bromide crystals themselves are seen in an electron microscope image in (c). The diameter of crystals is approximately 200 nm; (d) and (e) illustrate the principle of detection of a charged particle in the nuclear emulsion. Black small dots on silver bromide crystals show latent images in (d). From Ref.[46].	36
2.10	Schematic representation of the target unit: the brick on the left, the Compact Emulsion Spectrometer on the right.	38
2.11	Measured sagitta along the x axis for 1 GeV (left) and 10 GeV (right) pions. Magnetic field is along the y axis [39].	38
2.12	Illustration of the instrumentation of Target Trackers and Downstream Trackers.	39
2.13	Layout of the SND spectrometer magnet, showing the opening mechanism for the replacement of the emulsion films.	41
2.14	Layout of the SND muon identification system. The RPC and iron layers are visible.	42
2.15	Schematic diagram of the Hidden Sector detector (not to scale). An HNL decay is shown, as an example of HS decay topology [48].	43
2.16	Layout of the Hidden Sector Spectrometer magnet.	44
2.17	Hit resolution for a straw diameter equal to 20 mm. The measurement was performed by requiring no wire offset (on the left) and with a wire offset of 2 mm (on the right) [39].	45
2.18	Layout of the Timing Detector, in the plastic scintillator option.	46
2.19	Layout of the Hidden Sector calorimeter. The different colors mark separate regions.	47
2.20	SHiP exclusion limits at 90% C.L. as a function of the LDM mass M_X , compared to the current experimental limits [38].	48
2.21	SHiP sensitivity curves (90 % C.L.) for HNLs mixing to a single SM flavour: electron (blue), muon (red) and tau (green) [50].	50

3.1	On the left, momentum of charmed hadrons, separating the direct production from 400 GeV protons and the cascade production. The latter fraction is reported in the top-right inset. On the right, momentum of mother particles [54].	54
3.2	Momentum of produced tau neutrinos and antineutrinos, separating primary contribution (in blue) and cascade contribution (in red). The histograms are weighted to a spill of 5×10^{13} protons on target.	54
3.3	Spectrum of ν_τ transverse momentum vs momentum.	55
3.4	Momenta spectra of all neutrino flavours, underdoing a DIS interaction in the emulsion target [38].	56
3.5	Comparison between tau neutrinos from primary production (in blue) and cascade production (in red). On the left, the position of tau neutrinos in the transverse radius, with respect to the beam direction. On the right, the momentum of CCDIS interacting neutrinos.	56
3.6	Distribution of simulated neutrino interaction vertices, in the SND area. The emulsion target, dedicated to the reconstruction of neutrino interactions, is marked in red. The range of the y axis matches the height of the SND magnet.	58
3.7	Distributions that have driven the SND design. On the right: the signal from neutrinos, on the left, the muon background [39].	59
3.8	Layout of the Scattering Neutrino Detector. On the left, the lateral view. On the right, the front view.	59
3.9	Schematics of CCDIS neutrino interactions in the Emulsion Cloud Chamber: muon neutrino (left), tau neutrino (middle) and electron neutrino (right).	60
3.10	Display of a simulated muon neutrino event in the SND [57].	61
3.11	Display of a simulated tau neutrino interaction in an Emulsion Cloud Chamber of the SND. The tau lepton is drawn in blue.	62
3.12	Features of tau lepton decay: on the left, the kink angle. On the right, the flight length.	63
3.13	Implementation of the magnetic field maps in the simulation. On the left, the lateral view (zy plane), on the right, the front view (xy plane).	65

3.14	Sagitta distributions for tau decay daughters, from CES detectors. On the left, sagitta in the zx plane, without magnetic bending. On the right, sagitta in the zy plane, with magnetic bending, separating positive (in red) and negative (in blue) particles.	66
3.15	Electrons produced by tau decay, from a tau neutrino interaction. On the left, their energy spectrum. On the right, the plate number where they have been produced.	67
3.16	Momentum and angle of muons from tau decay. The red component is the one which enters the first RPC plane.	67
3.17	Diagram explaining the difference between tau neutrino interaction (a) and charm background events (b).	69
3.18	Distribution of phi angle between the tau lepton (in blue) or charmed hadron (in red) with respect to the hadrons produced in the neutrino interaction. The red line shows the minimum angle $\phi_{min} = 2.2$ rad required.	70
4.1	Photon total cross section in carbon and lead as function of the energy. The contributions of different processes are shown [53].	73
4.2	Picture of the detector installed in the moving table, in preparation for the test beam.	76
4.3	Drawing of run configurations during DESY test beam.	77
4.4	Geometry and picture of the SciFi trackers configuration [63].	78
4.5	An optical microscope used for the scanning of nuclear emulsion films.	78
4.6	Reconstruction of scanned emulsion information. On the left, reconstruction of micro-tracks from digitized clusters. On the right, reconstruction of base-tracks from two matched micro-tracks.	79
4.7	Position distribution of all showers in a run, in the frontal view (xy plane).	81
4.8	Display of a simulated shower in the Emulsion Cloud Chamber.	81

4.9	Distribution of the slope of the shower tracks, with respect to emulsion film number. On the left the signal distribution, on the right the background distribution. Film number 1 is the most upstream in the ECC target.	83
4.10	2D representation of electromagnetic shower hit search. The base tracks in the yellow region area are collected, and they are accepted if the position and angular displacements are satisfied.	83
4.11	Shower reconstruction efficiency as a function of the cone aperture angle and cylinder radius.	84
4.12	Angular spectrum of tracks starting from first three emulsion films. Tracks selected as possible shower injectors are shown in blue, below the red line at $\tan\theta < 0.05$	85
4.13	Number of segments associated to each reconstructed shower. The red line shows the applied selection $N_{segments} \geq 50$	85
4.14	Comparison between reconstructed showers from Monte Carlo simulations (in red) and from real data (in blue). On the left, the impact parameter over the longitudinal distance $IP/\Delta Z$. On the right, the angle with respect to the shower vertex θ'_{bt}	86
4.15	Display of a reconstructed shower in the zy plane from DESY RUN7 data.	86
4.16	Display of the reconstruction of an electromagnetic shower in the ECC, showing the x coordinate of each base-track with respect to z . The dotted rectangles represent the research region for associated base-tracks in each film. Signal segments are marked in red, while background ones in blue [69].	88
4.17	Drawing explaining two additional variables provided as input for discrimination between signal and noise segments in the Machine Learning classifier: the θ'_{bt} angle (above) and $IP/\Delta Z$ (below).	89
4.18	Schematic representation of a decision tree [72].	90
4.19	Size of reconstructed showers from RUN3 data. The dashed line shows the applied selection $N_{segments} \geq 50$	90
4.20	Showers provided by the Random Forest classifier from Monte Carlo simulations (in red) and from real data (in blue). On the left, the distance $IP/\Delta Z$. On the right, the angle θ'_{bt}	91

4.21	Comparison of performances between standard shower reconstruction (in green) and machine learning reconstruction (in purple) algorithms. On the left, recall distribution of electromagnetic shower reconstruction. On the right, precision distribution.	92
4.22	Calibration of shower energy measurement from the number of associated base-tracks [69].	93
4.23	On the left: energy resolution of the ECC calorimeter from a simulation of 6 GeV electron showers. On the right: resolution dependence on the shower energy [69].	94
5.1	Picture and schematics of the compact emulsion chamber used at airplan altitude [77].	96
5.2	First charm pair production observed in 1971, from detection of cosmic ray interactions in nuclear emulsions. Two kinks have been observed, at distance 1.38 cm and 4.88 cm from the main vertex, along with showers from π^0 decays [78].	97
5.3	Representation of the parton model description of an interaction involving two hadrons H_1 and H_2 . Taken from the lecture notes in Ref.[80].	98
5.4	Charm production cross section in nucleon-nucleon collision as a function of \sqrt{s} , compared to measurements from different experiments. Solid and dashed lines represent the theoretical predictions at NLO order and its uncertainties, respectively [81].	100
5.5	Lateral view of the experimental apparatus used in the 2018 optimization run.	101
5.6	Layout of the six different SHiP-charm target configurations.	101
5.7	Z position of produced charm vertices, comparing primary and cascade production. The lines represent the regions covered by the 2018 runs.	102
5.8	On the left, technical drawing of the target mover. On the right, a picture of the installed stage during a test exposure on a ECC target.	103
5.9	Pattern of the target movement in the 5 spills (left) and 10 spills (right) configurations.	103

5.10	Picture of the box containing the pixel modules, as seen from the beam.	104
5.11	Picture of SciFi and Drift Tubes detector configurations. . . .	105
5.12	Schematics of the muon tagger, showing the thickness of the five iron slabs and the position of the RPCs.	107
5.13	Shape of the proton beam, from the pixel hits belonging to the CHARM2-RUN1 dataset.	108
5.14	Low angle emulsion base-tracks ($\tan\theta < 0.1$), in a configuration with ten proton spills (CHARM1-RUN2, left) and five proton spills (CHARM1-RUN6, right), taken from the most downstream emulsion film.	109
5.15	Layout of the SHiP-charm geometry implemented in FairShip.	110
5.16	3D map of the B_y field component, units are in Tesla (T). . . .	110
5.17	Momentum distributions of charged charmed hadrons decay daughters, and the components which arrive at the various subdetectors of the SHiP-charm magnetic spectrometer. On the lower side, the corresponding acceptances are reported. .	111
5.18	Event display of a simulated proton interaction in the emulsion target. Downstream of the target, hits from the pixel detectors can be seen.	112
6.1	Track reconstruction efficiency (in red) and purity (in blue), as a function of the length of the tracks, expressed as the number of traversed emulsion films.	115
6.2	Display of a primary proton vertex and an hadronic interaction vertex.	116
6.3	Distributions of input variables used for the training of the BDT [90]. Spatial units are μm	118
6.4	Output of the BDT classifier for training and test sample [90].	119
6.5	Position of reconstructed vertices along the beam axis. The primary proton and hadron re-interaction components are distinguished in the Monte Carlo sample, while a global fit is performed on the data sample [90].	121
6.6	Results of the alignment between emulsion and pixel tracks. On the left, the average χ^2 per track with respect to the number of alignment iterations. On the right, the χ^2 distribution before and after alignment [91].	122

6.7	Position residuals along x (on the left) and along y (on the right) coordinates, after matching between emulsion and pixel tracks [91].	122
6.8	Angular residuals in the zx plane (on the left) and in the zy plane (on the right) coordinates, after matching between emulsion and pixel tracks [91].	123
6.9	Energy spectra of simulated charmed hadrons, from a beam of 400 GeV protons.	123
6.10	Drawing showing the definitions of “short” (top) and “long” decay (bottom) in an Emulsion Cloud Chamber.	124
6.11	Variables for BDT classification of decay vertices. Shown for signal (in blue) and background (in red). Spatial units are μm	125
6.12	Output of BDT classification of decay vertices. Shown for signal (in blue) and background (in red). The green line shows the applied selection at $BDT_{min} = -0.2$	126
6.13	Display of double charm candidate from CHARM1-RUN6 data.	127
6.14	Measurement of multiple scattering from the angles of base-tracks in nuclear emulsion films [94].	129
6.15	Momentum resolution of MCS measurement in ECC, for $P < 5 \text{ GeV}/c$. Tracks are daughters of charmed hadrons from CHARM1 simulation.	130
6.16	Display of a matched event in SHiP-charm. Tracks reconstructed in the ECC are marked purple, tracks reconstructed in the pixel detector are gray and matched tracks are marked with the dashed red line [91].	131

List of Tables

3.1	Expected neutrino flux for different neutrino flavours after collecting 2×10^{20} protons on target [39].	55
3.2	Branching ratios for τ decay channels [53].	62
3.3	Topological requirements for a tau decay event detected in an emulsion target. Decay search efficiency is reported for each decay channel separately.	63
3.4	Breakdown of efficiencies for the background induced by charmed hadron production in ν_μ CC interactions. Decay search requirements are the same applied for tau lepton identification. The requirement of the primary muon to be not identified is applied for the event to be classified as background.	68
3.5	Expected CCDIS muon neutrino interactions with charm production for 2×10^{20} protons on target [39] and expected number of observed events, after all the selections.	68
4.1	Summary of exposures at DESY19. The two ECC targets in RUN8 have been exposed to the same electron beam.	77
4.2	Table of average performances of the two reconstruction algorithms in the overall sample.	92
5.1	Comparison of charm production cross sections in pp collisions from the NA27 experimental measurement [82] and the NLO theoretical predictions, with typical values of the charm mass (in GeV). From the SHiP-charm proposal [81]. . .	99
5.2	Summary of the 2018 data taking session for the SHiP-charm experiment.	108

6.1	Vertex reconstruction efficiency for different analyzed data runs.	119
6.2	Known properties of the most frequent charmed hadrons expected in SHiP-charm data. Values from Particle Data Group 2020 [53].	124
6.3	Number of signal events and efficiency at each selection, as estimated from Monte Carlo simulations.	127
A.1	Exposure details for CHARM1 target bricks.	134
A.2	Exposure details for CHARM2 target bricks.	135
A.3	Exposure details for CHARM3 target bricks.	135
A.4	Exposure details for CHARM4 target bricks.	136
A.5	Exposure details for CHARM5 target bricks.	136
A.6	Exposure details for CHARM6 target bricks.	136

Acknowledgements

This PhD work was not possible without the help of many people.

First of all, my supervisors, Giovanni De Lellis and Antonia Di Crescenzo. They have provided me continuous support and guidance, forgiving my mistakes and pressing me to face the problems, not to avoid them. They have been always available to answer my questions and to discuss my doubts, even with all the various students and research topics they have to follow. My external referees, Masahiro Komatsu and Markus Cristinziani have forwarded me useful comments and corrections to improve the draft of my thesis, leading to this final version.

The emulsion group in Naples has been my home in all these years, providing a friendly and well equipped working environment. I consider all the people there both friends and colleagues. Annarita has been my mentor in the SHiP software framework, and even today remains for me a precious reference and example. Another fundamental mentor has been Valeri, who has shared with me his experience on the emulsion reconstruction software, always welcoming me in his office. Dario and Martina have been my trusted companions for all my studies, and their work in SHiP is precious for the entire Collaboration. I wish the best for their PhD degrees in Zurich. Daniele and Maria have also provided unique contributions during their Master theses, developing advances fields of research in our group. Valerio has performed a fantastic analysis on the reconstructed SHiP-charm vertices, and it was always available to assist me during my troubles. Andrey's experience with the microscopes makes all the research in our group possible. He not only keeps the microscopes running at their best, but he also continuously researches advanced optics and software systems to improve the speed and the quality of the emulsion scanning. Thanks for always listening to me when I come knocking to your door. Giuliana is an incredible physicist, able not only to perform excellent research but also to communicate it to everyone, which is an amazing and

rare talent. She has motivated me not only to improve my work, but also to challenge myself in various fields and tasks. Concerning the wellness and safety of our laboratory, I have also to thank Adele, always available and proactive in the relationships with the administration groups, at the same time continuing her precious research work in the FOOT experiment. My congratulations to Maria Cristina, who has recently seen her passion and dedication in the same experiment rewarded. A huge contribution to the analysis of FOOT data has been also performed by Brenda, who has been the first Master student I have guided in the particle physics and emulsion analysis software. I do not know her plans for the future, but my best wishes anyway. My best wishes also for Artem, who has started his PhD shortly after me. I wish him to write a fantastic thesis about his work in the NEWS experiment. I show not only my thanks but also my apologies to Asada, who often had to wait for me to go home before starting the scanning of the microscope near my workstation.

All my research has been performed within the SHiP Collaboration, and it was my first time working in an extensive and international group. Thanks to all the researchers for having warmly welcomed me there. Citing all of you with the rightful detail would be impossible, but I really thank Thomas, Eric and Oliver for their continuous assistance in the bugs and issues within the SHiP software, along with their advice. All the SHiP-charm research group worked constantly to make this analysis possible. The experience of Niko, Chris and Filipis has been fundamental in our work. Thank you very much!

My work experience at CERN has been wonderful and unforgettable. The supportive and welcoming atmosphere shows a precious example of collaborative research. Among my time at CERN, I remember most fondly the time spent in the library and in the cafeteria, where I could really feel to be a part of the most advanced particle physics research center in the world. The experience at the SPS Test Beam facility was challenging, but instructive and memorable nonetheless. Thanks to all the CERN staff working there for their continuous assistance. Also, the electron test beam has been performed at the Test Beam Facility at DESY Hamburg (Germany), a member of the Helmholtz Association (HGF). A huge thanks to them too.

A huge thanks to all my friends in the university, who have provided me some free time outside of the work hours, reminding me of the importance of a pleasant conversation and an hug in our lives. Nazarena, Rosario and

Lisa have been trusted companions of my lunch breaks during these three years. Thanks a lot for being available to spend time with me. Thanks to all the friends outside university too, I hope we can meet again soon.

Last, but not least, the patience and support of all my family: my father Pasquale, my mother Antonietta, my sister Maria Grazia and my brother-in-law Daniele. Finally my new nephew, the newborn Giovanni, brought both joy and a reason to come home with a smile everyday.